eXPRESS Polymer Letters Vol.7, No.12 (2013) 959
Available online at www.expresspolymlett.com
DOI: 10.3144/expresspolymlett.2013.93

Editorial corner – a personal view
Hard challenge with soft materials: Understanding large deformation and fracture behavior

P. M. Frontini[*]

Instituto de Ciencia y Tecnología de Materiales (INTEMA), CONICET Universidad Nacional de Mar del Plata, Juan B. Justo 4302, B7608FDQ Mar del Plata, Argentina

Rubber has been recognized as an engineering material since the mid 1800s. It is well known that the mechanical behavior of rubber is complicated due to nonlinearity, hyperelasticity and its great sensitivity to the effects of temperature, environment and strain history. Nowadays there seems to be a renewing interest in many other materials that show a similar behavior, collectively known as soft materials. Soft matter is a field that encompasses an incredible spectrum of topics from living tissues to diverse engineered materials, from personal care products to energy-efficient electronic-paper displays. Biological tissues, foams, food, elastomeric polymers, membranes, biomaterials, gels, granular materials, and their composites have called the attention of basic and applied researchers belonging to a variety of disciplines (DOI: 10.1039/C3SM90100A). Soft materials display a mixture of fluid and solid properties, which deform themselves easily under mechanical loads. Hitherto, their mechanical testing has focused primarily on low level deformation rather than on ultimate properties. However, for novel engineering applications, mechanical integrity appears to be very important and mechanical failure should be considered as necessary as stiffness for design purposes. In this context, the improvement of the fundamental understanding of the mechanics of soft materials, and the development of new suitable methods appears as an stimulating scientific goal (DOI: 10.1039/C2SM90089K). In summary, it is clear that there are plenty of problems which are associated wiht the hyperelastic nature and its corresponding nonlinear character of soft matter deformation awaiting for solutions. Based on these drivers, the following experimental and theoretical research topics may be suggested for future research efforts: Characterization of fracture behavior. Comparison of different toughness measurement methods. Characterization of cohesive zone properties. Development of strong, tough, shock-absorbing structural hydrogels. Understanding cavitation and other instability phenomena in soft solids and structures. Characterization of microstructure and damage evolution in soft materials. Development of new soft material composites with superior strain stiffening capability. Understanding the effects of adhesion on contact mechanics when the size and stiffness of material decrease. Development of new methods to bridge the gap between mechanical testing of articular cartilage and hydrogels in cartilage regeneration. Derivation of nonlinear elastic stress–strain constitutive laws to describe the indentation of materials beyond the Hertzian regime.

Prof. Dr. Patricia Maria Frontini
Member of International Advisory Board

[*]Corresponding author, e-mail: pmfronti@fi.mdp.edu.ar

eXPRESS Polymer Letters Vol.7, No.12 (2013) 960–965
Available online at www.expresspolymlett.com
DOI: 10.3144/expresspolymlett.2013.94

Self-standing chitosan films as dielectrics in organic thin-film transistors

J. Morgado[1,2], A. T. Pereira[1], A. M. Bragança[1], Q. Ferreira[1], S. C. M. Fernandes[3], C. S. R. Freire[3], A. J. D. Silvestre[3], C. Pascoal Neto[3], L. Alcácer[1]*

[1]Instituto de Telecomunicações, Instituto Superior Técnico, Avenida Rovisco Pais, P-1049-001 Lisboa, Portugal
[2]Department of Bioengineering, Instituto Superior Técnico, UTL, Avenida Rovisco Pais, P-1049-001 Lisboa, Portugal
[3]CICECO, University of Aveiro, Campus de Santiago, P-3810-193 Aveiro, Portugal

Received 26 June 2013; accepted in revised form 9 August 2013

Abstract. Organic thin film transistors, using self-standing 50 μm thick chitosan films as dielectric, are fabricated using sublimed pentacene or two conjugated polymers deposited by spin coating as semiconductors. Field-effect mobilities are found to be similar to values obtained with other dielectrics and, in the case of pentacene, a value (0.13 $cm^2/(V \cdot s)$ comparable to high performing transistors was determined. In spite of the low On/Off ratios (a maximum value of 600 was obtained for the pentacene-based transistors), these are promising results for the area of sustainable organic electronics in general and for biocompatible electronics in particular.

Keywords: *biocompatible polymers, organic thin-film transistors, organic field-effect transistors, chitosan, dielectric*

1. Introduction

There is a significant effort being put into the development of organic electronics employing various renewable materials, encompassing paper, leather, silk and biodegradable plastics, for various functions [1]. There are very interesting possibilities in terms of the development of 'green', biocompatible and biodegradable electronics with low production costs. For instance, various researches are being focused on paper. This has been studied as a substrate for printed circuits, using low cost fabrication methods. The fact that these systems combine flexibility and lightweight opens up various areas of application such as consumer electronics, disposable systems and applications in medical sensing and micro-electromechanical systems [2]. Paper was also used as material for flexible electronics [3].

Chitosan (CS) is a cationic polysaccharide obtained by alkaline deacetylation of chitin, this being the second most abundant polymer in nature, after cellulose. Chitin appears in nature as ordered crystalline microfibrils forming structural components of the exoskeleton of crustacean and insects and in the cell walls of fungi and algae [4, 5]. In view of its properties, like excellent film-forming ability, biocompatibility and biodegradability [4] chitosan and derivatives have been used in biomedical applications, such as gene delivery, biosensors [6] and also as proton exchange membranes [7]. These applications offer the prospects for the fabrication of biocompatible devices that could operate in biologically relevant media (for instance for smart sensing and preventive medical care), an area that is attracting an increasing attention [8].

In 2011, two reports appeared on the use of chitosan-based materials in electronics. One paper, by Zhong *et al*. [9], explored the protonic conduction in maleic-chitosan thin films to fabricate a protonic

*Corresponding author, e-mail: jorge.morgado@lx.it.pt

field-effect transistor, yielding a proton mobility of $4.9 \cdot 10^{-3}$ cm^2/(V·s). In another study, chitosan was used as dielectric in an ITO-based thin film transistor [10]. In this study, a chitosan film was deposited on ITO-coated glass by drop cast from an acetic acid solution. No indication of its thickness was given. ITO source, drain and channel were fabricated by RF magnetron sputtering. The devices were tested at ambient conditions. The authors obtained high performance transistors, which they attribute to the influence of proton mobility leading to very high gate dielectric capacitance due to electric-double-layer effect at the interface between dielectric and the semiconducting oxide. No reports were found on the use of CS as dielectric material in organic transistors.

In view of the CS potential, we have been studying self-standing CS films both as substrates and dielectrics for organic thin film transistors (TFTs). Here, we report on the performance of TFTs fabricated with organic semiconductors deposited by sublimation (pentacene) and by spin coating (regioregular head-to-tail poly(3-hexylthiophene), P3HT, and poly(9,9-dioctylfluorene-*alt*-bithiophene), F8T2), on the bare surface of self-standing CS films.

We find high hole field-effect mobilities (peaking at 0.13 cm^2/(V·s) for pentacene) though the On/Off ratios are small. A strong hysteresis effect is found which is attributed to the presence of ionic mobile species in the CS films.

2. Experimental

Chitosan, with a degree of deacetylation of 97% and a viscosity-average molar mass of 350 000 g/mol, was purchased from Mahtani Chitosan Pvt. Ltd. (India) and purified before use [11]. For the preparation of the CS films, a solution 1.5% (w/v) at pH = 4 was first prepared by dissolving the purified powdered CS sample in aqueous acetic acid (1% v/v) at room temperature during 48 h. An appropriate mass of CS solution was then transferred onto 10×10 cm^2 square plates. ~50 μm thick films were obtained by casting at 30ºC in a ventilated oven for 16 h. The obtained films were kept in atmospheric conditions until they were used for the thin film transistors fabrication.

The surface of the CS films were characterized by atomic force microscopy, using a Molecular Imaging Agilent (model 5100) system, operating in non-contact mode (at a resonance frequency between 200 and 400 kHz) using silicon probes with tip radii lower than 10 nm.

Thin-film transistors were prepared by depositing, first, a gate contact of ca. 40 nm thick aluminum on one (down) side of the CS film, using an Edwards evaporator at a base pressure of ca. $2 \cdot 10^{-5}$ mbar. Pentacene-based TFTs were prepared by thermal deposition depositing, on the other side of the CS film, a ca. 150 nm thick pentacene film. Transistors with F8T2 were prepared in air by spin coating from a xylene solution. A thin F8T2 film (ca. 100 nm thick) was thus formed on the CS film surface, opposite to the Al gate contact. These two types of device structures (with pentacene and F8T2) were then transferred inside a glove box (<0.1 ppm O_2, <0.3 ppm H_2O) to deposit source and drain contacts. P3HT was deposited by spin coating inside the glove box. The film thickness is ca. 40 nm. These three types of thin film transistors were then finalized by depositing source and drain contacts through a shadow mask, defining a channel with a length of L = 100 μm and a width of W = 5.1 mm. Source and drain contacts consisted of a bilayer structure, comprising MoO_3 (ca. 20 nm thick, which is a very efficient hole-injection material) covered with a 50–60 nm thick layer of Al. These transistors were characterized inside the glove box (to avoid damaging the source and drain contacts upon contact with ambient humidity), 24–48 h after the source and drain deposition, using a Semiconductor Parameter Analyzer HP 4140B. We note that the three types of devices were prepared from the same large CS film. We therefore expect that the characteristics of the CS dielectric, namely the water content, are similar for all three TFT structures. The thicknesses of the organic semiconductors were determined in films deposited, under similar conditions, on a glass substrate, using a Dektak 6M profilometer.

The specific capacitance of the CS film was measured with an Impedance Analyzer HP4192A at 1 kHz. A capacitor structure was fabricated by ink jet printing silver of both sides of the CS film, using a Dimatix printer.

3. Results and discussion

Figure 1 shows the topography image obtained over an area of 10×10 μm^2. Some fibers with diameters

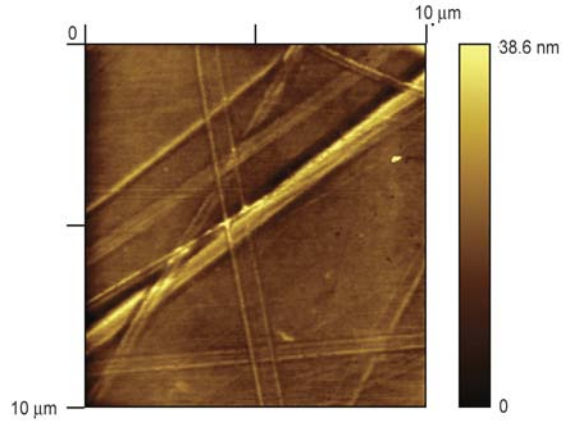

Figure 1. Topography image of a CS film over an area of 10·10 µm^2, evidencing some fibers dispersed over a very regular surface

on the order of 150 nm are observed. The regions between the fibers appear very regular, with a root-mean-square roughness (R_{rms}) not exceeding 1 nm.

The specific capacitance of the CS film measured for the capacitor structure fabricated by ink jet printing silver of both sides of the CS film at 1 kHz is $C_0 = 9.54 \cdot 10^{-9}$ F/cm^2. We note that, a lower capacitance value of $3.26 \cdot 10^{-11}$ F/cm^2 was measured, also at 1 kHz, when the CS film is placed in between two gold discs. We attribute this difference to the porous nature of the CS films surface, leading to an effective thickness that is much lower than the 'geometrical' value considered when using the gold discs. Although Figure 1 evidences a flat surface, a detailed study over smaller areas, confirms the existence of a porous structure, as shown in Figure 2. Though the line profile shows that such pores are few nanometers deep. However, this is likely limited by the tip radius, thus preventing us to determine the real value.

We further note that a comparable specific capacitance of ca. 10^{-7} F/cm^2 was determined at 1 kHz in a drop cast film of chitosan on ITO, though the film thickness was not reported [10]. It should be pointed out that, in view of its highly hygroscopic nature, the dielectric response of the chitosan is dependent on the water content [12] and likely on the deacetylation degree, leading to variable values in different reports.

Figure 3 shows the output characteristics and the transfer curve for the pentacene-based TFT. The curves are typical of a p-type TFT working in accumulation, as typically found in pentacene-based TFTs. The output curves were recorded at two different sweep rates. We find that a lower sweep rate

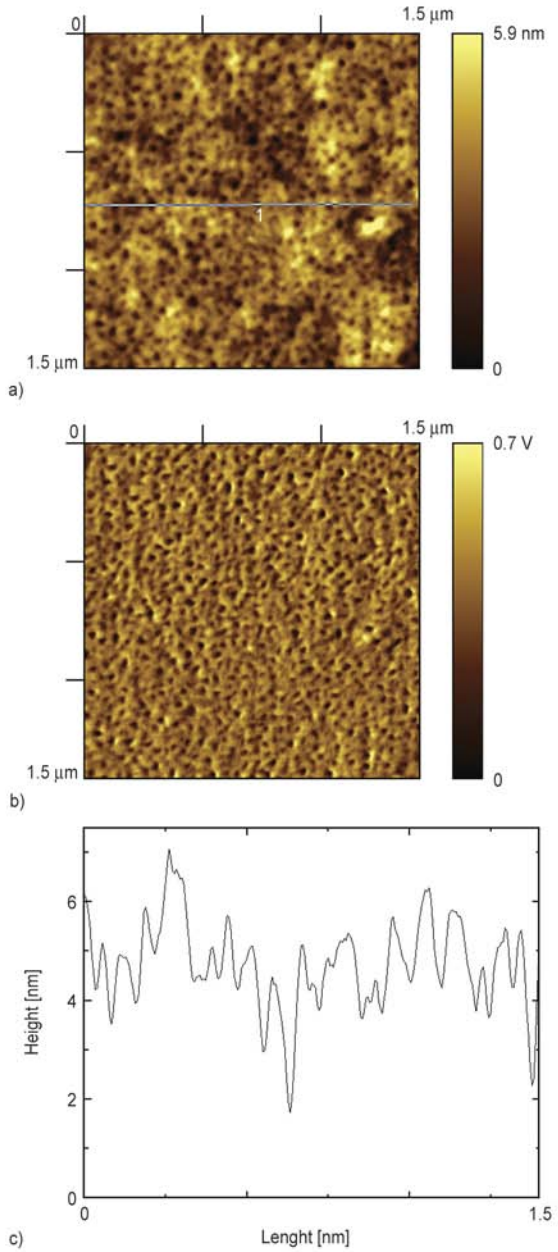

Figure 2. a) Topography and b) phase image of a CS film over an area of 1.5×1.5 µm^2, evidencing the porous structure. c) Line profile corresponding to the line marked in a).

leads to slightly higher currents. The transfer curve exhibits a marked hysteresis, which is attributed to mobile ions within the chitosan dielectric [10]. This hysteresis, with an increase of the current in the reverse sweep, is consistent with the output current increase upon decrease of the sweep rate (Figure 3a) and attributed to ion displacements within CS film. The transfer curve shows a low On/Off current ratio (between $V_g = -20$ and $V_g = 0$ V) of about 70 (in the forward sweep), which is reduced to ca. 4 in the back sweep. From the linear region of the $(I_d)^{1/2}$ *vs*

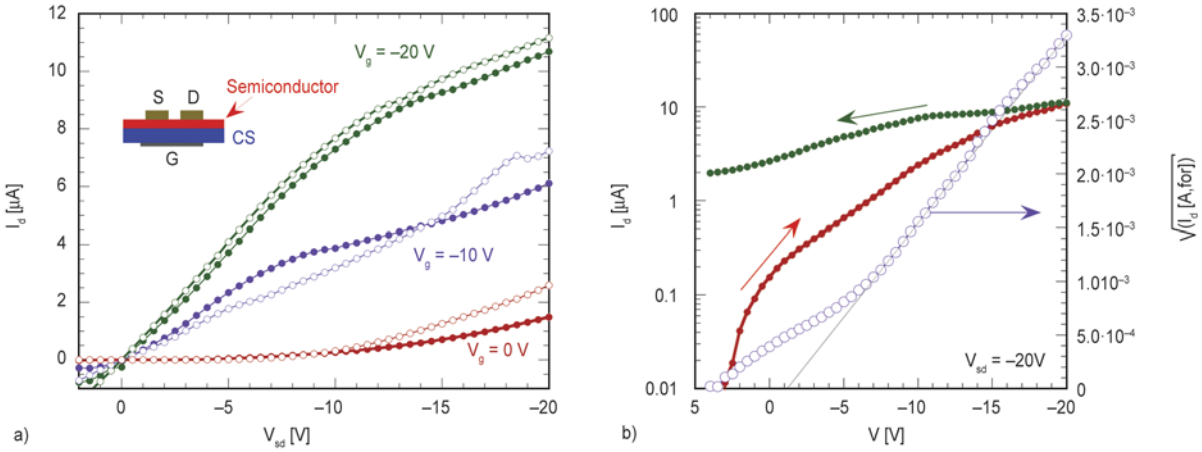

Figure 3. Output and transfer curves for a pentacene TFT. a) Two measuring rates were used, 0.5 V/s (closed symbols) and 0.5 V/5 s (open symbols). The inset shows the TFT scheme. The transfer curve (b) was measured at rate of 0.5 V/s. In b) we also show the plot of $(I_d)^{1/2}$ as a function of the gate voltage (V_g) for the forward (+4 to –20 V) sweep.

V_g plot, we estimate a saturation mobility of 0.13 cm^2/(V·s), using the well-known relation given by Equation (1):

$$I_d = \mu \frac{WC_0}{2L}(V_g - V_{th})^2 \quad (1)$$

Figure 4 shows the transfer curves for TFTs based on F8T2 and P3HT prepared by spin coating. Both TFTs show the typical p-type behavior. F8T2-based TFTs exhibit the highest On/Off ratio of ca. 600 (in the forward sweep), reduced to 60 in the back sweep, while the values found for the P3HT-based TFTs are ca. 6 and 3 respectively. The saturation field-effect mobility determined for the P3HT-based TFT is $8.6 \cdot 10^{-3}$ cm^2/(V·s). In the case of the F8T2-based TFT, if we just fit the data for V_g between –15 and –20 V, where the slope of the $(I_d)^{1/2}$ *vs* V_g curve has decreased, we obtain a field-effect mobility of $9 \cdot 10^{-4}$ cm^2/(V·s).

These results show that CS dielectric allows the formation of a conducting channel with these three organic semiconductors. The On/Off ratios are very small, but the mobilities are close to the highest values reported for other dielectrics. For instance, a mobility of 0.4 cm^2/(V·s) was reported for pentacene TFTs with a silane-modified SiO_2 dielectric and MoO_3/Al source and drain contacts [13]. We note that, for similarly prepared TFTs with 625 nm thick SiO_2 dielectric, we obtained a mobility of ca. $8 \cdot 10^{-4}$ cm^2/(V·s) for P3HT, which is lower than the value obtained with CS dielectric. However, this is also much lower than the values reported for primed P3HT transistors (e.g. 0.12 cm^2/(V·s) [14]). Finally, mobilities on the order of 10^{-2} cm^2/(V·s) were reported for optimized TFTs structures based on aligned F8T2 [15]. It should be emphasized that no surface treatment of the CS film and no thermal annealing was carried out on the organic semicon-

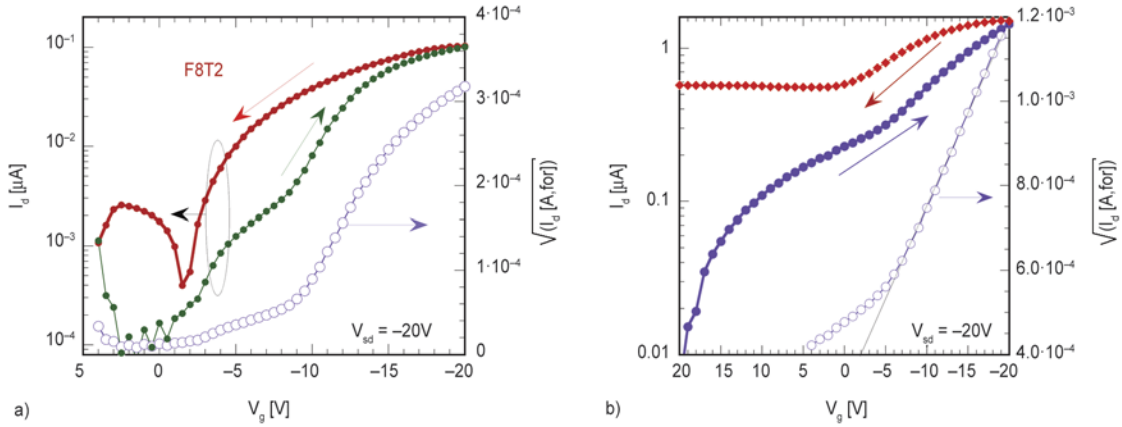

Figure 4. Transfer curves of TFTs based on F8T2 (a) and P3HT (b). The arrows indicate the voltage sweep. Also shown is $(I_d)^{1/2}$ *vs* V_g (open symbols).

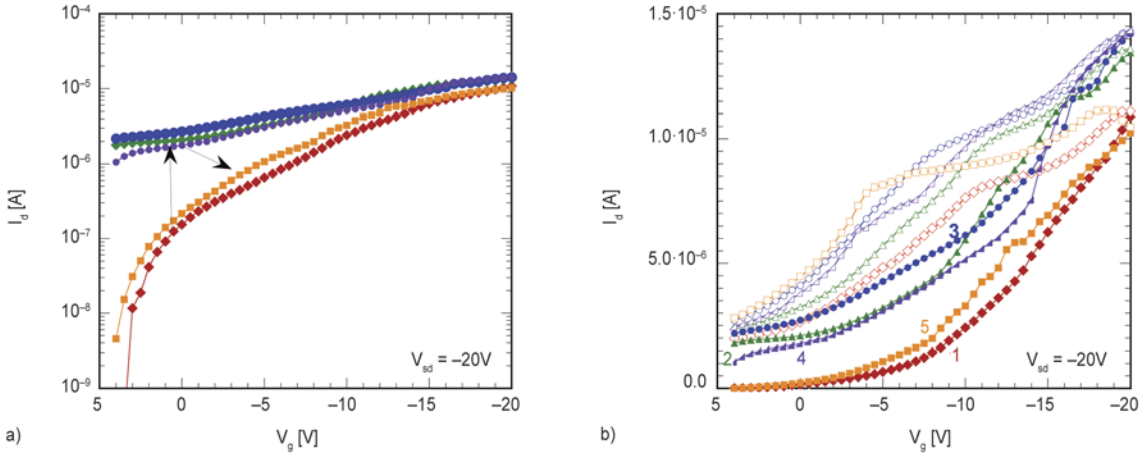

Figure 5. Forward transfer curves for the pentacene-based TFT of sequential sweep cycles. Measurements were carried out at a sweep rate of 0.5 V/s, starting at curve 1 up to 4. Curve 5 was obtained after ca. 2 h resting time, evidencing an almost complete recovery of the initial behavior. A different color and symbol type is associated to each cycle.

ducting films. We therefore anticipate that there is still room for improvement of the performance here reported. The other significant characteristic of the CS TFTs is the presence of significant hysteresis. Figure 5 shows the effect of the hysteresis on the transfer curve of pentacene-based transistors on five sequential voltage cycles. Figure 3 showed that, the Off current in the back sweep is much higher than that measured in the forward sweep. Figure 5a shows the transfer curves obtained in the forward sweep of each cycle, along 4 sequential cycles. The measured curve remains relatively constant between the 2nd and 4th cycles. If the TFT is left to recover for two hours we obtain a transfer curve very similar to the first one. The complete voltage cycles are shown in Figure 5b, where the forward sweep corresponds to the filled symbols and the back sweep to the open symbols. We attribute these results to ionic displacements within the CS dielectric in response to the applied gate bias.

It was mentioned above that CS is a hygroscopic material and that its proton conductivity has indeed been explored in previous studies. The effect of the water content was not addressed here but, based on the studies carried out by Kaihovirta *et al.* [16], for instance, in TFTs with hygroscopic dielectrics, the water content may in fact play an important role on the performance of transistors. Additional studies are in progress to better evaluate the role of the water content and the possible electric-double-layer effects on the behavior of the organic transistors.

4. Conclusions

In summary, we showed that self-standing chitosan films are very interesting dielectrics for organic TFTs. Transistors prepared with either thermal evaporated or spin coated films of organic semiconductors showed high hole field-effect mobilities though the On/Off ratios are small. We believe these studies open the way for the application of CS films in organic electronics for a wide range of applications, ranging from disposable systems to biosensors and biomedical applications [17].

Acknowledgements

This work was supported by FCT-Portugal under the contracts PTDC/CTM/099452/2008, PTDC/CTM/102144/2008 and PEst-OE/EEI/LA0008/2013. QF thanks FCT for a post-doc grant.

References

[1] Irimia-Vladu M., Saricifcti N. S., Bauer S.: Exotic materials for bio-organic electronics. Journal of Materials Chemistry, **21**, 1350–1361 (2011). DOI: 10.1039/C0JM02444A

[2] Siegel A. C., Phillips S. T., Dickey M. D., Lu N., Suo Z., Whitesides G. M.: Foldable printed circuit boards on paper substrates. Advanced Functional Materials, **20**, 28–35 (2010). DOI: 10.1002/adfm.200901363

[3] Tobjörk D., Österbacka R.: Paper electronics. Advanced Materials, **23**, 1935–1961 (2011). DOI: 10.1002/adma.201004692

[4] Rinaudo M.: Chitin and chitosan: Properties and applications. Progress in Polymer Science, **31**, 603–632 (2006). DOI: 10.1016/j.progpolymsci.2006.06.001

[5] Pillai C. K. S., Paul W., Sharma C. P.: Chitin and chitosan polymers: Chemistry, solubility and fiber formation. Progress in Polymer Science, **34**, 641–678 (2009). DOI: 10.1016/j.progpolymsci.2009.04.001

[6] Singh R., Verma R., Kaushik A., Sumana G., Sood S., Gupta R. K., Malhotra B. D.: Chitosan–iron oxide nano-composite platform for mismatch-discriminating DNA hybridization for *Neisseria gonorrhoeae* detection causing sexually transmitted disease. Biosensors and Bioelectronics, **26**, 2967–2974 (2011). DOI: 10.1016/j.bios.2010.11.047

[7] Smitha B., Sridhar S., Khan A. A.: Polyelectrolyte complexes of chitosan and poly(acrylic acid) as proton exchange membranes for fuel cells. Macromolecules, **37**, 2233–2239 (2004). DOI: 10.1021/ma0355913

[8] Irimia-Vladu M., Troshin P. A., Reisinger M., Shmygleva L., Kanbur Y., Schwabegger G., Bodea M., Schwödiauer R., Mumyatov A., Fergus J. W., Razumov V. F., Sitter H., Sariciftci N. S., Bauer S.: Biocompatible and biodegradable materials for organic field-effect transistors. Advanced Functional Materials, **20**, 4069–4076 (2010). DOI: 10.1002/adfm.201001031

[9] Zhong C., Deng Y., Roudsari A. F., Kapetanovic A., Anantram M. P., Rolandi M.: A polysaccharide bioprotonic field-effect transistor. Nature Communications, **2**, 476/1–476/5 (2011). DOI: 10.1038/ncomms1489

[10] Zhou B., Sun J., Han X., Jiang J., Wan Q.: Low-voltage organic/inorganic hybrid transparent thin-film transistors gated by chitosan-based proton conductors. IEEE Electron Device Letters, **32**, 1549–1551 (2011). DOI: 10.1109/LED.2011.2164612

[11] Cunha A. G., Fernandes S. C. M., Freire C. S. R., Silvestre A. J. D., Pascoal Neto C., Gandini A.: What is the real value of chitosan's surface energy? Biomacromolecules, **9**, 610–614 (2008). DOI: 10.1021/bm701199g

[12] Nogales A., Ezquerra T. A., Rueda D. R., Martinez F., Retuert J.: Influence of water on the dielectric behaviour of chitosan films. Colloid and Polymer Science, **275**, 419–425 (1997). DOI: 10.1007/s003960050099

[13] Chu C-W., Li S-H., Chen C-W., Shrotriya V., Yang Y.: High-performance organic thin-film transistors with metal oxide/metal bilayer electrode. Applied Physics Letters, **87**, 193508/1–193508/3 (2005). DOI: 10.1063/1.2126140

[14] Chang J-F., Sun B., Breiby D. W., Nielsen M. N., Sölling T. I., Giles M., McCulloch I., Sirringhaus H.: Enhanced mobility of poly(3-hexylthiophene) transistors by spin-coating from high-boiling-point solvents. Chemistry of Materials, **16**, 4772–4776 (2004). DOI: 10.1021/cm049617w

[15] Sirringhaus H., Wilson R. J., Friend R. H., Inbasekaran M., Wu W., Woo E. P., Grell M., Bradley D. D. C.: Mobility enhancement in conjugated polymer field-effect transistors through chain alignment in a liquid-crystalline phase. Applied Physics Letters, **77**, 406–408 (2000). DOI: 10.1063/1.126991

[16] Kaihovirta N., Aarnio H., Wikman C-J., Wilén C-E., Österbacka R.: The effects of moisture in low-voltage organic field-effect transistors gated with a hydrous solid electrolyte. Advanced Functional Materials, **20**, 2605–2610 (2010). DOI: 10.1002/adfm.201000586

[17] Kim D-H., Viventi J., Amsden J. J., Xiao J. Vigeland L., Kim Y-S., Blanco J. A., Panilaitis B., Frechette E. S., Contreras D., Kaplan D. L., Omenetto F. G., Huang Y., Hwang K-C., Zakin M. R., Rogers J. A.: Dissolvable films of silk fibroin for ultrathin conformal bio-integrated electronics. Nature Materials, **9**, 511–517 (2010). DOI: 10.1038/nmat2745

eXPRESS Polymer Letters Vol.7, No.12 (2013) 966–973
Available online at www.expresspolymlett.com
DOI: 10.3144/expresspolymlett.2013.95

On a novel method to synthesize POSS-based hybrids: An example of the preparation of TPU based system

O. Monticelli[1*], *A. Fina*[2], *D. Cavallo*[3], *E. Gioffredi*[2], *G. Delprato*[1]

[1]Dipartimento di Chimica e Chimica Industriale, Università di Genova, Via Dodecaneso, 31, 16146 Genova, Italy
[2]Dipartimento di Scienza Applicata e Tecnologia, Politecnico di Torino-sede di Alessandria, viale Teresa Michel, 5, 15121 Alessandria, Italy
[3]Department of Mechanical Engineering, Eindhoven University of Technology, P.O. Box 513, 5600 MB Eindhoven, The Netherlands

Received 4 July 2013; accepted in revised form 9 August 2013

Abstract. A novel method to prepare polymer/polyhedral oligomeric silsesquioxanes (POSS) hybrids by melt reactive blending is proposed in this paper, by the controlled polymer chain scission and reaction of chain ends with functional silsesquioxanes. Application to thermoplastic polyurethanes (TPU) is addressed, taking advantage of the polyurethane chain scission equilibrium reaction, leading to the formation of highly reactive isocyanate and hydroxyl chain ends. Despite the isocyanate chemistry has been widely studied for the preparation of polymer/POSS hybrids by *in situ* copolymerisation, the exploitation of similar chemical processes in an industrially viable and environmental friendly melt blending process is currently an open research field. In this work, the reaction in the molten state of dihydroxyl-functionalised POSS with the polyurethane chain is demonstrated to produce a TPU/POSS hybrids. The effect of POSS concentration on nanomorphology, thermal properties and surface properties is studied, showing significant changes compared to pristine TPU. In particular, an increase of glass transition temperature is observed in the presence of reactive POSS (ΔT up to about 10°C in the presence of 10 wt% loading). Furthermore, an increase of surface water wettability, evidenced by the decrease of water contact angle from 95° for pristine TPU to 70° in TPU containing 10 wt% of reactive POSS, is found.

Keywords: *nanocomposites, POSS, TPU, T_g, reaction blending*

1. Introduction

Polyhedral oligomeric silsesquioxanes (POSS) have been used as an interesting class of precursors for the synthesis of molecularly designed organic/inorganic hybrids [1]. POSS bridges the gap between fillers and monomers in modifying macromolecules mobility and thus the reinforcement of polymer materials. Indeed, POSS are organic/inorganic molecules, with a size of approximately 1 to 3 nm, with a general formula of $(RSiO_{1,5})n$ where R is hydrogen or an organic group, such as alkyl, aryl or any of their derivatives [2, 3]. The size of the pendant POSS cage is comparable to the dimensions of the linear polymer, enabling POSS to control the motions of the chains at the molecular level with enhanced benefits while retaining the processability and mechanical properties of the pristine polymer [1].

From a general point of view, the incorporation of the thermally robust POSS moiety into organic polymers was found to modify drastically the thermal properties of the polymer supplying improved thermal stability to the polymer matrix [4, 5], also allowing the tailoring of the polymer glass transition temperature by tuning the POSS concentration [6]. Moreover, incorporation of POSS molecules is responsible for modifications of the mechanical

*Corresponding author, e-mail: orietta.monticelli@unige.it

properties [7, 8] as well as reduction in both flammability and rate of heat release during combustion [9].
The preparation of POSS/polymer systems has been accomplished following different approaches. In particular, *in situ* copolymerization of POSS to produce hybrid organic-inorganic polymers with pendent POSS groups has been widely studied both for thermoplastics and thermosets [10–12]. On the other hand, melt blending was also widely studied, this process being very appealing, economic and environmentally friendly [13, 14]. Nevertheless, the dispersion of POSS into polymers by simple melt mixing is not obvious and requires the strict control of the balance between polymer–POSS interactions and POSS–POSS self-interactions.
Solution blending [15, 16] and vapour phase grafting [17] have also been attempted to incorporate POSS into a polymer matrix. Recently, some work has been also carried out on the preparation of polymer/POSS systems by melt reactive blending techniques [18]. Chemical reactions between POSS and polymer chains in the molten state can indeed be taken into advantage to promote molecular dispersion of POSS [19]. Nevertheless, the above approach can only be applied to polymer matrices carrying reactive side groups capable of reacting with silsesquioxane molecules. On this ground, the generalization of the reactive melting approach to polymers which does not carry reactive side groups is indeed of great interest.
The innovative approach, proposed in the present work, is based on the reaction between silsesquioxane molecules and the macromolecule functional groups, which are formed directly during the melt blending process through a controlled scission of the polymer matrix.
In order to employ chain scission to generate reactive functions to be exploited for further reactions during melt blending, very controlled statistical chain scission should be obtained. This is possible in principle with different polymers, including polyamides, polyesters and thermoplastic polyurethanes. The latter class of polymers has been chosen due to the properties of polyurethanes and the intrinsic reactivity of isocyanate groups.
POSS hybrids based on polyurethane (PU) have been previously prepared by *in situ* polymerization. Indeed, synthesis of amphiphilic telechelic oligourethanes with terminal POSS groups through reaction of monoisocyanate substituted POSS and oligo (oxyethylene diol) and investigation of the structure of such polymers in solution were reported [20, 21]. Interestingly, chemical reaction of monoisocyanate substituted POSS fragments with polyamidoamine of a dendritic nature (polyamidoamine PAMAM dendrimers) leads to the formation of several organo-inorganic core–shell type nano-hybrids [22]. Application of dihydroxy-containing POSS with isocyanate pre-polymers can yield linear segmented PU with POSS fragments as a side group of the hard segments [23–28]. By analogy with this method, diamino-POSS was used to prepare nanostructured PU–POSS hybrid aqueous dispersions [29]. As demonstrated, the reaction of the silanol groups of an open cage POSS with isocyanate moieties gave segmented PU with POSS incorporated in the polymer main chain as a part of the hard segment [30]. Cross-linked PU were also synthesized through the reaction of octafunctional POSS with either isocyanate [31] or amine groups. [32]
Few papers reported on the preparation of composites based on PU by melt blending. Bourbigot *et al*. [33] described the reaction to fire of composites based on TPU containing 10 wt% of POSS prepared in a Brabender-type mixer.
In this work, a novel method to prepare PU/POSS hybrids directly by melt blending is explored: controlled chain scission of a commercial thermoplastic PU (TPU) is carried out to obtain the formation of functional groups potentially capable of reacting with diol-functionalised polyhedral oligomeric silsesquioxane molecules.

2. Experimental

2.1. Materials

Octaisobutyl POSS (referred to as oib-POSS in the following) and trans-cyclohexanediolisobutyl POSS (referred to as POSS-OH in the following) were purchased from Hybrid Plastics (Hattiesburg, MS, USA) as crystalline powders and used as received. Chemical structures for oib-POSS (M = 873.6 g/mol) and POSS-OH (M = 959.7 g/mol) are reported in Figure 1.
The polyurethane used (Elastollan 1185A), kindly supplied by BASF (Germany), was a polyether-based thermoplastic PU.

2.2. TPU/POSS system preparation

Before accomplishing the hybrid preparation, the polymer matrix was dried overnight at 110°C. TPU

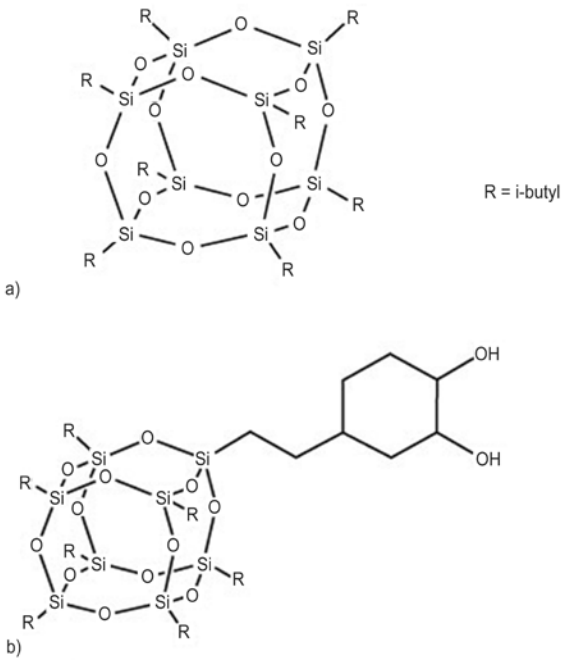

Figure 1. (a) Octaisobutyl POSS (oib-POSS), (b) trans-cyclohexanediolisobutyl POSS (POSS-OH)

was added to the glass reactor, namely a laboratory internal mixer provided with a mechanical stirrer (Heidolth, type RZR1), which was connected to a vacuum line and evacuated for 30 min at 100°C. Then, the reactor was purged with helium for 30 min. The above operations were repeated at least three times, to be sure to avoid humidity to come in contact with the reagents.

The reactor was placed in an oil bath at 220°C and when the polymer was completely molten, POSS was added under inert atmosphere. TPU/POSS systems were prepared by mixing, under inert atmosphere, the neat polymer and POSS, both octaisobutyl and trans-cyclohexanediolisobutyl POSS, at various concentrations, from 2 to 20 wt%, using a mixing time of 10 min.

Neat TPU was processed and characterised under the same conditions, as reference material. Materials are identified in the text with the format polymer/POSS type(concentration); as: TPU/POSS-OH(10).

In order to evaluate the reaction yield after melt blending, all solid samples were broken into small pieces and unreacted POSS was removed by Soxhlet extraction with hexane for 48 h. The grafting yield was calculated by weighting composite samples before and after the above treatment.

2.3. Characterization

Fourier Transform-Infrared Spectroscopy (FT-IR) spectra were recorded by a Bruker IFS66 spectrometer. The samples were scanned in the range 400–4000 cm^{-1} with nitrogen purge.

Differential scanning calorimetry (DSC) was performed under a continuous nitrogen purge on a Mettler (Mettler, Columbus, OH, USA) calorimetric apparatus, model TC10A. Both calibrations of heat flow and temperature were based on a run in which one standard sample (indium) was heated through its melting point. Samples having a mass between 2.5 and 6 mg were used. Data were gathered using a scan rate of 10°C/min.

Transmission electron microscopy analyses were performed with a high-resolution equipment JEOL 2010 (Tokyo, Japan). The measurements were carried out using an accelerating voltage of 200 kV. Ultrathin sections of about 100 nm thick were cut with a Power TOMEX microtome equipped with a diamond knife and placed on a 200-mesh copper grid and stained with ruthenium tetraoxide to obtain sufficient phase contrast.

Contact angle measurements were performed at room temperature with an Erma G-1 contact angle meter using pure water as probe liquid.

3. Results and discussion

3.1. Study of the polymer matrix thermal behavior

This work has been preliminarily focused on the study of TPU thermal behavior, the approach for the hybrid polymer/POSS synthesis being based on a controlled polymer matrix decomposition which allows to create reactive groups, potentially capable of reacting with silsesquioxane molecules. The mechanisms of thermal decomposition of polyurethanes were reviewed by Chattopadhyay and Webster [34]. Despite a number of possible concurrent reactions is possible, urethane bond scission (Figure 2), is typically obtained as a first step, at relatively low temperatures (180–250°C), depending on the PU structure [34].

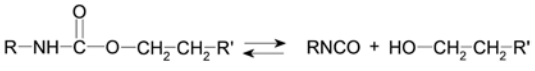

Figure 2. Thermal degradation mechanism of the urethane segment by depolymerisation

During thermal decomposition of PU, this first decomposition step is followed by further scission of the hard and soft segments, leading to a number of secondary decomposition products. However, secondary decomposition steps are much slower and thus require significantly higher temperature to occur. Therefore, it is possible in principle to induce a limited extent of chain scission without reaching the conditions of extensive decomposition and volatilisation of the polymer, thus allowing to produce isocyanate groups during melt mixing.

Thermogravimetric measurements, carried out in heating ramp showed no detectable weight loss until 260°C, supporting no significant volatilisation of polymer during melt blending.

IR spectra of our TPU and that of the polymer treated at 200°C are given in Figure 3.

The FT-IR spectrum of the neat TPU presents a characteristic band at 3328 cm^{-1}, which corresponds to the stretching vibration of N–H group [35]. The bands at 2956 and 2870 cm^{-1} can be attributed to asymmetric and symmetric stretching of CH_2 group [36]. The shoulder at 1730 cm^{-1} characterizes C=O stretching vibrations in ester structure, while the peak at 1705 cm^{-1} corresponds to C=O stretching vibration in the urethane bond (amide I band). The absorbance at 1531 cm^{-1} in the IR spectrum of TPU could be attributed to the coupling of N–H bending vibration with C–N stretching vibration in the –C–NH group (amide II band) [35, 36]. The weaker vibration band at 1314 cm^{-1} corresponds to the combination between N–H bending vibration and C–N stretching vibration (amide III band) [35]. The region 1300–1100 cm^{-1} is characteristic to C–O stretching vibrations in esters. The skeletal vibration of C=C in the aromatic ring from 1597 cm^{-1} can be coupled with the absorbance from 814 cm^{-1}, the last being characteristic to C–H out of plane bending vibration in 1,4-disubstituted aromatic ring [37].While the IR spectra of the samples treated below 200°C turn out to be similar to that of the neat TPU, the polymer, which underwent a thermal treatment at 200°C online in the IR cell, shows some differences. Indeed, the band between 3600 and 3200 cm^{-1} is modified, with the appearance of a shoulder at 3400 cm^{-1}, while a new peak at ca. 2260 cm^{-1}appears. The former band can be assigned to hydroxyl group, whereas the one at higher wavenumbers to isocyanate group formation [35].

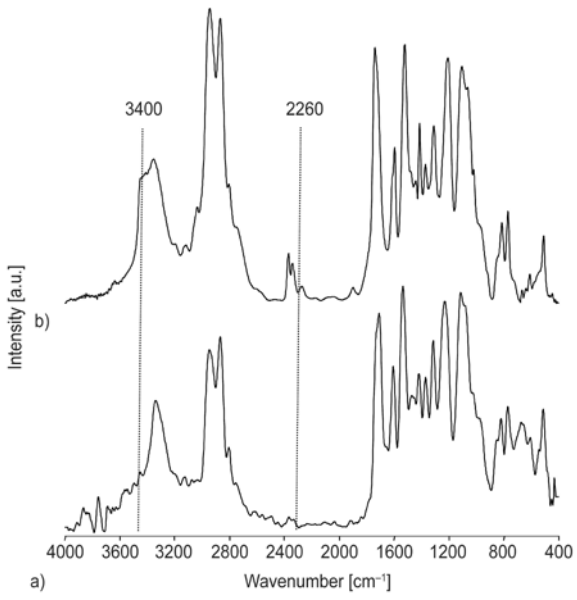

Figure 3. FTIR spectra of (a) TPU and (b) TPU at 200°C (inert atmosphere)

Moreover, the stability of the polymer matrix molecular mass, evaluated by viscosity measurements, further supports the above mechanism, the relative viscosity of the pristine TPU and that of the treated sample being equivalent, namely 1.42 and 1.41, respectively.

These findings suggest that the occurrence of the chain scission reaction reported in Figure 2 is indeed an equilibrium reaction, which is weakly shifted towards the dissociated form when increasing the temperature. Therefore, in the presence of POSS-OH, reaction of isocyanate groups with POSS is possible, also depending on the reactivity ratio between POSS moieties and OH-terminated polymer chains.

3.2. Study of hybrid systems characteristics

The polymer matrix was contacted with various amounts of an hydroxyl-functionalized POSS (from 2 to 20 wt%) and, as a comparison, with 10 wt% of isobutyl-POSS at 200°C. Up to 10 wt% the hybrids turned out to be homogeneous, whereas the sample blend containing 20 wt% of POSS-OH (TPU/POSS-OH(20)) clearly showed two separated phases at the micron scale. In the case of the sample based on isobutyl-POSS, (TPU/oib-POSS(10)), a solvent capable to swell the polymer and completely solubilize POSS molecules was found to extract the POSS entirely, evidencing the efficiency of the experimental procedure for the extraction of unbound silsesquioxanes. Conversely, for TPU/POSS(10),

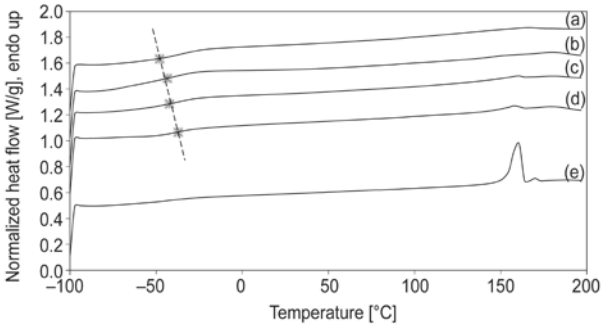

Figure 4. DSC traces on heating for: (a) TPU (T_g = –48°C), (b) TPU/POSS-OH(2) (T_g = –43°C), (c) TPU/POSS-OH(5) (T_g = –42°C), (d) TPU/POSS-OH(10) (T_g = –37°C), (e) POSS-OH

containing 10 wt% of POSS-OH (soluble in the same solvent), the extraction treatment seems to eliminate only a fraction of the silsesquioxane mixed with the polymer, which is only 20% of the total POSS content for TPU/POSS-OH(10). Moreover, in the case of TPU/POSS-OH(5) and TPU/POSS-OH(2) the reaction yield is almost 100%. This demonstrates the covalent bonding of POSS-OH to the TPU chain, evidencing that the reactivity of the silsesquioxane is essential for the formation of a hybrid system.

DSC traces of the different TPU/POSS-OH prepared are given in Figure 4, in comparison with pristine TPU and POSS-OH.

The pristine TPU displays a glass transition at −48°C, which is typical for this kind of polymer. By analyzing these results, it comes out that a modification of T_g with respect to that of the neat polymer matrix occurs even for the samples with low concentration of POSS-OH (TPU/POSS-OH(2)). In particular, the TPU/POSS-OH sample T_g increases with increasing the silsesquioxane content, while in the case of TPU/oib-POSS(10), namely the system containing the unreactive POSS, the glass transition temperature remains constant. This behavior might be related to the scarce interaction between the isobutyl-POSS and the polymer matrix, as demonstrated by yield data.

Taking into account the literature findings [38–40], it is possible to interpret the increase of the glass transition temperature of our TPU/POSS systems on the basis of hindrance of polymer chain mobility induced by the presence of relatively bulky POSS cages. Moreover, for our polymer matrix, which consists of a hard and a soft segment phase, as reported in the literature [29], the relevant increase of T_g at low temperature with increasing the POSS content can be ascribed to the portioning of silsesquioxane molecules into the soft segment phase.

It is worth to underline the presence of a very small peak in the DSC trace of TPU/POSS-OH(5), which is more evident for the sample TPU/POSS-OH(10). This peak can be ascribed to the melting of unbound POSS, as it not observable in the plots for samples which underwent a washing treatment to remove the unbound POSS.

In order to accurately evaluate the sample microphase morphology, TEM analysis was preformed. Figure 5 shows a comparison between TEM micrographs of the neat TPU and TPU/POSS-OH(5) surface which underwent the washing treatment.

It is clearly evident from this figure that the morphology of TPU/POSS-OH(5) does not show any segregation or aggregation of POSS particles, thus indicating that POSS-OH is chemically reacted with the polymer. Moreover, Si concentration has been found to be homogenous. A clear microphase-separated structure can be observed for both samples. However, the presence of POSS turns out to modify the microphase morphology, as neat TPU surface shows a finer structure compare to TPU/POSS-OH(5). Indeed, the dimension of domains seems to increase in the POSS-based TPU, evidencing that

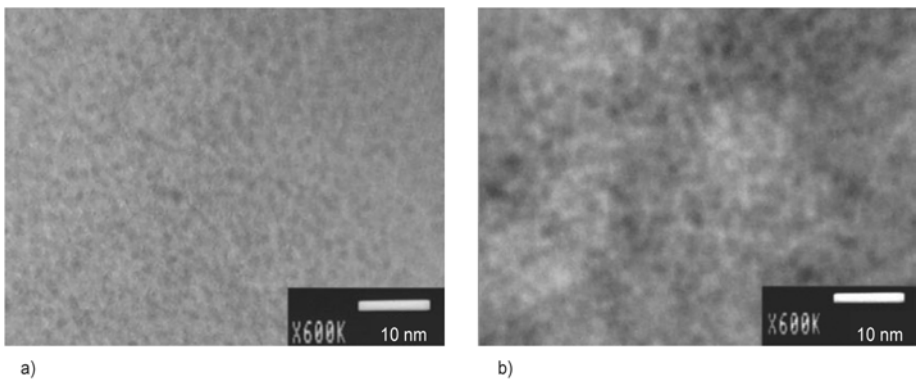

Figure 5. TEM micrographs of: (a) TPU and (b) TPU/POSS-OH(5)

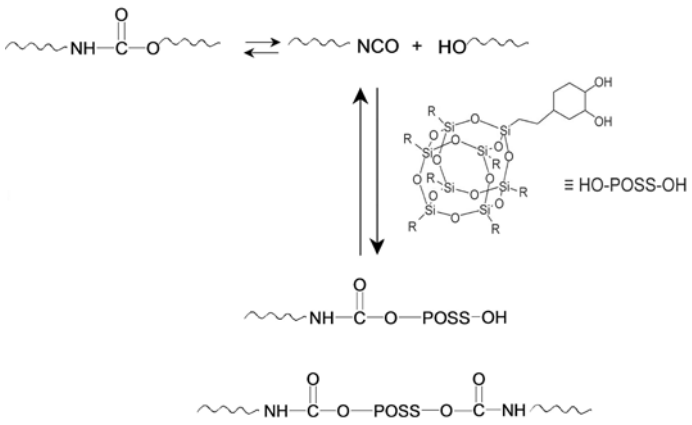

Figure 6. Reaction scheme

the silsesquioxane is capable of modifying the polymer microphase morphology, as previously reported in the literature [41]. On the basis of the results obtained, it is possible to hypothesize that the reaction between the polymer functional groups, formed during the melt blending, and POSS functionalities follows the mechanism shown in Figure 6.

Indeed, it is possible to suppose that both the silsesquioxane hydroxyl functionalities react with the polymer isocyanate groups, produced by chain scission, leading to POSS insertion inside the macromolecular chains or the reaction of only one of the two OH groups, forming POSS-ended chains. The effect of POSS as chain terminator is supported by the viscosity measurements, the relative viscosity of the pristine TPU and TPU/POSS-OH(10) being 1.41 and 1.21, respectively.

Another property of the materials prepared, which was investigated by contact angle measurements, was the wettability. Indeed, water contact angle was measured on the surface of TPU/POSS-OH films up to 10% POSS, which underwent a washing treatment. While the contact angle of pristine TPU is about 95°, a strong reduction was obtained in the presence of POSS, to about 85 and 70° for 5% and 10% POSS loadings, respectively. This can be explained by the hydrophilicity introduced by OH groups on POSS, which are present also in the hybrids because of the formation of POSS-ended chains characterized by a hydroxyl group.

4. Conclusions

In this work, a novel approach for the preparation of POSS-based hybrids has been assessed. The method studied turns out to be simple, being based on reactive melting, and it is applicable to polymers which do not carry reactive side groups. Indeed, the approach consists in the reaction between silsesquioxane molecules and the macromolecule functional groups, which are formed directly during the melt blending process through a controlled scission of the polymer matrix.

In the case of TPU, it has been verified that the thermal degradation of the urethane segment, which occurs directly in a mixer under controlled atmosphere by depolymerization leads to the formation of isocyanate groups. The blending with silsesquioxane molecules, characterized by hydroxyl groups, leads to the formation of systems consisting of silsesquioxane molecules directly attached to the macromolecular chain which modify the TPU microphase morphology. The presence of POSS has been found to affect significantly the polymer glass transition temperature, as it increases by increasing POSS concentration, this phenomenon being related to the effect of POSS on the macromolecular motion and to the partitioning of silsesquioxane molecules into the soft segment phase.

The presence of POSS has turned out to increase film hydrophilicity.

Acknowledgements

We are grateful to the Italian Ministry of Education and University through the 2010-2011 PRIN project (Grant No. 2010XLLNM3_005).

References

[1] Cordes D. B., Lickiss P. D., Rataboul F.: Recent developments in the chemistry of cubic polyhedral oligosilsesquioxanes. Chemical Reviews, **110**, 2081–2173 (2010).
DOI: 10.1021/cr900201r

[2] Baney R. H., Itoh M., Sakakibara A., Suzuki T.: Silsesquioxanes. Chemical Reviews, **95**, 1409–1430 (1995).
DOI: 10.1021/cr00037a012

[3] Valentini L., Bittolo Bon S., Monticelli O., Kenny J. M.: Deposition of amino-functionalized polyhedral oligomeric silsesquioxanes on graphene oxide sheets immobilized onto an amino-silane modified silicon surface. Journal of Materials Chemistry, **22**, 6213–6217 (2012).
DOI: 10.1039/C2JM16111G

[4] Blanco I., Abate L., Antonelli M. L., Bottino F. A., Bottino P.: Phenyl hepta cyclopentyl – polyhedral oligomeric silsesquioxane (ph,hcp-POSS)/polystyrene (PS) nanocomposites: The influence of substituents in the phenyl group on the thermal stability. Express Polymer Letters, **6**, 997–1006 (2012).
DOI: 10.3144/expresspolymlett.2012.105

[5] Carniato F., Bisio C., Gatti G., Boccaleri E., Bertinetti E., Coluccia S., Monticelli O., Marchese L.: Titanosilsesquioxanes embedded in synthetic clay as a hybrid material for polymer science. Angewandte Chemie International Edition, **48**, 6059–6061 (2009).
DOI: 10.1002/anie.200901927

[6] Tanaka K., Chujo Y.: Advanced functional materials based on polyhedral oligomeric silsesquioxane (POSS). Journal of Materials Chemistry, **22**, 1733–1746 (2012).
DOI: 10.1039/C1JM14231C

[7] Baldi F., Bignotti F., Ricco L., Monticelli O., Riccò T.: Mechanical and structural characterization of POSS-modified polyamide 6. Journal of Applied Polymer Science, **100**, 3409–3414 (2006).
DOI: 10.1002/app.23804

[8] Dintcheva N. Tz., Morici E., Arrigo R., La Mantia F. P., Malatesta V., Schwab J. J.: Structure-properties relationships of polyhedral oligomeric silsesquioxane (POSS) filled PS nanocomposites. Express Polymer Letters, **6**, 561–571 (2012).
DOI: 10.3144/expresspolymlett.2012.59

[9] Vannier A., Duquesne S., Bourbigot S., Castrovinci A., Camino G., Delobel R.: The use of POSS as synergist in intumescent recycled poly(ethylene terephthalate). Polymer Degradation and Stability, **93**, 818–826 (2008).
DOI: 10.1016/j.polymdegradstab.2008.01.016

[10] Phillips S. H., Haddad T. S., Tomczak S. J.: Developments in nanoscience: Polyhedral oligomeric silsesquioxane (POSS)-polymers. Current Opinion in Solid State and Materials Science, **8**, 21–29 (2004).
DOI: 10.1016/j.cossms.2004.03.002

[11] Li G., Wang L., Ni H., Pittman C. U. Jr.: Polyhedral oligomeric silsesquioxane (POSS) polymers and copolymers: A review. Journal of Inorganic and Organometallic Polymers, **11**, 123–154 (2001).
DOI: 10.1023/A:1015287910502

[12] Monticelli O., Cavallo D., Bocchini S., Frache A., Carniato F., Tonelotto A.: A novel use of Ti-POSS as initiator of L-lactide ring-opening polymerization. Journal of Polymer Science Part A: Polymer Chemistry, **49**, 4794–4799 (2011).
DOI: 10.1002/pola.24926

[13] Fina A., Tabuani D., Frache A., Camino G.: Polypropylene–polyhedral oligomeric silsesquioxanes (POSS) nanocomposites. Polymer, **46**, 7855–7866 (2005).
DOI: 10.1016/j.polymer.2005.06.121

[14] Fu B. X., Gelfer M. Y., Hsiao B. S., Phillips S., Viers B., Blanski R., Ruth P.: Physical gelation in ethylene–propylene copolymer melts induced by polyhedral oligomeric silsesquioxane (POSS) molecules. Polymer, **44**, 1499–1506 (2003).
DOI: 10.1016/S0032-3861(03)00018-1

[15] Hosaka N., Otsuka H., Hino M., Takahara A.: Control of dispersion state of silsesquioxane nanofillers for stabilization of polystyrene thin films. Langmuir, **24**, 5766–5772 (2008).
DOI: 10.1021/la704062n

[16] Hao N., Böhning M., Schönhals A.: Dielectric properties of nanocomposites based on polystyrene and polyhedral oligomeric phenethyl-silsesquioxanes. Macromolecules, **40**, 9672–9679 (2007).
DOI: 10.1021/ma071777g

[17] Monticelli O., Fina A., Cozza E. S., Prato M., Bruzzo V.: POSS vapor phase grafting: A novel method to modify polymer films. Journal of Materials Chemistry, **21**, 18049–18054 (2011).
DOI: 10.1039/C1JM13553H

[18] Fina A., Monticelli O., Camino G.: POSS-based hybrids by melt/reactive blending. Journal of Materials Chemistry, **20**, 9297–9305 (2010).
DOI: 10.1039/C0JM00480D

[19] Monticelli O., Fina A., Ullah A., Waghmare P.: Preparation, characterization, and properties of novel PSMA–POSS systems by reactive blending. Macromolecules, **42**, 6614–6623 (2009).
DOI: 10.1021/ma900969b

[20] Kim B-S., Mather P. T.: Amphiphilic telechelics incorporating polyhedral oligosilsesquioxane: 1. Synthesis and characterization. Macromolecules, **35**, 8378–8384 (2002).
DOI: 10.1021/ma020226h

[21] Kim B-S., Mather P. T.: Amphiphilic telechelics with polyhedral oligosilsesquioxane (POSS) end-groups: Dilute solution viscometry. Polymer, **47**, 6202–6207 (2006).
DOI: 10.1016/j.polymer.2006.06.050

[22] Dvornic P. R., Hartmann-Thompson C., Keinath S. E., Hill E. J.: Organic–inorganic polyamidoamine (PAMAM) dendrimer–polyhedral oligosilsesquioxane (POSS) nanohybrids. Macromolecules, **37**, 7818–7831 (2004).
DOI: 10.1021/ma030542b

[23] Fu B. X., Zhang W., Hsiao B. S., Rafailovich M., Sokolov J., Johansson G., Sauer B. B., Phillips S., Balnski R.: Synthesis and characterization of segmented polyurethanes containing polyhedral oligomeric silsesquioxanes nanostructured molecules. High Performance Polymer, **12**, 565–571 (2000).
DOI: 10.1088/0954-0083/12/4/311

[24] Fu B. X., Hsiao B. S., White H., Rafailovich M., Mather P. T., Jeon H. G., Phillips S., Lichtenhan J., Schwab J.: Nanoscale reinforcement of polyhedral oligomeric silsesquioxane (POSS) in polyurethane elastomer. Polymer International, **49**, 437–440 (2000). DOI: 10.1002/(SICI)1097-0126(200005)49:5<437::AID-PI239>3.0.CO;2-1

[25] Fu B. X., Hsiao B. S., Pagola S., Stephens P., White H., Rafailovich M., Sokolov J., Mather P. T., Jeon H. G., Phillips S., Lichtenhan J., Schwab J.: Structural development during deformation of polyurethane containing polyhedral oligomeric silsesquioxanes (POSS) molecules. Polymer, **42**, 599–611 (2001). DOI: 10.1016/S0032-3861(00)00389-X

[26] Turri S., Levi M.: Structure, structure, dynamic properties, and surface behavior of nanostructured ionomeric polyurethanes from reactive polyhedral oligomeric silsesquioxanes. Macromolecules, **38**, 5569–5574 (2005). DOI: 10.1021/ma047304g

[27] Knight P. T., Lee K. M., Qin H., Mather P. T.: Biodegradable thermoplastic polyurethanes incorporating polyhedral oligosilsesquioxane. Biomacromolecules, **9**, 2458–2467 (2008). DOI: 10.1021/bm8004935

[28] Wu J., Ge Q., Mather P. T.: PEG–POSS multiblock polyurethanes: Synthesis, characterization, and hydrogel formation. Macromolecules, **43**, 7637–7649 (2010). DOI: 10.1021/ma101336c

[29] Nanda A. K., Wicks D. A., Madbouly S. A., Otaigbe J. U.: Nanostructured polyurethane/POSS hybrid aqueous dispersions prepared by homogeneous solution polymerization. Macromolecules, **39**, 7037–7043 (2006). DOI: 10.1021/ma060809h

[30] Oaten M., Choudhury N. R.: Silsesquioxane–urethane hybrid for thin film applications. Macromolecules, **38**, 6392–6401 (2005). DOI: 10.1021/ma0476543

[31] Neumann D., Fisher M., Tran L., Matisons J. G.: Synthesis and characterization of an isocyanate functionalized polyhedral oligosilsesquioxane and the subsequent formation of an organic–inorganic hybrid polyurethane. Journal of the American Chemical Society, **124**, 13998–13999 (2002). DOI: 10.1021/ja0275921

[32] Liu H., Zheng S.: Polyurethane networks nanoreinforced by polyhedral oligomeric silsesquioxane. Macromolecular Rapid Communication, **26**, 196–200 (2005). DOI: 10.1002/marc.200400465

[33] Bourbigot S., Turf T., Bellayer S., Duquesne S.: Polyhedral oligomeric silsesquioxane as flame retardant for thermoplastic polyurethane. Polymer Degradation and Stability, **94**, 1230–1237 (2009). DOI: 10.1016/j.polymdegradstab.2009.04.016

[34] Chattopadhyay D. K., Webster D. C.: Thermal stability and flame retardancy of polyurethanes. Progress in Polymer Science, **34**, 1068–1133 (2009). DOI: 10.1016/j.progpolymsci.2009.06.002

[35] Silverstein R. M., Webster F. X., Klemie D. J.: Spectrometric identification of organic compounds. Wiley, New York (2005).

[36] Stuart B.: Infrared spectroscopy. Fundamental and applications. Wiley, New York (2004).

[37] Lin-Vien D., Colthup N. B., Fateley W. G., Grasselli J. G.: The handbook of infrared and Raman characteristic frequencies of organic molecules. Academic Press, Boston (1991).

[38] Bharadwaj R. K., Berry R. J., Farmer B. L.: Molecular dynamics simulation study of norbornene–POSS polymers. Polymer, **41**, 7209–7221 (2000). DOI: 10.1016/S0032-3861(00)00072-0

[39] Lee A., Lichtenhan J. D.: Viscoelastic responses of polyhedral oligosilsesquioxane reinforced epoxy systems. Macromolecules, **31**, 4970–4974 (1998). DOI: 10.1021/ma9800764

[40] Raftopoulos K. N., Pandis Ch., Apekis L., Pissis P., Janowski B., Pielichowski K., Jaczewska J.: Polyurethane–POSS hybrids: Molecular dynamics studies. Polymer, **51**, 709–718 (2010). DOI: 10.1016/j.polymer.2009.11.067

[41] Madbouly S. A., Otaigbe J. U., Nanda A. K., Wicks D. A.: Rheological behavior of POSS/polyurethane–urea nanocomposite films prepared by homogeneous solution polymerization in aqueous dispersions. Macromolecules, **40**, 4982–4991 (2007). DOI: 10.1021/ma070186n

eXPRESS Polymer Letters Vol.7, No.12 (2013) 974–983
Available online at www.expresspolymlett.com
DOI: 10.3144/expresspolymlett.2013.96

Preparation and characterization of a stereocomplex of poly(lactide-co-ε-caprolactone)/tricalcium phosphate biocomposite using supercritical fluid technology

R. I. Nurqadar[1,2], *P. Purnama*[1], *S. H. Kim*[1,2,3*]

[1]Biomaterials Research Center, Korea Institute of Science and Technology, 136-791 Seoul, Korea
[2]Biomedical Engineering, University of Science and Technology, 113 Gwahangno, Yuseong-gu, 305-333 Daejeon, Korea
[3]KU-KIST Graduate School of Converging Science and Technology, Korea University, 136-701 Seoul, Korea

Received 30 May 2013; accepted in revised form 13 August 2013

Abstract. A novel biocomposite material from a stereocomplex of poly (L-lactide-co-ε-caprolactone) (PLLCL) and poly (D-lactide-co-ε-caprolactone) (PDLCL) and inorganic tricalcium phosphate (TCP) was prepared by supercritical fluid method. Both pristine and poly (L-lactide)-grafted-TCP (PLLA-g-TCP) were used. PLLA-g-TCP was produced by ring-opening polymerization of L-lactide in the presence of surface-activated TCP. Infrared (IR) spectroscopy and scanning electron microscopic (SEM) images confirm the attachment of PLLA onto the activated TCP surface. The stereocomplex formation of biocomposite was confirmed by differential scanning calorimetry (DSC) and wide-angle X-ray diffraction (WAXD). The biocomposite containing PLLA-g-TCP has higher stereocomplex degree and more homogeneous TCP distribution compared to the biocomposite containing pristine TCP. The presence of PLLA-g-TCP in the stereocomplex PLLCL-PDLCL (s-PDLCL) enhance the stereocomplex degree up to a certain content and also supports the homogeneous TCP dispersion in the stereocomplex matrix. These phenomena support the improvement in mechanical properties of the s-PDLCL composite the optimum content of PLLA-g-TCP being 10%. The biocomposites containing TCP materials are promising materials for biomedical application, especially for bone tissue engineering.

Keywords: *biocomposites, polylactide, biodegradable polymers, stereocomplex*

1. Introduction

Absorbable materials are attractive for internal fracture fixation devices. They have advantages in the reduction of stress shielding, secondary operations for removal are no longer required, and the risks of complications are reduced [1]. Biopolymers such as polylactide, poly(glycolic acid), poly(ε-caprolactone), and their copolymers attract great attention due to their biodegradability and biocompatibility. The major limitation of those materials is that their mechanical properties (as strength, toughness, elastic modulus) are lower than the mechanical properties of cortical bones.

Polylactide-based materials have attracted great interest due to their capability to form stereocomplex. Stereocomplex can be formed by interaction between L-lactide and D-lactide fragments with minimum length of about 7 lactide units [2]. The stereocomplexation caused by interaction of L- and D-lactide sequences affect the mechanical and thermal properties of polylactide [3]. The linear stereocomplex polylactide has limitation in melt stability. This drawback can be reduced by adding flexible fragments such as ε-caprolactone to the polylactide [4]. Improvement in mechanical and thermal performance of polylactide by stereocomplexation still

*Corresponding author, e-mail: soohkim@kist.re.kr

does not match with cortical bone level. For this reason, there are many developments to prepare absorbable material with proper mechanical properties to match natural bones by combining biodegradable polymers and inorganic fillers.

There are many inorganic fillers capable of improving the mechanical performance and bioactivity of composites such as hydroxyapatite, TCP, bioactive glass, bioactive glass ceramics, and calcium silicate [5–9]. Bioresorbable TCP material has been used as bone substitute due to its biocompatibility and osteoconductivity [10, 11].

In this report, we prepare new hybrid materials by combining stereocomplexation of PLLCL and PDLCL in the presence of TCP by supercritical fluid method. Here, we compare the non-grafted (pristine) TCP and PLLA-g-TCP as fillers in the stereocomplex matrix. The biocomposite from surface-modified TCP and stereocomplex matrix exhibits higher mechanical and thermal properties than the biocomposite from pristine TCP and stereocomplex matrix.

2. Experimental section

2.1. Materials

PDLCL (M_n = 96,249 g/mol, M_w = 239,118 g/mol, PDI = 2.484, where PDI denotes the polydisperisty index) and PLLCL (M_n = 114,602 g/mol, M_w = 252,362 g/mol, PDI = 2.202) with 10% mol of ε-caprolactone were synthesized by bulk polymerization in Biomaterial Research Center, Korea Institute of Science and Technology (KIST). TCP hydrate nano-powder (MFCD00015984) (Sigma-Aldrich, <200 nm particle size, determined by the Brunauer-Emmet-Tell/BET/method, USA) and phosphoric acid (MFCD00011340) (Sigma-Aldrich, 85 wt%, USA), methylene chloride (9315-03) (JT Baker, HPLC grade, USA), and L-lactide (CAS No. 4511-42-6) (Medichem Chemical Co., Ltd., Korea, minimum purity 99.9%) and carbon dioxide (CO_2) (Shin Yang Oxygen Industry Co. Ltd., minimum purity 99.9%, South Korea) were used as received.

2.2. Grafting of lactide onto surface-modified TCP

The surface-modified TCP was obtained by a method similar to one already described in the literature [12]. Briefly; TCP hydrate was vacuumed at 80°C for 24 hours before use. TCP powder was added to 5% aqueous phosphoric acid solutions (1:2 w/w) and stirred at room temperature for 1 hour. The precipitate was removed from the solution by centrifugal separation. These powders were washed five times with distilled water to completely remove free residual PO_4^{3-} ions, and dried at 60°C under vacuum before used. Evacuation was used to minimize residual water in order to reduce the formation of ungrafted PLLA and L-lactide hydrolisis [13, 14].

The dry surface-modified TCP powder was grafted by L-lactide through ring-opening polymerization using stannous octoate as catalyst. 8.4 g of L-lactide was mixed with 1 g of surface-modified TCP (molar ratio 1:10) and stannous octoate (0.05 wt%) in a glass ampoule. The polymerization was carried out at 130°C for 36 and 96 hours. The product then washed by chloroform to separate the non-grafted PLLA, filtered, and dried at 50°C under vacuum. The polymerization resulted in PLLA-g-TCP.

2.3. Preparation of stereocomplex-TCP biocomposites

The formation of stereocomplex-TCP biocomposite was carried out by method using supercritical CO_2-methylene chloride similar to that described earlier [16]. A blend of PLLCL 10% and PDLCL 10% (weight ratio 1:1) was mixed with surface-modified TCP or pristine TCP and placed into a 40 mL stainless steel high pressure reactor equipped with a magnetic stirrer and electronic heating equipment. Methylene chloride was added to the reactor by syringe, and then the reactor was connected to the supercritical fluid apparatus. The reactor was filled with liquid CO_2 at 30°C and 100 bar then gradually heated until reaching 65°C and 350 bar. The methylene chloride to CO_2 ratio is 30:70 (wt%). The reaction process was allowed to proceed for the predetermined times (5 h) and the reactor was opened immediately after the reaction had finished.

2.4. Characterization

Surface modification of TCP was analyzed by IR spectrometer Nicolet iS10 (Thermo SCIENTIFIC). Polymer grafted onto the surface of TCP was confirmed by ToF-SIMS (time of flight secondary ion mass spectroscopy) analysis using ToF-SIMS 5 (ION-TOF). Thermal gravimetric analysis (TGA) was conducted on a Hi-Res TGA 2950 (TA Instrument, USA) under N_2 flow at a heating rate of 10°C/min. Stereocomplex-composites formation

was monitored by DSC (differential scanning calorimetry) using a DSC Q20 (TA Instrument, USA) under a N_2 flow of 50 mL/min at a heating rate 10°C/min. The crystalline structure of stereocomplex-composites with grafted or non-grafted TCP at varied content was analyzed by WAXD (wide angle X-ray diffraction), recorded on X-ray diffractometer Rigaku D/Max-2500 composed of Cu K_α (λ = 1.54056 Å, 30 kV, 100 mA) source, a quartz monochromator, and a goniometric plate. The mechanical properties of biocomposites were measured by an Instron apparatus with specimen size was 20 × 5 mm, and sample thickness about 10 μm. The distance between supports was 10 mm and the extension rate was 1 mm/min for extension rate. Scanning electron microscopy (SEM) was used to evaluate the morphology of surface-modified TCP and TCP filler distribution in stereocomplex matrix using a FEI SEM INSPECT F50 (FEI).

3. Results and discussion

The attachment of inorganic materials to the polymer matrix is an important point in composite systems. Thus, surface-modification or polymer grafting is useful to improve the miscibility of those materials.

The surface activation followed by polymer grafting was applied to TCP materials. IR spectra were used to evaluate TCP, surface-activated TCP, PLLA, and PLLA-g-TCP as shown in Figure 1.

The surface-activated TCP was successfully synthesized from pristine TCP. The characteristic alterations in IR spectrum of surface-activated TCP in comparison with pristine TCP are observable. At the wavenumber below 1000 cm^{-1}, the surface-activated TCP shows different spectrum at 643, 933, and 997 cm^{-1} which correspond to O–P–O bending or H_2O waging, P–O stretching, and H_2O rocking, respectively [12]. Low intensity of O–H valence band in the region 3100–3600 cm^{-1} and band of crystal water of surface-activated TCP were clearly observed. The neat PLLA has the characteristic carbonyl band at 1750 cm^{-1}, C–H stretching band at 2920 and 3000 cm^{-1}, and C–H bending band at 1450 and 1360 cm^{-1} [13, 14]. The IR spectrum PLLA-g-TCP shows that PLLA was successfully grafted onto TCP surfaces. It can be seen as the dissapearance of hydroxyl band (3100–3600 cm^{-1}) and the presence of small absorbance of carbonyl band, C–H stretching, C–H bending which come from PLLA characteristics.

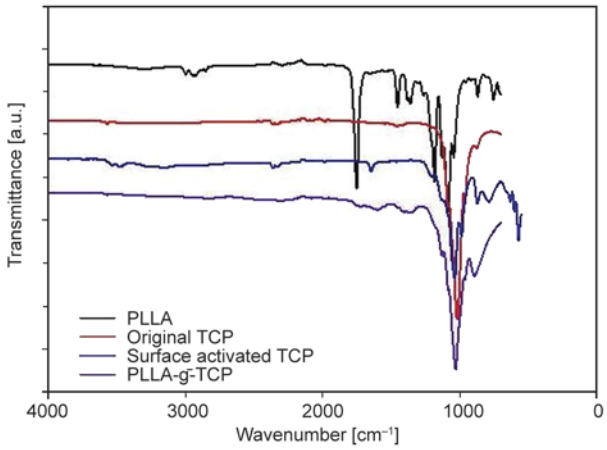

Figure 1. IR spectra of pristine TCP, surface-activated TCP, PLLA-g-TCP, and neat PLLA

The appearance of PLLA-g-TCP was shown in Figure 2. PLLA-g-TCP was successfully obtained by ring-opening polymerization by stannous octoate for 36 and 96 h. The generated PLLA grafted TCPs from 36 and 96 h polymerization time were denoted as PLLA-g-TCP36 and PLLA-g-TCP96, respec-

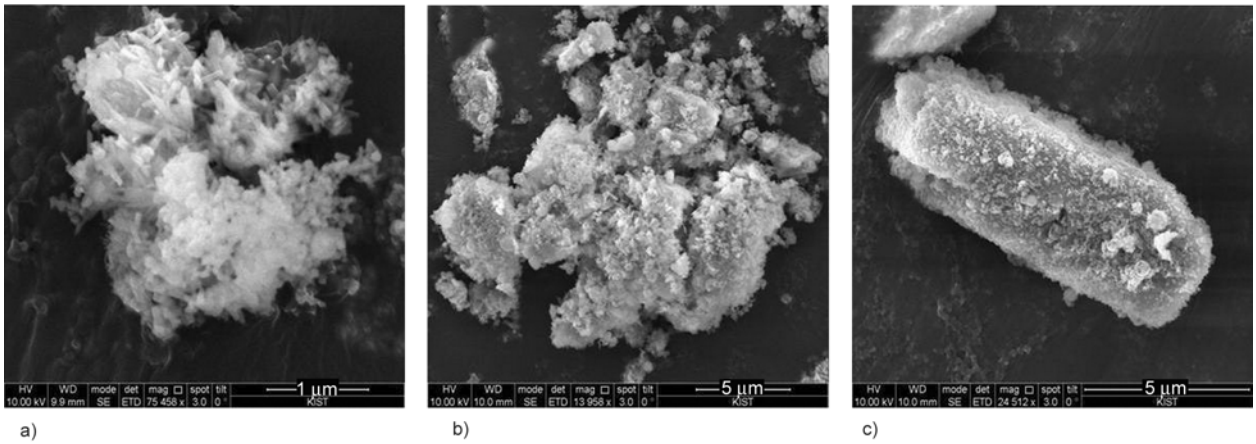

Figure 2. SEM images: a) pristine TCP (scale bar = 1 μm); b) PLLA-g-TCP36 (scale bar = 5 μm); c) PLLA-g-TCP96 (scale bar = 5 μm)

tively. The PLLA growth from the hydroxyl group on the activated TCP surfaces which acts as initiator. From the SEM picture, the PLLA fully attached to the activated TCP surfaces for PLLA-g-TCP36 and PLLA-g-TCP96. The attachment of PLLA chain onto TCP surface was also confirmed by ToF-SIMS analysis. The negative ion spectra of TCP powder show the characteristic fragments of TCP (Figure 3). Characteristic peaks were observed at *m*/*z* 31, 47, 36, and 79, corresponding to P^-, PO^-, PO_2^-, and PO_3^- respectively. It can be seen that the spectrum is dominated by the phosphor containing fragments. Other fragment containing Ca was found at *m*/*z* 119 attributed to $CaPO_3^-$ which is consistent with the typical spectrum of hydroxyapatite [15]. Figure 4 shows distinct series of ions characteristic of hydroxyapatite in this mass region. The low mass ions at *m*/*z* 16 and 17 correspond to O^- and OH^-, respectively. In the *m*/*z* region between 100 and 120, there are two fragments $C_3H_4O_2P^-$ (*m*/*z* 103) and $CaPO–C_2H_4^-$ (*m*/*z* 115) which and related as characteristic fragments of grafted TCP. A peak at *m*/*z* 144 is ascribed to $C_6H_8O_4^-$ or single fragment of L-lactide. Another fragment containing phosphor was found at *m*/*z* 175 ($C_6H_8O_4P^-$). The peak intensity of PLLA-g-TCP96 is higher than PLLA-g-TCP36 which means the grafted PLLA content in the PLLA-g-TCP96 is higher than PLLA-g-TCP36. Further evaluation has been done by TGA to evaluate the amount of grafted PLLA as depicted in Figure 5. The grafting degree of PLLA onto activated TCP surface was quantitatively determined by the total mass loss of PLLA-g-TCP. The grafting degree depends on the reaction time. PLLA-g-TCP96 has a grafting degree (~12%) higher than PLLA-g-TCP36 (~8%). This indicates that PLLA-g-TCP96 has more grafted PLLA than PLLA-g-TCP36.

Stereocomplex-TCP biocomposites were prepared by combining PDLCL and PLLCL in the presence of TCP in supercritical CO_2-methylene chloride.

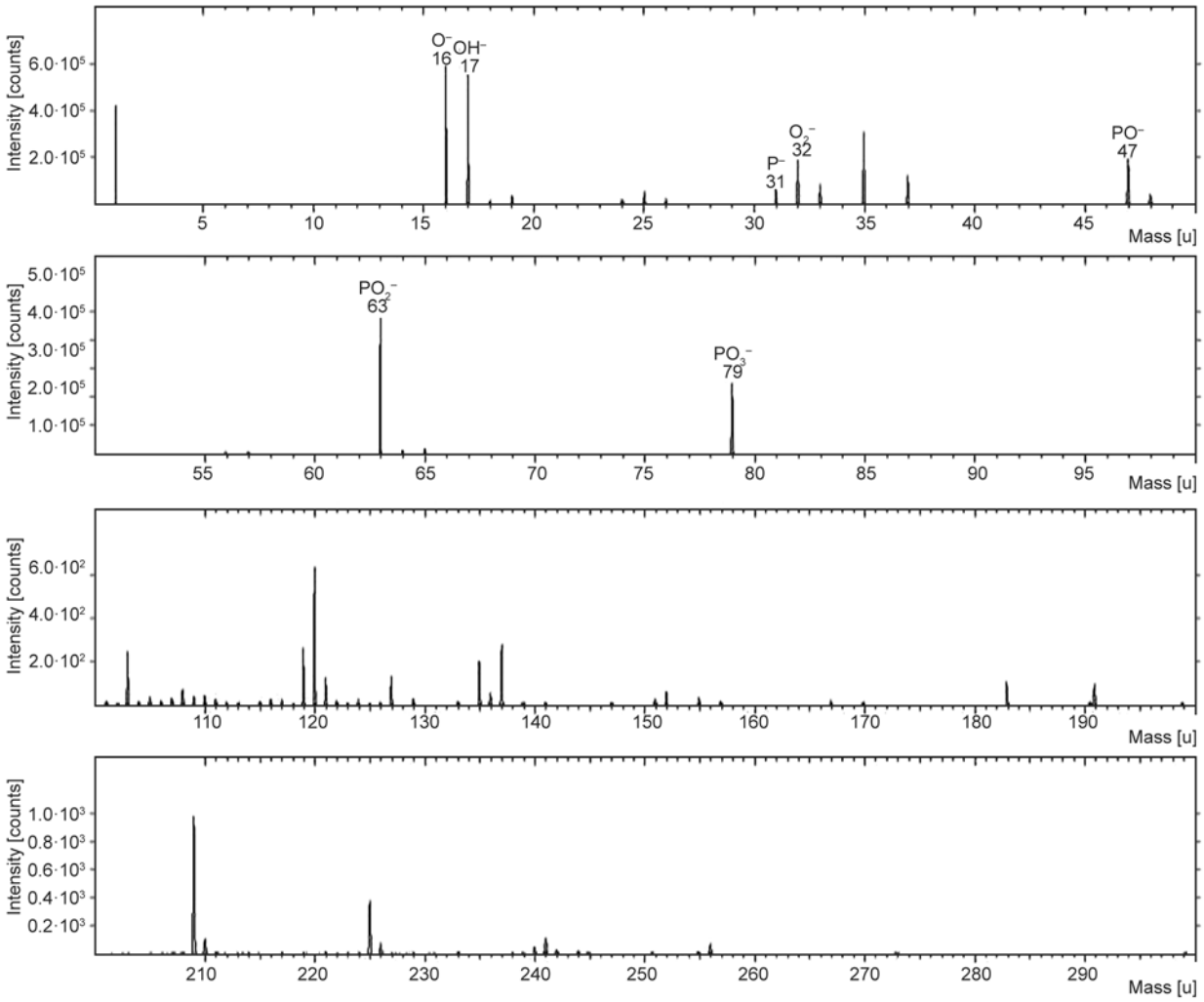

Figure 3. Negative ToF-SIMS spectrum of Pristine TCP

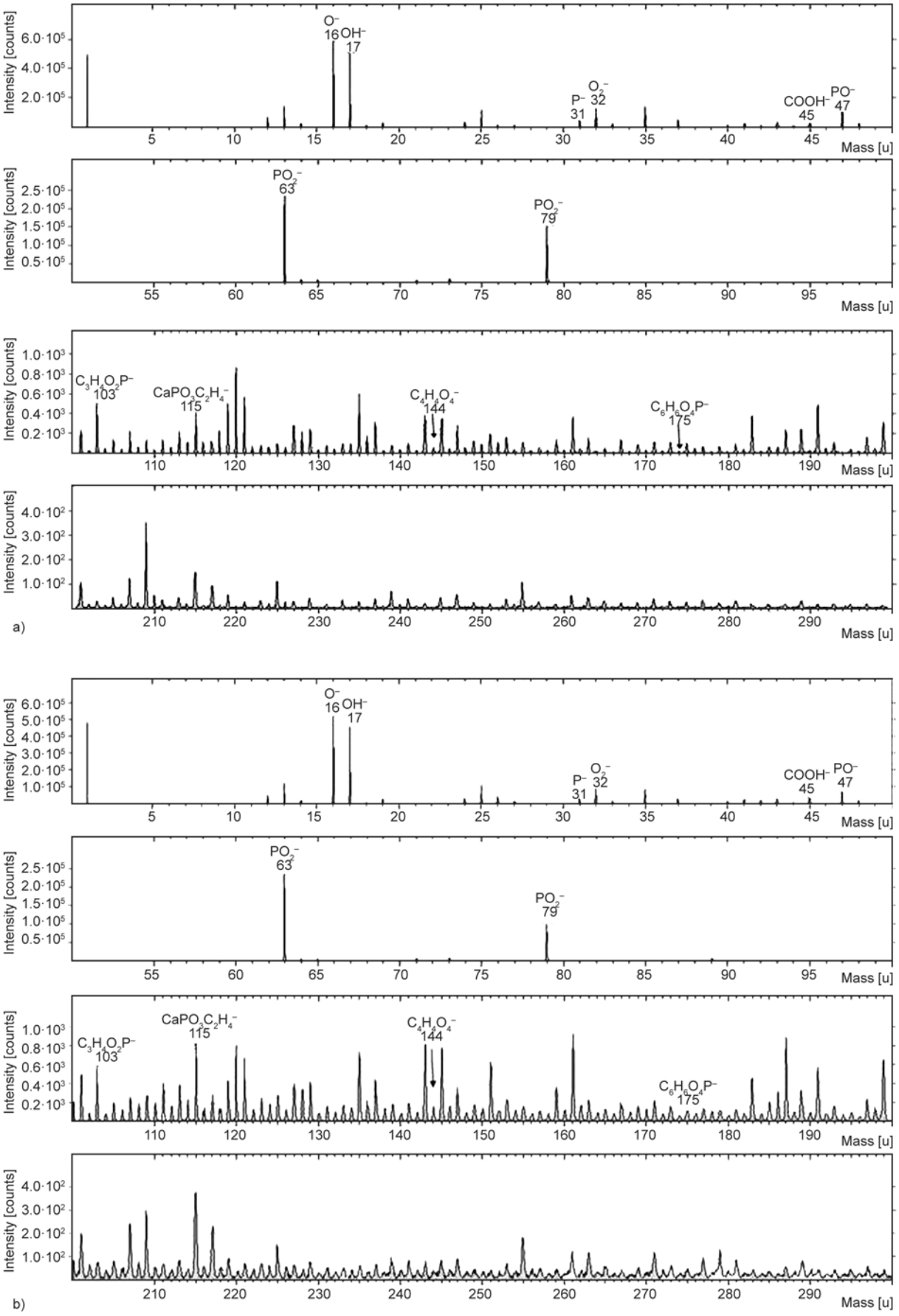

Figure 4. Negative ToF-SIMS spectra of PLLA-g-TCP36 (a) and PLLA-g-TCP96 (b)

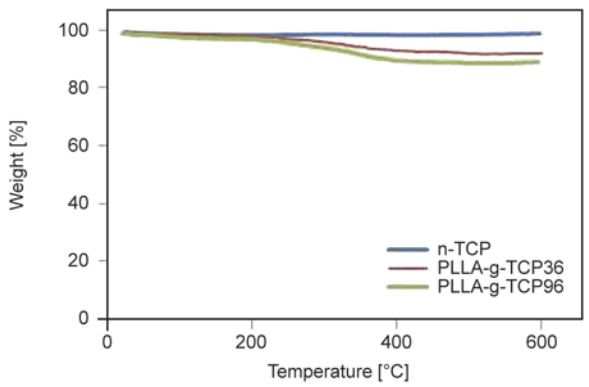

Figure 5. TGA thermograms of pristine TCP, PLLA-g-TCP36, and PLLA-g-TCP96

Due to the limited solubility of PDLCL and PLLCL in supercritical CO_2, methylene chloride was used as co-solvent to improve their solubility in supercritical CO_2 [16]. PLLA-g-TCP96 and pristine TCP were used as inorganic material for these biocomposites due to the fact that they contain more grafted PLLA on the activated TCP surfaces compared to PLLA-g-TCP36. The presence of grafted-PLLA on activated-TCP surfaces is expected to improve the physical properties of generated-biocomposites.

The stereocomplex degree was evaluated by comparing ΔH_m at the melting point (T_m) of the stereocomplex ($T_m > 200°C$) and their homopolymers ($T_m < 180°C$) from DSC anaysis. The neat s-PDLCL has a degree of stereocomplex of ~88.36%. It could not achieve 100% of stereocomplex during 5 h stereocomplexation processing time. As mentioned in the literature, the presence of ε-caprolactone fragments bothers the interaction between L- and D-lactide fragments to form stereocomplex [4]. In the biocomposite system, the presence of inorganic materials also affects the interaction with the polymer matrix [17].

The s-PDLCL containing PLLA-g-TCP96 (s-PDLCL/g-TCP) shows higher stereocomplex degree than s-PDLCL containing pristine TCP (s-PDLCL/TCP) as tabulated in Table 1. In the s-PDLCL/TCPs, the presence of TCP reduces the degree of stereocomplex in the biocomposite. At 5% TCP content, stereocomplex degree of s-PDLCL/TCP decreases drastically to about ~44%. The presence of ε-caprolactone fragments in the s-PDLCL results in decreasing stereocomplex degree compared to the streocomplex formed from polylactide homopolymer [4]. The presence of inorganic materials also caused a decreasing stereocomplex degree due to the interruption of the interaction between L- and D-lactide fragments to form stereocomplex [17]. The increasing TCP content decreases the stereocomplex degree proportionally. The increasing TCP content means the stereocomplex biocomposite system contains more particles which interfere with the stereocomplex formation. Thus, the presence of ε-caprolactone fragments and TCP materials simultaneously caused the decreasing stereocomplex degree. The heat of melting (ΔH_m) of s-PDLCL/g-TCP is higher than that of s-PDLCL/TCP. It is presumably caused by the nucleating effect of TCP particles in the polymer matrix. The PLLA-g-TCP exhibits better distribution in the polymer matrix than pristine TCP due to the presence of grafted-PLLA. The ΔH_m of biocomposite is lower than that of s-PDLCL. The crystallinity depends on the arrangement of polymer chains [20]. The presence of TCP particle interferes with the arrangement of the polymer chain, which leads to decreasing ΔH_m.

s-PDLCL/g-TCP exhibits different behavior from s-PDLCL/TCP. The presence of TCP materials in the PLLA-g-TCP96 form has different effect on the stereocomplex biocomposite system. Compared to

Table 1. The summary of DSC data for s-PDLCL, s-PDLCL/TCP, and s-PDLCL/g-TCP

Materials	TCP [%]	T_g [°C]	T_m^1 [°C]	ΔH_m^1 [J/g]	T_m^2 [°C]	ΔH_m^2 [J/g]	Degree of stereocomplex [%]
s-PDLCL	0	44.86	149.70	5.358	205.53	40.67	88.36
s-PDLCL/TCP5	5	46.58	149.87	10.54	205.85	8.58	44.87
s-PDLCL/TCP10	10	51.27	155.09	15.23	201.61	8.53	35.90
s-PDLCL/TCP15	15	53.61	153.09	24.29	201.64	9.27	27.63
s-PDLCL/g-TCP5	5	45.86	150.27	1.519	202.57	16.73	91.68
s-PDLCL/g-TCP10	10	45.57	146.80	1.556	206.50	25.81	94.31
s-PDLCL/g-TCP15	15	46.37	145.41	1.759	206.59	25.09	93.34

[1]copolymer
[2]stereocomplex

s-PDLCL/TCP at 5% TCP content, the s-PDLCL/g-TCP composite has about ~3% higher stereocomplex degree than s-PDLCL. The different behavior is caused by the presence of grafted-PLLA on the activated TCP surfaces. The grafted PLLA on activated TCP surfaces improves the miscibility of PLLA-g-TCP with the stereocomplex matrix. PLLA-g-TCP96 exhibits better interfacial phase interaction in the stereocomplex biocomposite than pristine TCP [12]. The presence of grafted-PLLA on the activated TCP surfaces also supports the formation of stereocomplex with D-lactide fragment which results in increasing stereocomplex degree (~3%). The increasing TCP contents of s-PDLCL/g-TCP increase the stereocomplex degree up to a certain level, and then slightly decrease. In the s-PDLCL/g-TCP biocomposite system, it assumed that grafted-PLLA and TCP materials have opposite effects on stereocomplexation. The grafted-PLLA supports the miscibility and stereocomplex formation. Contrary, TCP materials tend to disrupt the L- and D-lactide fragments in the system. At the certain content (up to 10%) of PLLA-g-TCP96, the effect of grafted-PLLA seems to be superior to that of TCP. But, at higher TCP content (15%), the TCP effect starts to overcome the grafted-PLLA effect. That counter-effect causes the increasing of stereocomplex degree up to 10% of TCP content, then the decrease at higher TCP content (15%).

WAXD analysis was performed for the further investigation for the stereocomplex structure in the presence of calcium phosphate filler. The neat copolymers (PLLCL and PDLCL) show diffraction peaks at 2θ = 16.56, 18.74, and 21.74° (figure not shown) corresponding to the α-form of the copolymer. The stereocomplex biocomposites and s-PDLCL (control sample) exhibit appearance of new peaks at 2θ = 11.96, 20.82, and 23.88° which correspond to stereocomplex crystallites [14, 15]. The presence of PLLA-g-TCP96 increases stereocomplex degree of the s-PDLCL/g-TCP biocomposites up to a certain PLLA-g-TCP content (Figure 6a). It was shown by the increasing relative intensity of peaks characteristic of the stereocomplex as compared to that in the copolymer. The grafted-PLLA fragments on the activated TCP surface can interact with D-lactide fragments from copolymer PDLCL and form stereocomplex crystallites. PLLA-g-TCP96 can act as a heterogeneous nucleating agent and decreases the crystalization activation energy up to certain content. Above the optimum content, PLLA-g-TCP96 can act as blocking site which obstructs the formation of stereocomplex crystallites. In the other hand, the WAXD results for s-PDLCL/TCP (Figure 6b) show the decreasing relative intensity of stereocomplex relative to copolymer peaks which means decreasing stereocomplex degree by increasing TCP contents.

The distribution of inorganic TCP in the stereocomplex matrix is illustrated by SEM images in Figure 7. For s-PDLCL/TCP biocomposites (Figure 7a–7c), pristine TCP has limited dispersibility in the stereocomplex matrix. There are some TCP particle agglomerates even at 5% TCP content which caused by the limited interaction between inorganic TCP with polymer matrix. The grafted-PLLAs sup-

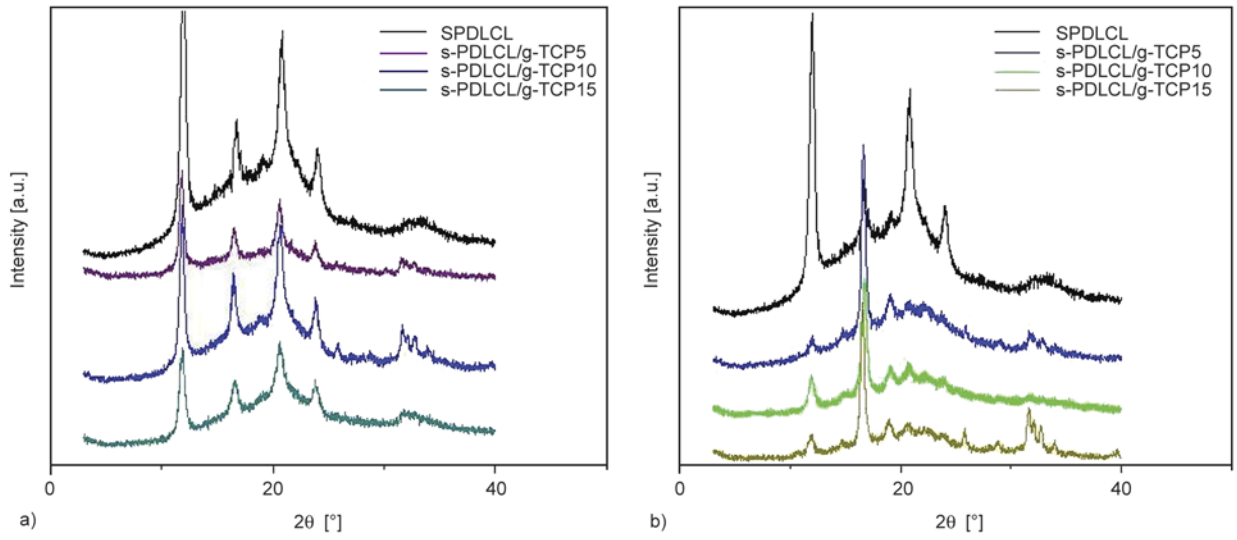

Figure 6. WAXD patterns of biocomposites: a) s-PDLCL/g-TCP; b) s-PDLCL/TCP

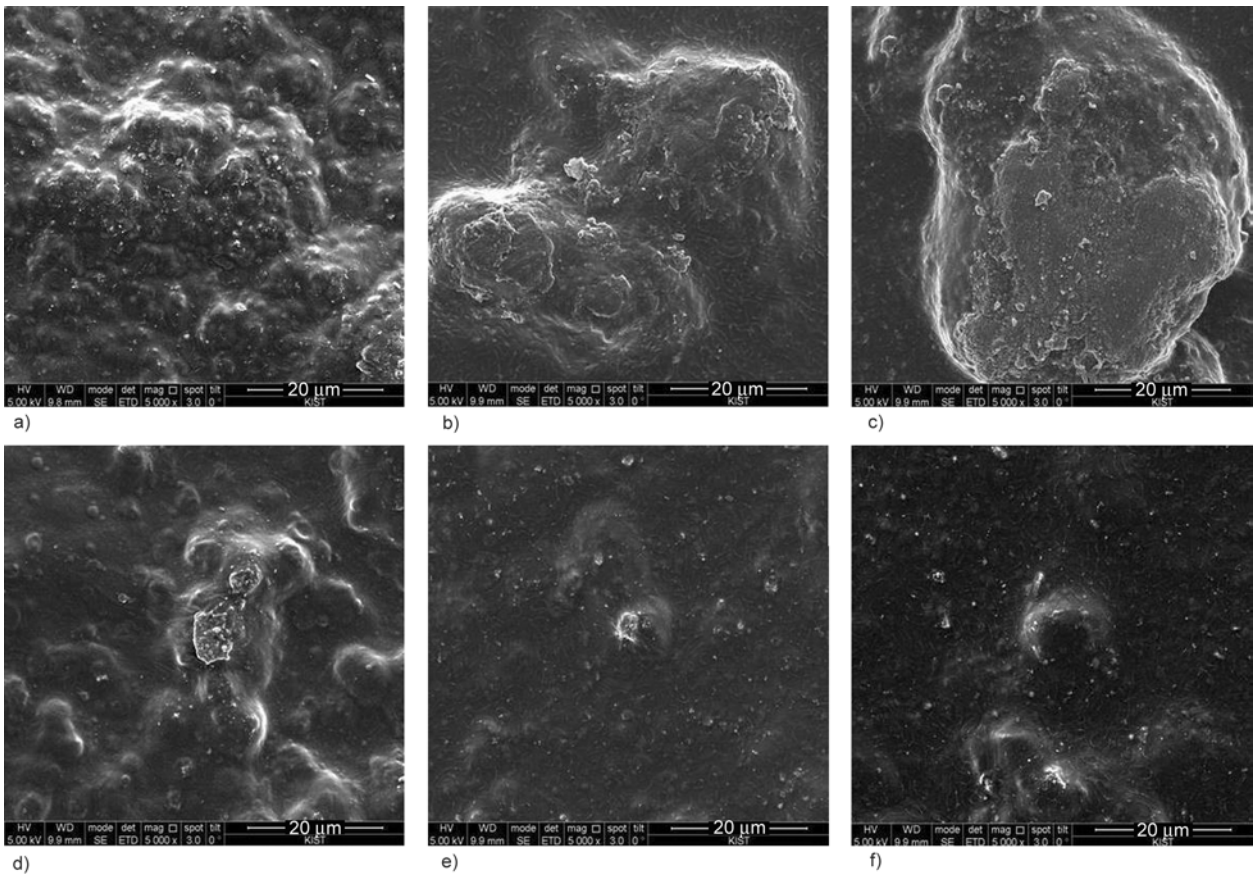

Figure 7. SEM images of s-PDLCL/TCP: a) 5%; b) 10%; c) 15% of TCP particles and s-PDLCL/g-TCP biocomposites: d) 5%; e) 10%; f) 15% of PLLA-g-TCP (scale bar = 20 µm)

port the dispersion of TCP in the stereocomplex matrix as shown in Figure 7d–7f. The grafted-PLLA has strong interaction with L-lactide fragments from PLLCL and also D-lactide fragments from PDLCL by forming stereocomplex. Those interactions result in homogeneous dispersion of PLLA-g-TCP in the stereocomplex biocomposite matrix.

The addition of inorganic materials to the polymeric matrix is practiced to improve its mechanical properties. The Young's modulus of s-PDLCL and biocomposites from s-PDLCL and inorganic TCP was depicted in Figure 8. The s-PDLCL/g-TCPs show higher Young's modulus compare to the s-PDLCL/TCP and neat s-PDLCL. The s-PDLCL/TCP shows slight improvement in Young's modulus even though the stereocomplex degree was decreased with increasing TCP content. It also has limitation in making homogeneous dispersion in stereocomplex matrix. The small improvement in Young's modulus was presumably supported by the stiffening effect of TCP materials [18]. Otherwise, s-PDLCL/g-TCPs show better improvement in Young's modulus. The Young's modulus was increased by increasing TCP content up to certain

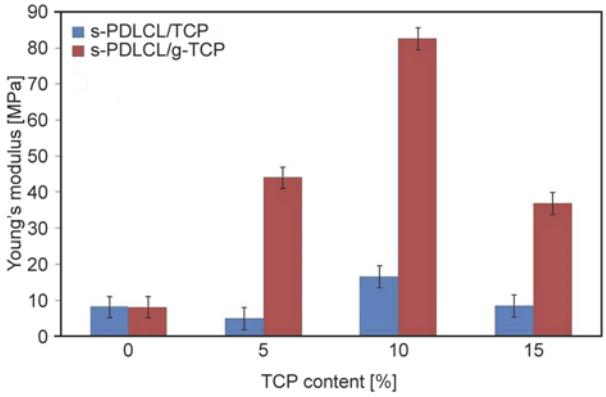

Figure 8. The mechanical property (Young's modulus) of s-PDLCL and its biocomposites (s-PDLCL/TCP and s-PDLCL/g-TCP)

content (10 %), then decreased at higher content (15%). The maximum Young's modulus was ~80 MPa at 10% of PLLA-g-TCP96 content. This mechanical improvement is in accordance with the result from DSC analysis and SEM images. The presence of grafted-PLLA from PLLA-g-TCP96 in the s-PDLCL/g-TCP results in a homogeneous dispersion of TCP in the stereocomplex matrix and also increases the stereocomplex degree. The decreasing Young's modulus at s-PDLCL/g-TCP15

was caused by the decrease of the stereocomplex degree and by the presence of TCP particle in high concentration (15%). There is a slight decrease in the stereocomplex degree of s-PDLCL/g-TCP. On the other hand, higher solid filler (PLLA-g-TCP) in the composite tends to form aggregate which decreases the interfacial filler-polymer matrix adhesion [19].

4. Conclusions

PLLA-g-TCP was successfully produced by ring-opening polymerization of L-lactide in the presence of surface-activated TCP. The attachment of PLLA was confirmed by IR spectroscopy, ToF-SIMS, and SEM images. Stereocomplex biocomposites were obtained by combining PDLCL and PLLCL in the presence of pristine TCP or PLLA-g-TCP96 through supercritical CO_2-methylene chloride system. The s-PDLCL/TCPs show decreasing in stereocomplex degree and inhomogeneous dispersion of TCP in stereocomplex matrix which results in a slight improvement of the mechanical properties. Contrary, the presence of PLLA-g-TCP96 in the s-PDLCL/g-TCP increases the stereocomplex degree up to certain content and also supports the homogeneous dispersion of TCP materials in stereocomplex matrix. These interactions support the improvement of mechanical properties of s-PDLCL/g-TCP. The optimum content of PLLA-g-TCP96 in s-PDLCL/g-TCP biocomposite is 10%. The combination of stereocomplex matrix and TCP materials provide a promising route to use such materials for internal fracture fixation devices.

Acknowledgements

This study was supported by the National Research Foundation of Korea Grant funded by the Korea Government (MEST), NRF-2010-C1AAA001-0028939.

References

[1] Törmälä P., Pohjonen T., Rokkanen P.: Bioabsorbable polymers: Materials technology and surgical applications. Proceedings of the Institution of Mechanical Engineers Part H: Journal of Engineering in Medicine, **212**, 101–111 (1998). DOI: 10.1243/0954411981533872

[2] De Jong S. J., van Dijk-Wolthuis W. N. E., Kettenes-van den Bosch J. J., Schuyl P. J. W., Hennink W. E.: Monodisperse enantiomeric lactic acid oligomers: Preparation, characterization, and stereocomplex formation. Macromolecules, **31**, 6397–6402 (1998). DOI: 10.1021/ma980553i

[3] Tsuji H.: Poly(lactide) stereocomplexes: Formation, structure, properties, degradation, and applications. Macromolecular Bioscience, **5**, 569–597 (2005). DOI: 10.1002/mabi.200500062

[4] Purnama P., Jung Y., Kim S. H.: Stereocomplexation of poly(L-lactide) and random copolymer poly(D-lactide-*co*-ε-caprolactone) to enhance melt stability. Macromolecules, **45**, 4012–4014 (2012). DOI: 10.1021/ma202814c

[5] Qiu X., Chen L., Hu J., Sun J., Hong Z., Liu A., Chen X., Jing X.: Surface-modified hydroxyapatite linked by L-lactic acid oligomer in the absence of catalyst. Journal of Polymer Science Part A: Polymer Chemistry, **43**, 5177–5185 (2005). DOI: 10.1002/pola.21006

[6] Miyai T., Ito A., Tamazawa G., Matsuno T., Sogo Y., Nakamura C., Yamazaki A., Satoh T.: Antibiotic-loaded poly-ε-caprolactone and porous β-tricalcium phosphate composite for treating osteomyelitis. Biomaterials, **29**, 350–358 (2008). DOI: 10.1016/j.biomaterials.2007.09.040

[7] Li X., Shi J., Dong X., Zhang L., Zeng H.: A mesoporous bioactive glass/polycaprolactone composite scaffold and its bioactivity behavior. Journal of Biomedical Materials Research Part A, **84**, 84–91 (2008). DOI: 10.1002/jbm.a.31371

[8] Oréfice R., Clark A., West J., Brennan A., Hench L.: Processing, properties, and *in vitro* bioactivity of polysulfone-bioactive glass composites. Journal of Biomedical Materials Research Part A, **80**, 565–580 (2007). DOI: 10.1002/jbm.a.30948

[9] Huan Z., Chang J.: Self-setting properties and *in vitro* bioactivity of calcium sulfate hemihydrate–tricalcium silicate composite bone cements. Acta Biomaterialia, **3**, 952–960 (2007). DOI: 10.1016/j.actbio.2007.05.003

[10] Low K. L., Tan S. H., Zein S. H. S., Roether J. A., Mouriño V., Boccaccini A. R.: Calcium phosphate-based composites as injectable bone substitute materials. Journal of Biomedical Materials Research Part B: Applied Biomaterials, **94**, 273–286 (2010). DOI: 10.1002/jbm.b.31619

[11] Hak D. J.: The use of osteoconductive bone graft substitutes in orthopaedic trauma. Journal of the American Academy of Orthopaedic Surgeons, **15**, 525–536 (2007).

[12] Choudhery R. A., Vance C. J.: The characterisation and properties of modern conversion coatings for use with paint films. in 'Advances in corrosion protection by organic coatings. Cambridge, England' 64 (1989).

[13] Kunze C., Freiter T., Helwig E., Sandner B., Reif D., Wutzler A., Radusch H-J.: Surface modification of tricalcium phosphate for improvement of the interfacial compatibility with biodegradable polymers. Biomaterials, **24**, 967–974 (2003).
DOI: 10.1016/s0142-9612(02)00433-7

[14] Hong Z., Qiu X., Sun J., Deng M., Chen X., Jing X.: Grafting polymerization of L-lactide on the surface of hydroxyapatite nano-crystals. Polymer, **45**, 6699–6706 (2004).
DOI: 10.1016/j.polymer.2004.07.036

[15] Eriksson C., Bömer K., Nygren H., Ohlson K., Bexell U., Billerdahl N., Johansson M.: Studies by imaging TOF-SIMS of bone mineralization on porous titanium implants after 1 week in bone. Applied Surface Science, **252**, 6757–6760 (2006).
DOI: 10.1016/j.apsusc.2006.02.194

[16] Purnama P., Kim S. H.: Stereocomplex formation of high-molecular-weight polylactide using supercritical fluid. Macromolecules, **43**, 1137–1142 (2010).
DOI: 10.1021/ma902536p

[17] Purnama P., Lim S. H., Jung Y., Kim S. H.: Stereocomplex-nanocomposite formation of polylactide/fluorinated-clay with superior thermal property using supercritical fluid. Macromolecular Research, **60**, 545–548 (2012).
DOI: 10.1007/s13233-012-0092-4

[18] Wilberforce S. I. J., Finlayson C. E., Best S. M., Cameron R. E.: A comparative study of the thermal and dynamic mechanical behaviour of quenched and annealed bioresorbable poly-L-lactide/α-tricalcium phosphate nanocomposites. Acta Biomaterialia, **7**, 2176–2184 (2011).
DOI: 10.1016/j.actbio.2011.02.006

[19] López Manchado M. A., Valentini L., Biagiotti J., Kenny J. M.: Thermal and mechanical properties of single-walled carbon nanotubes–polypropylene composites prepared by melt processing. Carbon, **43**, 1499–1505 (2005).
DOI: 10.1016/j.carbon.2005.01.031

[20] Odian G.: Principles of polymerization. Wiley, New York (1991).

eXPRESS Polymer Letters Vol.7, No.12 (2013) 984–995
Available online at www.expresspolymlett.com
DOI: 10.3144/expresspolymlett.2013.97

Active diluents effects of 4-nonylphenoxy-1, 2-dinitrilbenzene on phthalonitrile containing benzoxazine and their copolymerization behaviors

*M. Z. Xu, M. D. Liu, S. H. Dong, G. Y. Qiu, X. B. Liu**

Research Branch of Functional Materials, Institute of Microelectronic & Solid State Electronic, High-Temperature Resistant Polymers and Composites Key Laboratory of Sichuan Province, University of Electronic Science and Technology of China, Chengdu 610054, P. R. China

Received 13 June 2013; accepted in revised form 17 August 2013

Abstract. 4-nonylphenoxy-1, 2-dinitrilbenzene (NP-ph), a novel kind of phthalonitrile containing flexible hydrocarbyl chains, has been synthesized. The structures of NP-ph were investigated by Nuclear Magnetic Resonance Spectroscopy (^{1}H-NMR) and Fourier Transform Infrared Spectroscopy (FTIR). Low viscosity NP-ph/phthalonitrile containing benzoxazine (BA-ph) blends were achieved by melt blending BA-ph with various content of NP-ph. Copolymerization behaviors and processability of NP-ph/BA-ph have been investigated by Differential Scanning Calorimetry (DSC) and Dynamic Rheological Analysis. Results indicated that NP-ph/BA-ph blends processability was improved and can be controlled by varying NP-ph contents, processing temperature and time. NP-ph/BA-ph polymers were prepared from the thermal polymerization with short curing time and low curing temperatures without addition of any other curing agents, which displayed high glass transition temperature (>360°C) and attractive thermal decomposition temperature (>420°C). The outstanding glass transition temperature and desirable thermo-oxidative stabilities, together with good processability and sound process conditions could enable the NP-ph/BA-ph polymers to be further explored in the fields under some practical critical circumstances with requirements of high wears and temperatures.

Keywords: *thermal properties, active diluents effects, phthalonitrile, copolymer behavior, thermal mechanical properties*

1. Introduction

Resin-transfer molding (RTM) for the fabrication of composite materials has been receiving more and more attention because of its comparatively low cost and high efficiency [1, 2]. Environmentally friendly processes together with the satisfactory products resulted in a wide application of RTM in several commercial applications, from repairing bridges to making sailboats and refrigerated cargo boxes, and has been considered for various civil and marine infrastructure, aerospace, defense and automotive applications [3–5].

Owing to the strict requirements of the process, most of thermosetting resins cannot satisfy the requirements of RTM [6]. Though the unsaturated polyesters, vinyl esters, and acrylates can match the characteristic of low viscosity (<1 Pa·s) and a long pot life at the injection temperature, none of these resins can meet the need of high-performance composites for strength, modulus, and thermo-oxidative stability.

Recently, phthalonitrile resin containing benzoxazine (BA-ph) was designed and synthesized via a condensation reaction between amino-functional phthalonitrile and bisphenol A [7]. Owing to the

*Corresponding author, e-mail: liuxb@uestc.edu.cn

active phenolic hydroxyls generated from ring-opening of benzoxazine, many advantages can be obtained. On the one hand, the active phenolic hydroxyls generated from ring-opening of benzoxazine can be used as a kind of curing agent to achieve the cross-linking networks, thus realizing the self-promoted copolymerization. On the other hand, the active phenolic hydroxyls allowed BA-ph to be used as hydroxyl-functional phthalonitrile to achieve good processability and desirable properties of the composites [8–11]. Therefore, these merits accompany their excellent processability (low melting point, low viscosity), outstanding thermal stabilities and cost-effectiveness have made BA-ph resin attract increasing interests in the field of composites compared with the traditional heat resisting resins and can find their potential applications in the future [12–15].

Though the BA-ph resin showed quite low melt viscosity, the resin was still required to be further improved to reduce the melt viscosity to match the requirements of industrial applications. Thus, in our previous work, low-viscosity epoxy resin has been partially incorporated into the BA-ph resin to improve the prosessability [8]. It has been reported that the incorporation of low-viscosity epoxy resin has significantly decreased the melt viscosity and improved the impregnation characteristic of the composites [16–19]. Moreover, the low-viscosity resin also allowed addition of a greater amount of filler (e. g. nanoclay and CNTs) while maintaining processability of the molding compound [11, 20, 21]. However, in the case, the decrease of melt viscosity of the composites was at the cost of heat resistance and reaction rate [8, 20, 21].

Recently, a novel kind of low-viscosity phthalonitrile containing a flexible aliphatic hydrocarbon segment (4-nonylphenoxy-1,2-dinitrilbenzene, NP-ph) has been designed and manufactured. The long aliphatic hydrocarbon segment in the NP-ph monomer resulted in the low melt temperature and viscosity. Meanwhile, the active cyano groups can be involved in the polymerization reaction of the BA-ph, resulting to the high cross-linking degree and heat resistance. In this work, NP-ph/BA-ph blends and polymers were prepared. Copolymerization behaviors and processability of NP-ph/BA-ph were investigated and discussed. In addition, the effect of various contents of active diluent NP-ph on the polymerization rate and degree of the NP-ph/BA-ph systems has also been monitored by Differential scanning calorimetry (DSC) and dynamic rheological analysis. Moreover, the thermal mechanical properties and thermal stabilities of NP-ph/BA-ph polymers were also investigated and discussed.

2. Experimental

2.1. Materials

P-nonylphenoxy (p-NP) (99%), N, N-dimethylformamide (DMF) (99%), potash (K_2CO_3) (99%), 4-nitrophthhalonitrile (Nph) (99%), were purchased from Kelong Reagent Co. Ltd., Chengdu, China. All the chemicals and reagents were used without further purification. Phthalonitrile containing benzoxazine (BA-ph) was synthesized and purified according to the procedure reported before [7].

2.2. Preparation of the NP-ph monomer

33 g of p-nonylphenoxy and 60 mL DMF were added to a 250 mL three necks round bottle flask equipped with a mechanical stirrer and refluxing condenser, the mixtures were heated at 60°C for few minutes to be dissolved sufficiently, then the K_2CO_3 was added to the solution and the temperature was kept at 60°C with vigorous stirring for 5 h. After that, 4-nitrophthalonitrile (Nph) was added to the light pink mixtures and continued stirring for another 3 h. Finally, an orange solution was obtained. Then the solution was poured into water to precipitate the NP-ph monomer with vigorously stirring, the products were separated and washed several times by distilled water and then dried at 100°C overnight.

2.3. Preparation of NP-ph/BA-ph blends

The NP-ph/BA-ph thermosetting copolymers with different ratios (NP-ph content: 10, 20, 30, and 40 wt%) were prepared by melt blending at 140°C for 20 min.

2.4. Preparation of the NP-ph/BA-ph polymers

Firstly, polytetrafluoroethylene mold with cavity dimensions 50 mm × 10 mm × 3 mm was preheated at 160°C for 2 h. Then, the NP-ph/BA-ph blend was molten at 140°C for 20 min and the viscous melt was poured into the preheated polytetrafluoroethylene mold to undergo the curing procedures. In accordance with the results of DSC, the onset temperature of the curing reaction was 200°C and the double peaks of exothermic reaction were about

240 and 280°C. As well known, explosive curing reaction would lead to large numbers of internal defects. Combination of the results of dynamic rheological analysis, $T = 180$°C was chosen as a moderate onset temperature of polymerization. 160°C was selected to make sure that the blend could be molten well and it was enough to eliminate the air bubbles in the viscous melt resin. In sum, the curing procedure was selected as follows: 160°C (4 h), 180°C (4 h), 200°C (4 h), 240°C (2 h), 280°C (2 h). The cured NP-ph/BA-ph polymers were sanded to a thickness of 2 mm for the Dynamic mechanical measurements (DMA). Also, the cured NP-ph/BA-ph polymers were physically pulverized under ambient conditions for thermal gravimetric analysis (TGA).

2.5. Characterizations

Nuclear magnetic resonance (^{1}H-NMR) spectra were taken on a AV400 nuclear magnetic resonance spectrometer with a proton frequency of 300 MHz and the solvent was $CDCl_3$, Bruker, Germany. Fourier Transform Infrared (FTIR) spectra were recorded with FTIR8400S Fourier Transform Infrared spectrometer in KBr pellets between 4000 and 500 cm^{-1} in air, Shimadzu, Japan. Differential scanning calorimetric (DSC) analysis was performed by Modulated DSC-Q100 at a heating rate of 10°C/min and a nitrogen flow rate of 50 mL/min, TA Instruments, USA. The DSC testing of NP-ph and BA-ph monomer was performed by heating the samples from 50 to 350°C, while, the NP-ph/BA-ph blending was heater from 100 to 350°C. Viscosity studies and curing process of the blends were conducted using Rheometer AR-G2 with a heating rate of 5°C/min and a frequency of 1 Hz from 50 to 300°C in air, TA Instruments, USA. The samples (0.5–1 g) were melted between 25 mm diameter parallel plates with the gap of 1000 μm and shear rate of 1 Hz. The isothermal tests of dynamic rheological analysis were performed at 160, 180 and 200°C, respectively, with a frequency of 1 Hz and shear rate of 1 Hz. Dynamic mechanical analysis (DMA) in a three-point-blending mode was performed on QDMA-800 dynamic mechanical analyzer to determine the glass transition temperature (T_g), TA Instruments, USA. The storage modulus and tan delta were investigated at a frequency of 1 Hz and amplitude of 20 μm, and the samples (dimensions 30 mm × 10 mm × 2 mm) were heated from 50 to 400°C at a temperature ramp of 3°C/min. Thermogravimetry (TGA) and Differential presentation of integral TGA (DTA) was performed on a TGA Q50 with a heating rate of 20°C/min (under nitrogen or air) and a purge of 40 mL/min from 100 to 800°C, TA Instruments, USA.

3. Results and discussion

3.1. Synthesis and characterization of NP-ph monomer

The NP-ph monomer has been synthesized via substitution reaction of 4-nitrophthalonitrile and p-nonylphenoxy at the presence of K_2CO_3 in the N, N-dimethylformamide (DMF) solvent (Figure 1). The assumed reaction sequence is depicted in Figure 2. The monomer structures were characterized by ^{1}H-NMR and FTIR spectroscopies. The relevant data are listed as follows.

^{1}H-NMR (300 MHz, $CDCl_3$-d6, δ ppm): 0.96 (t, 3H, CH3), 1.29–1.62 (m, 14H, –CH2–), 2.55 (t, 2H, Ar–CH2), 7.08 (t, 2H, Ar–H), 6.87 (d, 2H, Ar–H), 7.35 (s, 1H, Ar–H), 7.38 (d, 1H, Ar–H), 7.65 (d, 1H, Ar–H).

FTIR (liquid state, cm^{-1}): 3250 to 2750 cm^{-1} (–C–H stretching vibrations of the alkyl), 2230 cm^{-1} (–CN), 1230 cm^{-1} (stretch, Ar–O–Ar), 1490 cm^{-1} (1, 2 and 4 substitution of benzene ring).

^{1}H-NMR spectrum was shown in Figure 3 and FTIR spectrum was depicted in Figure 4. In ^{1}H-NMR spectrum, the prominent resonances at 0.866–2.66 ppm in the aliphatic frequency corresponded to the hydrogen in the long hydrocarbyl segment. The prominent resonances at 6.76–7.71 ppm were consistent with the hydrogens in the benzene ring. The data were found to be in good agreement with the proposed structures.

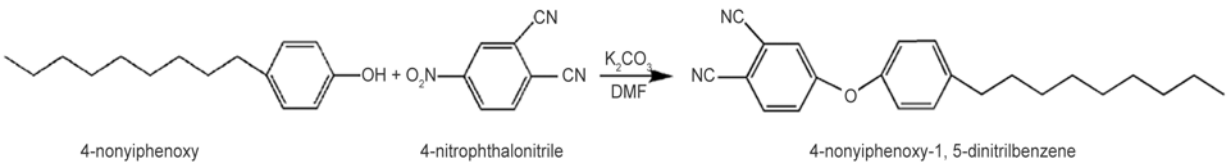

Figure 1. Synthesis of the NP-ph monomer

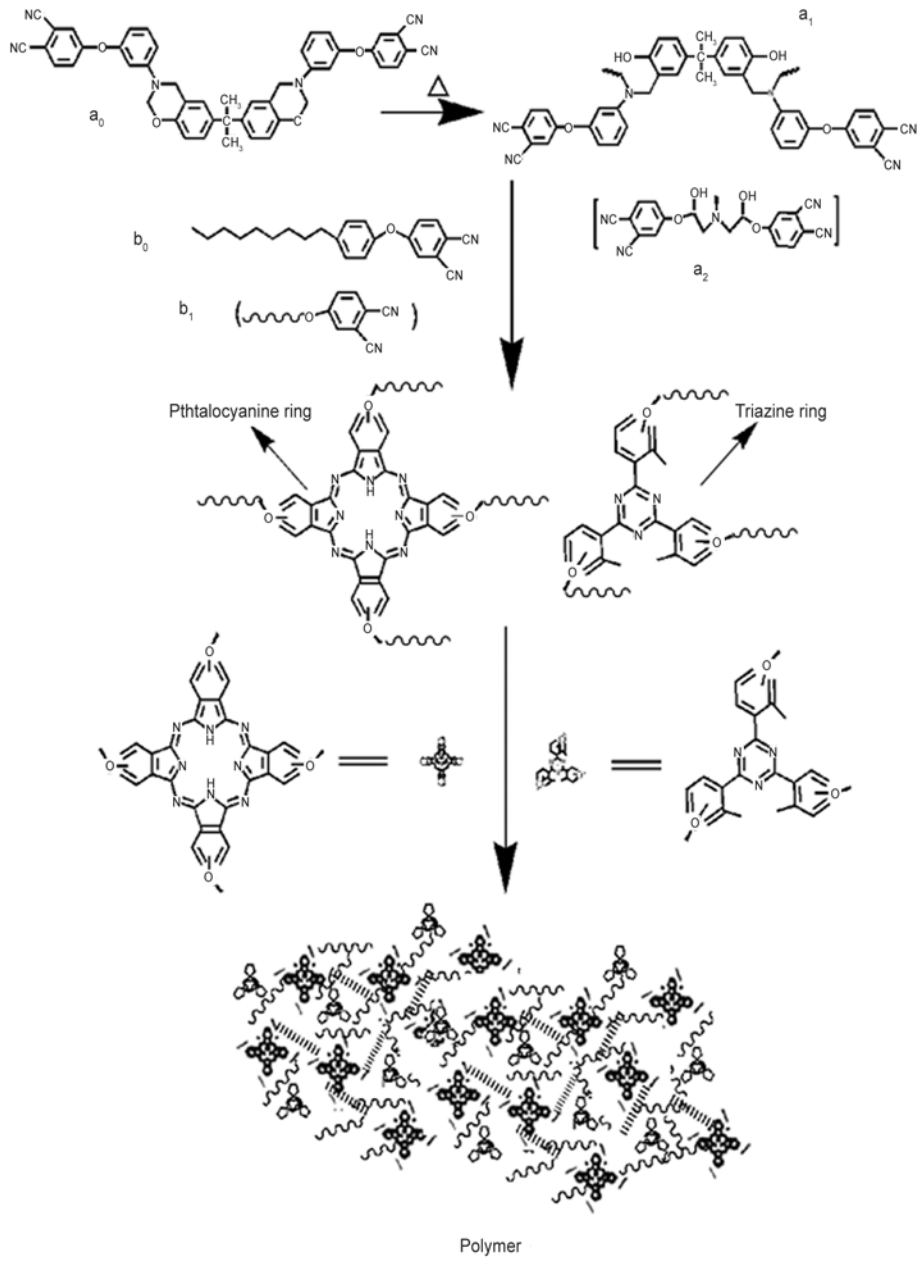

Figure 2. Preparation of NP-ph/BA-ph copolymers: a_0) BA-ph monomer, a_1) BA-ph monomer with ring-opening of oxazine, a_2) simplification of a_1, b_0) NP-ph monomer, b_1) simplification of b_0

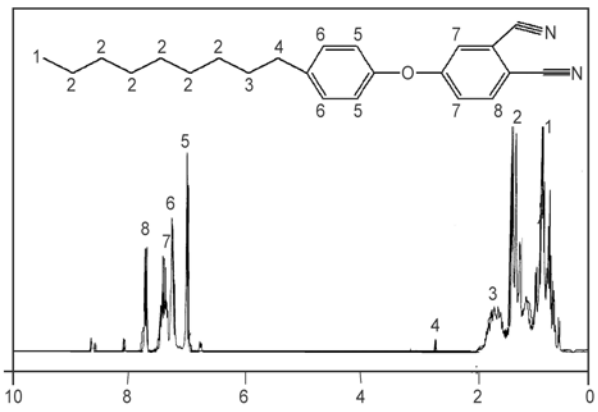

Figure 3. The ^{1}H-NMR spectrum of NP-ph in $CDCl_3$

The FTIR spectrum for NP-ph monomer was discussed in the range from 4000 to 500 cm^{-1}, as shown in Figure 4. The absorption peaks at round 1230 cm^{-1} represented the antisymmetry stretching vibrations of diphenyl ether indicated the interaction between p-nonylphenoxy and 4-nitrophthhalonitrile. The intensive absorption peak at 2230 cm^{-1} was assigned to the stretching vibrations of cyano groups (–CN) [22]. The absorption band of the C–H stretching vibration of saturated hydrocarbon was observed in the range of 2750 and 3000 cm^{-1}. While, the absorption band of aromatic hydrocarbon was observed above 3000 cm^{-1} as the shoulder of the band in the

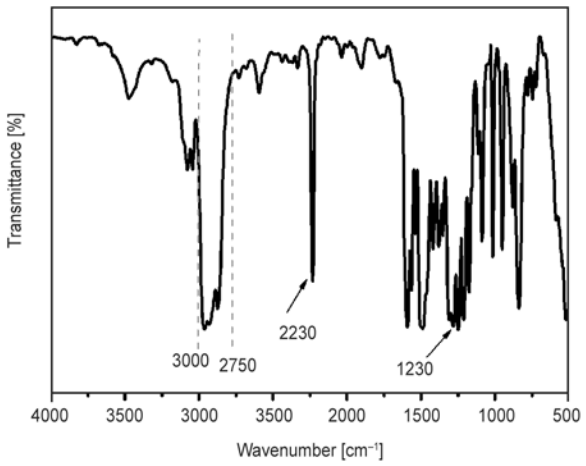

Figure 4. The FTIR spectrum of NP-ph

range from 2750 to 3000 cm^{-1} corresponding to the saturated hydrocarbon. The characteristic absorption bands in Figure 4 demonstrated that the phthalonitrile containing flexible chains have been obtained.

3.2. Self-promoted curing behaviors on NP-ph/BA-ph copolymers

Figure 5 showed the DSC thermograms in the temperature range from 50 to 350°C at the heating rate of 10°C/min of BA-ph and NP-ph resins, respectively. The curve showed the curing exotherm of the BA-ph monomer exhibited two characteristic exothermic peaks: a peak maximum of about 220°C and the other about 260°C, which was characteristic of the thermal curability of the resin [7, 8]. On the contrary, the NP-ph resin showed no sign of a curing reaction in this temperature range without added initiators or catalysts. As was well known, the polymerization of the neat phthalonitrile monomers was extremely sluggish and this procedure needed several days to obtain stable polymers [7, 23, 24]. Thus, in the case of the NP-ph resin, no self-promoted polymerization has occurred in this temperature range. Meanwhile, an endothermic peak at about 300°C has been observed which may be as a result of evaporation of the monomer.

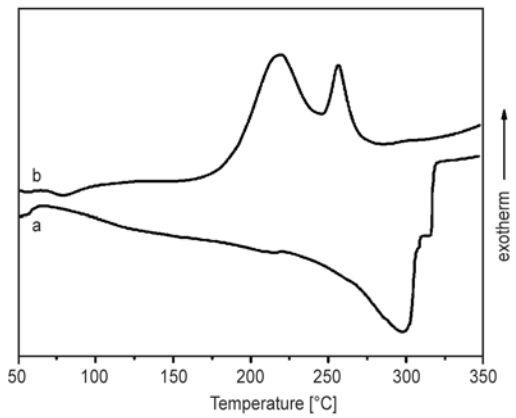

Figure 5. The DSC curves of (a) BA-ph monomer and (b) NP-ph monomer

Table 1. Thermal properties and gelation time at 180° of NP-ph/BA-ph blends

Samples	T_{top1} [°C]	ΔH_{curing} [J·g^{-1}]	T_{top2} [°C]	ΔH_{curing} [J·g^{-1}]	Gelation time at 180°C [min]
10%	225.9	131.0	262.7	53.6	23
20%	231.5	106.4	266.1	79.5	29
30%	235.7	75.6	270.0	77.8	37
40%	240.5	102.5	273.3	63.2	48

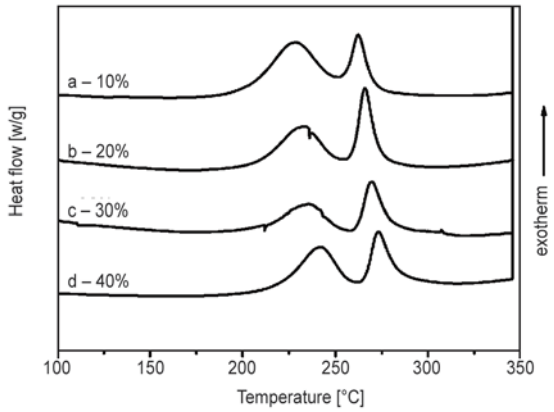

Figure 6. The DSC curves of NP-ph/BA-ph blends with various content of NP-ph (a) 10%, (b) 20%, (c) 30% and (d) 40%

The self-promoted curing behaviors of the NP-ph/BA-ph blends were studied by DSC (Figure 6) and the main results were listed in Table 1. In the curves shown in Figure 6, the retardation of the polymerization reaction of BA-ph resin has been observed as a weak shift of the exothermic peaks to higher temperature. The degree of the retardation increases with increasing amounts of NP-ph resin. This was because the NP-ph component in the system acted as a diluent, resulting in the retardation of the polymerization of BA-ph resin. The curing reaction would occur preferentially at around 220°C and the oxazine ring-opening polymerization produced Mannich bridge ($–CH_2–NR–CH_2–$) with phenolic hydroxyl functional groups (Figure 2). The polymerization among BA-ph monomers was predominant in the temperature range from 210–240°C [9, 10]. Then the free phenolic hydroxyls with active hydrogen generated from the ring-opening reaction of BA-ph at elevated temperatures (265°C) may promote the

polymerization of cyano groups of BA-ph and NP-ph. That was, at proper temperature (210–240°C), ring-opening of benzaoxazine rings took place and a certain amount of active hydroxyls was generated. On the one hand, the oxazine ring-opening polymerization occurred to produce Mannich bridge structures. On the other hand, in the presence of active hydrogen, cyano groups were catalyzed to become isoindole rings intermediates, and then immediately transited to phtahalocyanine and triazine rings with excess cyano groups. Continuously, the triazine and phthalocyanine rings formed between BA-ph and NP-ph resin. Large amounts of rigid groups would be entrapped into and twined by the flexible chains in the polymer matrices (Figure 2) [8, 25, 26].

3.3. Structures of NP-ph/BA-ph blends and polymers

The structures of NP-ph/BA-ph blends and polymers with 20 and 40 wt% NP-ph have been confirmed by FTIR spectra shown in Figure 7 and Figure 8. Figure 7 (a) and (b) curves showed the structure of the NP-ph/BA-ph blends with 20 and 40% NP-ph, respectively. It can be seen that the absorption band at around 956 cm^{-1} contributed to the trisubstituted benzene ring attached with oxazine ring, confirmed the existence of oxazine rings. The intense characteristic absorption band of cyano groups at 2230 cm^{-1} indicated that the polymerization of cyano groups hardly proceeded or did not occur at all. Meanwhile, the absorption band at 1493 cm^{-1}, corresponding to the in-plane carbon-carbon stretching of the trisubstituted benzene ring, evidently indicated that the polymerization of the NP-ph/BA-ph blend

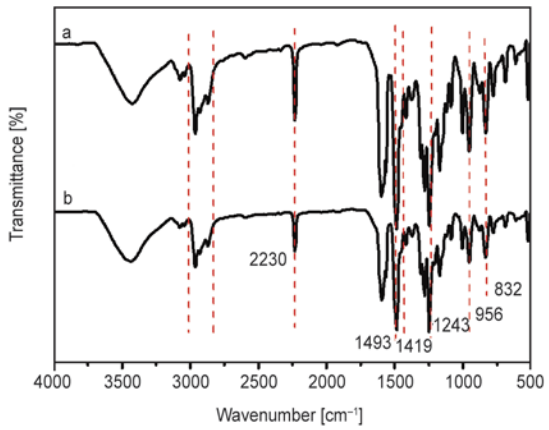

Figure 7. The FTIR spectra of NP-ph/BA-ph blends with various content of NP-ph (a) 20% and (b) 40%

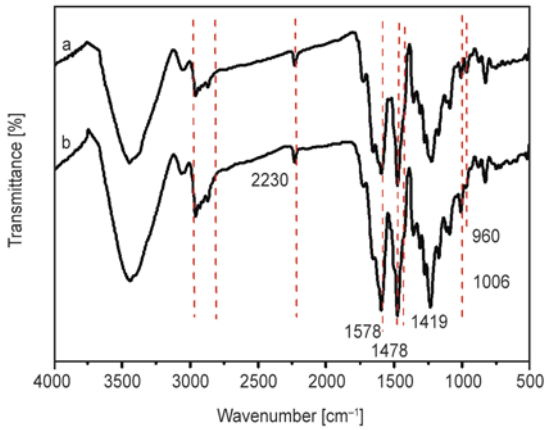

Figure 8. The FTIR spectra of NP-ph/BA-ph polymers with various content of NP-ph (a) 20% and (b) 40%

did not occur during melt blending. Additionally, the characteristic absorption bands of NP-ph were observed in the NP-ph/BA-ph blend in Figure 7.

In comparison with the characteristic absorption bands shown in Figure 7, the intensity of the characteristic bands of benzoxazine at ~956 cm^{-1} shown in Figure 8 reduced significantly, indicating that the benzoxazine has been involved to a great extent in the polymerization. The characteristic absorption band at 2230 cm^{-1} significantly decreased, new absorption bands at 1006 and 1578 cm^{-1} were observed which indicated the formation of phthalocyanine and triazine rings among cyano groups [7, 22]. The band at 1493 cm^{-1} has been shifted to 1478 cm^{-1}, which corresponds the in-plane carbon-carbon stretching of the tetrasubstituted benzene ring, indicating that the methylene bridges formed in the free ortho positions of the phenolic structures [25, 26]. In comparison with that shown in Figure 7, the formation of methylene bridges, phthalocyanine rings and triazine rings demonstrated that the copolymerization of NP-ph and BA-ph has occurred to a great extent.

3.4. Processability of NP-ph/BA-ph blends

The complex viscosity (η*) of NP-ph/BA-ph blends as a function of temperature from 50 to 300°C were shown in Figure 9. It can be seen that the η* of NP-ph/BA-ph copolymers diminished gradually before 130°C. The minimum of the η* was about 0.75 Pa·s at 150°C for the blend with 20% NP-ph. At around 160°C, there was a slight increase of η* and a rapid increase of η* was observed at 180–210°C for all of the NP-ph/BA-ph blends. Moreover, the sharp increase of η* was observed at higher temperatures with increasing the amount of NP-ph resin in the

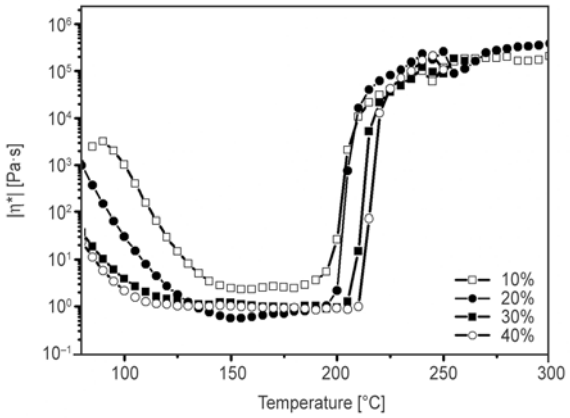

Figure 9. Complex viscosity curve as a function of temperature for NP-ph/BA-ph blends

blends. For the blend with 40% NP-ph, a rapid increase of η* was observed at 210°C, indicating that the polymerization was delayed with increasing the amount of NP-ph, in good agreement with DSC results in Figure 4.

To further determine the processing temperature and time for NP-ph/BA-ph copolymers, the η* change of the NP-ph/BA-ph copolymer with 20% NP-ph was measured as a function of time at various temperatures, shown in Figure 10. It can be seen that the η* at different temperatures were relatively low and stable before the proper curing reaction started. However, after the curing reaction started, the η* increased dramatically. Nevertheless, the time for dramatic η* increase was varied with the different temperatures. Namely, the η* increase of NP-ph/BA-ph copolymer at 160°C took a very long time (100 min), indicating that the reaction was carried out slowly. Quite the opposite, the η* increase of NP-ph/BA-ph copolymers at 200°C took a rather short time, revealing that curing reaction was carried out very fast. Thus, 180°C was a proper processing temperature for NP-ph/BA-ph copolymers. On the one hand, these results manifested that the η* of the NP-ph/BA-ph copolymer processed faster with increasing the processing temperature. On the other hand, these results revealed that processing temperature could accelerate the copolymerization reaction of NP-ph/BA-ph. From Figure 10, the processing time and polymerization rate of NP-ph/BA-ph system could be easily controlled by varying the processing temperature and the optical processing temperature for NP-ph/BA-ph copolymers was about 180°C.

Thus, 180°C was chosen to investigate the effect of NP-ph content on the processability of NP-ph/BA-ph copolymers, as shown in Figure 11. It can be seen that all of the NP-ph/BA-ph copolymers exhibited relatively low initial η* and the initial η* of NP-ph/BA-ph copolymers decreased with increasing the content of NP-ph. Generally, the low initial η* can offer convenience for processing such as fully mixing and removal of air bubbles, which was beneficial to practical operations and the final properties of products used in the field of RTM. Figure 11 also showed that with more NP-ph content, the time for cure reaction of NP-ph/BA-ph copolymers increased significantly, indicating that the NP-ph would retard the polymerization reaction rate of BA-ph. This may be due to that the sluggish NP-ph resin affected the generation, activity or redistribution of active hydroxyl generated from the ring-opening of benzoxazine rings, resulting in delaying the polymerization of cyano groups in the system. From these results, it was clear that NP-ph/BA-ph copolymer at processing temperature of 180°C exhibited good processing advantages due to the low initial η* and appro-

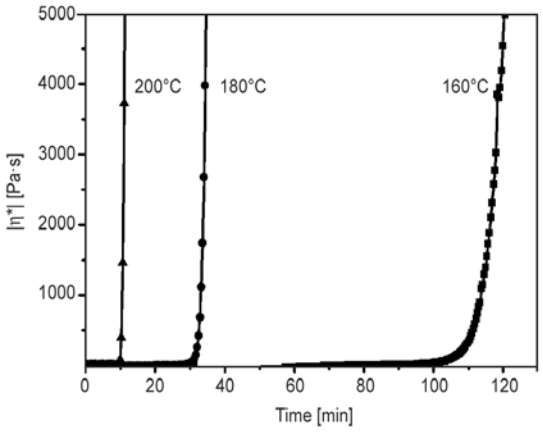

Figure 10. Complex viscosity as a function of time for the 20% NP-ph/BA-ph blends at various temperatures

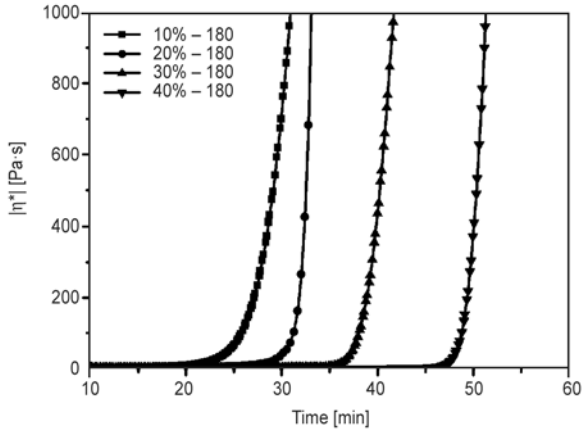

Figure 11. Complex viscosity as a function of time at 180°C for various NP-ph/BA-ph blends

priate processing temperature, while the processability of NP-ph/BA-ph copolymers could be varied by the amount of NP-ph. Additionally, based on the principle of classical rheological theory, the gelation time was determined from the crossover point of the storage modulus (G') and the loss modulus (G''). The time of gel-point was collected in Table 1 which was distinguished from that of BA-ph [8]. The proper processing time resulting from the presence of NP-ph was in favor for industrial applications.

3.5. Dynamic mechanical properties of NP-ph/BA-ph polymers

In the previous parts, copolymerizing behaviors and processability of NP-ph/BA-ph copolymers were investigated. These investigations can provide us effective molding procedures to prepare NP-ph/BA-ph polymers. Dynamic mechanical studies were conducted to evaluate the changes in the sample modulus as a function of temperature and determinate the T_g of the polymers. From these studies, storage modulus and tan delta plots generated on NP-ph/BA-ph polymers versus temperature were presented in Figure 12 and 13, respectively, and the results of T_g were exhibited in Table 2. In Figure 12, the modulus for NP-ph/BA-ph with 20% NP-ph changed from 3650 to 10 MPa when heated from 50 to 400°C. For all of the samples, large modulus changes were observed after 300°C. The data showed that the extent of the modulus changes decreased as the NP-ph content increased. However, the decrease for sample with 10% NP-ph may be the result of the pinholes in the sample pieces. The decrease in the storage modulus was attributed to the stress relaxation of NP-ph/BA-ph copolymers.

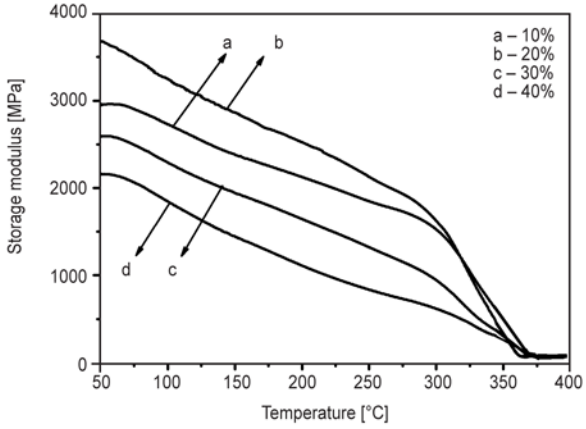

Figure 12. Storage modulus (G') as a function of temperature for various NP-ph/BA-ph polymers heated in nitrogen

Table 2. Glass transition temperatures and thermal and thermo-oxidative stabilities of NP-ph/BA-ph polymers

Samples	Nitrogen				Air		
	T_g [°C]	$T_{5\%}$ [°C]	$T_{10\%}$ [°C]	Yield char	$T_{5\%}$ [°C]	$T_{10\%}$ [°C]	Yield char
10%	371	437	483	72.7%	438	477	27.2%
20%	368	425	478	71.3%	435	473	12.4%
30%	366	422	469	69.8%	426	473	4.0%
40%	365	416	448	64.3%	414	465	3.0%

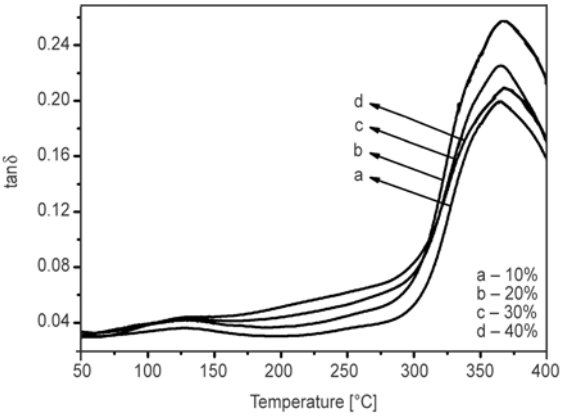

Figure 13. Damping factor (tanδ) as a function of temperature for various NP-ph/BA-ph polymers heated in nitrogen

Thus, the Tg was obtained from the maximum of tanδ in a plot of tan delta versus temperature. As noted in Figure 13, one or two relaxation peaks were observed in each plot. The tanδ peaks (100–150°C) of all the NP-ph/BA-ph polymers were attributed to NP-ph. On heating to 400°C, the tanδ peaks of all the NP-ph/BA-ph polymers occurred at above 360°C. Meanwhile, it can be seen that the tan delta peak shifted to lower temperatures as the NP-ph content increased. As was well known, the T_g of polymers depended on the rigidity of the molecular chains and the crosslinking degree [27–32]. It can be seen in Table 2 that the T_g of the samples were up to 360°C, which were obviously superior to the traditional epoxy, phenolics and polybenzoxazines resin [28, 30–32]. The outstanding T_g was mainly attributed to the high crosslinking degree of ring-opening polymerization of benzoxazine and heterocyclization of cyano groups in the NP-ph/BA-ph system. The polymerization of the active groups significantly increased the crosslinking degree and rigidity of the polymer, which greatly limited the motion of the molecular chains. With increasing the

content of NP-ph, the amount of flexible alkyl chins increased and then decreased the rigidity of the polymer to some extent, eventually resulting to the reduction of T_g.

3.6. Thermal stabilities of NP-ph/BA-ph polymers

The thermal decomposition of the NP-ph/BA-ph polymers was also examined by TGA (Figure 14) both in inert (nitrogen) and air (20% oxygen) environments at a heating rate of 20°C/min and the main results were summarized in Table 2, in which the temperatures at weight loss of 5% ($T_{5\%}$), 10% ($T_{10\%}$) and char yield at 800°C were displayed. For comparison, the thermal properties of BA-ph polymer have been provided in Table 2. Overall, all of the polymers exhibit a slow degradation in nitrogen environment beginning at about 420°C and extending to 800°C. This slow degradation rate may be attributed to the high concentration of phthalocyanine rings and triazine rings in the network, which may protect against degradation even at these high temperatures. The $T_{5\%}$ weight losses of the cured NP-ph/BA-ph polymers in nitrogen atmosphere were in the range of 416–437°C, and char yields at 800°C were in the range of 64–72%. The results indicated that the thermal stabilities of NP-ph/BA-ph polymers in N_2 atmosphere were weakly decreased by the increase of NP-ph content, which could be attributed to the relatively low thermal stabilities of NP-ph itself resulting from the long hydrocarbyl segments. The degradation profiles for these polymers were similar in air and nitrogen. In air atmosphere, $T_{5\%}$s were in the range of 414–438°C and char yields were in the range of 2.9–27.2%. Under air atmosphere, the 5% weight loss temperatures for the NP-ph/BA-ph polymers were approximately equivalent to those observed under nitrogen atmosphere. This suggested that oxygen almost did not play a significant role on the $T_{5\%}$ of NP-ph/BA-ph polymers. Nevertheless, the 60–75% chars remaining at 800°C was obviously higher than those of under atmospheric conditions, which related to the different degradation mechanisms and thermal properties according to the thermal history [33, 34]. The differential presentation of integral TGA curves (DTA) was shown in Fig-

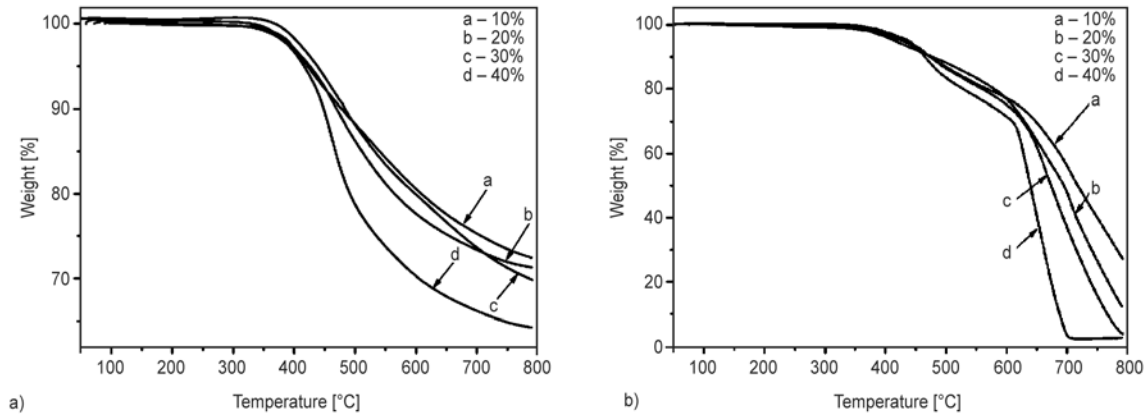

Figure 14. TGA curves of NP-ph/BA-ph composites (a) in nitrogen, (b) in air

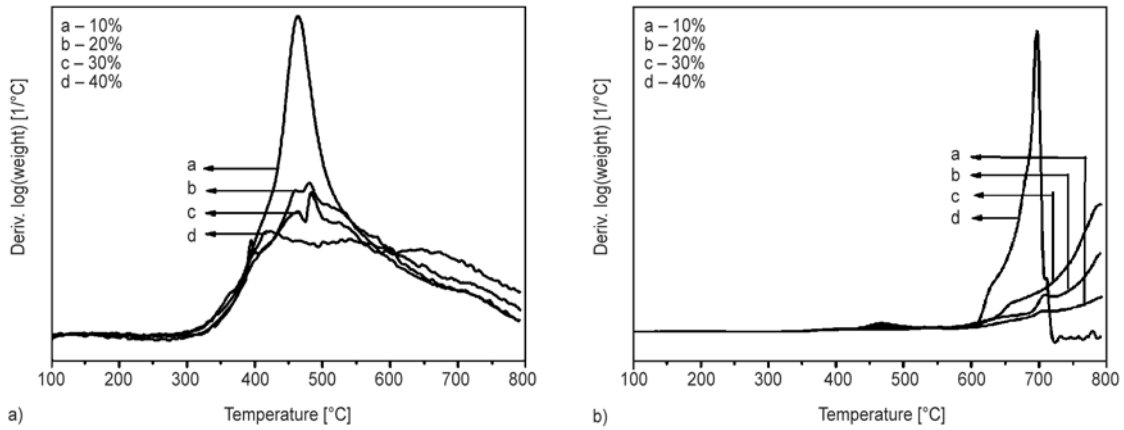

Figure 15. DTA curves of NP-ph/BA-ph composites (a) in nitrogen, (b) in air

ure 15 to improve the interpretation of the double-step character of thermal degradation. It could be seen in Figure 15a that a main degradation step was observed which started at around 350°C and reached the maximum at around 460°C. However, in Figure 15b, the double-step thermal degradation was observed at around 470 and 680°C, suggesting two major decomposition processes, which was obviously distinguished from the character of degradation in N_2. In the presence of oxygen, bridging methylene and methyl groups were preferential to be thermal-oxidatived and decomposed at around 400°C. In addition to oxidative degradation, further thermal chain scission was characteristic at elevated temperatures (>600°C). Nevertheless, in inert atmospheres, thermal chain scission, including bridging methylene and methyl groups, was the main thermal degradation process. Compared with other state-of-the-art thermosetting composites, the NP-ph/BA-ph exhibited excellent thermal and thermal-oxidative stabilities. The phthalonitrile-based composites or laminates, by comparison, showed as high $T_{5\%}$ as NP-ph/BA-ph systems [34–37]. However, these composites have to be cured at elevated temperatures (over 350°C) for a very long time (24 h or even more), which would be hard in the practical processing. The thermosetting polyimide-based composite laminates, on the other hand, were durable for a long time at 343°C, but the high-temperature machining increased the difficulty of processing and limited their potential applications. To sum up, the excellent thermo-oxidative stabilities and high T_gs, together with the sound processing conditions could enable the NP-ph/BA-ph polymers to find uses in the fields of RTM and those under some practical critical circumstances with requirements of high wears and temperatures.

4. Conclusions

A novel kind of phthalonitrile containing flexible chains (NP-ph) has been successfully synthesized and investigated. Then, the low viscosity NP-ph resin has been incorporated into the BA-ph matrix to prepare NP-ph/BA-ph copolymers and polymers with various amount of NP-ph. The curing and rheological behaviors of the NP-ph/BA-ph copolymers were studied and the results indicated that the viscosity and processability can be tuned flexibly by varying the content of NP-ph, process temperature and time. The NP-ph/BA-ph polymers were obtained underwent the curing procedure mentioned above without any other curing agents. Results demonstrated that the NP-ph/BA-ph polymer exhibited outstanding glass transition temperature (T_g >360°C) and good thermal stability ($T_{5\%}$ >420°C). Good processability and sound processing conditions, combined with the outstanding T_g as well as excellent thermal stabilities enable the as-prepared NP-ph/BA-ph copolymers to find uses under some practical critical circumstances with requirements of high wears and temperatures.

Acknowledgements

The authors wish to thank for financial support of this work from the National Natural Science Foundation (No. 51173021) and '863' National Major Program of High Technology (2012AA03A212).

References

[1] Lundström T. S., Gebart B. R.: Influence from process parameters on void formation in resin transfer molding. Polymer Composites, **15**, 25–33 (1994). DOI: 10.1002/pc.750150105

[2] Trochu F., Gauvin R., Gao D-M.: Numerical analysis of the resin transfer molding process by the finite element method. Advances in Polymer Technology, **12**, 329–342 (1993). DOI: 10.1002/adv.1993.060120401

[3] Seemann W. H.: Plastic transfer molding techniques for the production of fiber reinforced plastic structures. U.S. Patent 4902215, USA (1990).

[4] Seemann W. H.: Plastic transfer molding apparatus for the production of fiber Plastic transfer molding apparatus for the production of fiber reinforced plastic structures. U.S. Patent 5052906, USA (1991).

[5] Seemann W. H.: Unitary vacuum bag for forming fiber reinforced composite articles. U.S. Patent 5316462, USA (1994).

[6] Yan Y., Shi X., Liu J., Zhao T., Yu Y.: Thermosetting resin system based on novolak and bismaleimide for resin-transfer molding. Journal of Applied Polymer Science, **83**, 1651–1657 (2002). DOI: 10.1002/app.10073

[7] Cao G. P., Chen W. J., Wei J. J., Li W. T., Liu X. B.: Synthesis and characterization of a novel bisphthalonitrile containing benzoxazine. Express Polymer Letters, **1**, 512–518 (2007). DOI: 10.3144/expresspolymlett.2007.73

[8] Xu M., Yang X., Zhao R., Liu X.: Copolymerizing behavior and processability of benzoxazine/epoxy systems and their applications for glass fiber composite laminates. Journal of Applied Polymer Science, **128**, 1176–1184 (2013). DOI: 10.1002/app.38422

[9] Xu M., Hu J., Zou X., Liu M., Dong S., Zou Y., Liu X.: Mechanical and thermal enhancements of benzoxazine-based GF composite laminated by *in situ* reaction with carboxyl functionalized CNTs. Journal of Applied Polymer Science, **129**, 2629–2637 (2013). DOI: 10.1002/app.38988

[10] Cid J. A., Wang Y-X., Ishida H.: Cationic polymerization of benzoxazine monomers by boron trifluoride complex. Polymers and Polymer Composites, **7**, 409–420 (1999).

[11] Wang Y-X., Ishida H.: Cationic ring-opening polymerization of benzoxazines. Polymer, **40**, 4563–4570 (1999). DOI: 10.1016/S0032-3861(99)00074-9

[12] Iji M., Kiuchi Y.: Flame-retardant epoxy resin compounds containing novolac derivatives with aromatic compounds. Polymers for Advanced Technologies, **12**, 393–406 (2001). DOI: 10.1002/pat.66

[13] Hergenrother P. M., Connell J. W., Smith J. G.: Phenylethynyl containing imide oligomers. Polymer, **41**, 5073–5081 (2000). DOI: 10.1016/S0032-3861(99)00569-8

[14] Homrighausen C. L., Keller T. M.: Synthesis of hydroxy-terminated, oligomeric poly(silarylene disiloxane)s via rhodium-catalyzed dehydrogenative coupling and their use in the aminosilane–disilanol polymerization reaction. Journal of Polymer Science Part A: Polymer Chemistry, **40**, 1334–1341 (2002). DOI: 10.1002/pola.10110

[15] Zuo F., Liu X.: Synthesis and curing behavior of a novel benzoxazine-based bisphthalonitrile monomer. Journal of Applied Polymer Science, **117**, 1469–1475 (2010). DOI: 10.1002/app.31978

[16] May C. A.,Tanaka G. Y.: Epoxy resin chemistry and technology. Marcel Dekker, New York (1973).

[17] Baur R. S.: Epoxy resin chemistry. American Chemical Society, Washington (1979).

[18] Potter W. G.: Epoxide resins. Springer, New York (1970).

[19] McAdams L. V., Gannon J. A.: Epoxy resins. in 'Encyclopedia of polymer science and engineering' (eds.: Mark H. F., Bikales N., Overberger C. G., Menges G., Kroschwitz J. I.) New York, Vol 6, 322–382 (1986).

[20] Xu Y., Hoa S. V.: Mechanical properties of carbon fiber reinforced epoxy/clay nanocomposites. Composites Science and Technology, **68**, 854–861 (2008). DOI: 10.1016/j.compscitech.2007.08.013

[21] Bekyarova E.,Thostenson E. T., Yu A., Kim H., Gao J., Tang J., Hahn H. T., Chou T-W., Itkis M. E., Haddon R. C.: Multiscale carbon nanotube–carbon fiber reinforcement for advanced epoxy composites. Langmuir, **23**, 3970–3974 (2007). DOI: 10.1021/la062743p

[22] Guo H., Lei Y., Zhao X., Yang X., Zhao R., Liu X.: Curing behaviors and properties of novolac/bisphthalonitrile blends. Journal of Applied Polymer Science, **125**, 649–656 (2012). DOI: 10.1002/app.36335

[23] Zhang J., Liu X., Wen H., Xie M., Cai X.: Investigation of the properties of phthalocyanine resin containing bismaleimide groups. Polymer International, **42**, 363–366 (1997). DOI: 10.1002/(SICI)1097-0126(199704)42:4<363::AID-PI711>3.0.CO;2-0

[24] Yang X. L., Liu X. B.: Study on curing reaction of 4-aminophenoxyphthalonitrile/bisphthalonitrile. Chinese Chemical Letters, **21**, 743–747 (2010). DOI: 10.1016/j.cclet.2009.12.022

[25] Chen Z., Guo H., Tang H., Yang X., Xu M., Liu X.: Preparation and properties of bisphenol A-based bisphthalonitrile composite laminates. Journal of Applied Polymer Science, **129**, 2621–2628 (2013). DOI: 10.1002/app.38986

[26] Agag T., Takeichi T.: Novel benzoxazine monomers containing *p*-phenyl propargyl ether: Polymerization of monomers and properties of polybenzoxazines. Macromolecules, **34**, 7257–7263 (2001). DOI: 10.1021/ma0107915

[27] Chow T. S.: Molecular interpretation of the glass transition temperature of polymer-diluent systems. Macromolecules, **13**, 362–364 (1980). DOI: 10.1021/ma60074a029

[28] Hancock B. C., Zografi G.: The relationship between the glass transition temperature and the water content of amorphous pharmaceutical solids. Pharmaceutical Research, **11**, 471–477 (1994). DOI: 10.1023/A:1018941810744

[29] Forrest J. A., Dalnoki-Veress K., Stevens J. R., Dutcher J. R.: Effect of free surfaces on the glass transition temperature of thin polymer films. Physical Review Letters, **77**, 2002–2005 (1996). DOI: 10.1103/PhysRevLett.77.2002

[30] Forrest J. A., Dalnoki-Veress K., Dutcher J. R.: Interface and chain confinement effects on the glass transition temperature of thin polymer films. Physical Review E, **56**, 5705–5716 (1997). DOI: 10.1103/PhysRevE.56.5705

[31] Allaoui A., El Bounia N.: How carbon nanotubes affect the cure kinetics and glass transition temperature of their epoxy composites? – A review. Express Polymer Letters, **3**, 588–594 (2009). DOI: 10.3144/expresspolymlett.2009.73

[32] Kimura H., Ohtsuka K., Matsumoto A.: Curing reaction of bisphenol-A based benzoxazine with cyanate ester resin and the properties of the cured thermosetting resin. Express Polymer Letters, **5**, 1113–1122 (2011). DOI: 10.3144/expresspolymlett.2011.108

[33] Sumner M. J., Sankarapandian M., McGrath J. E., Riffle J. S., Sorathia U.: Flame retardant novolac-bisphthalonitrile structural thermosets. Polymer, **43**, 5069–5076 (2002).
DOI: 10.1016/S0032-3861(02)00354-3

[34] Laskoski M., Dominguez D. D., Keller T. M.: Synthesis and properties of a bisphenol A based phthalonitrile resin. Journal of Polymer Science Part A: Polymer Chemistry, **43**, 4136–4143 (2005).
DOI: 10.1002/pola.20901

[35] Dominguez D. D., Jones H. N., Keller T. M.: The effect of curing additive on the mechanical properties of phthalonitrile-carbon fiber composites. Polymer Composites, **25**, 554–561 (2004).
DOI: 10.1002/pc.20049

[36] Dominguez D. D., Keller T. M.: Properties of phthalonitrile monomer blends and thermosetting phthalonitrile copolymers. Polymer, **48**, 91–97 (2007).
DOI: 10.1016/j.polymer.2006.11.003

[37] Kuznetsov A. A., Semenova G. K.: Perspective thermally stable thermoset binders for polymer composite materials. Russian Journal of General Chemistry, **80**, 2170–2180 (2010).
DOI: 10.1134/S1070363210100464

eXPRESS Polymer Letters Vol.7, No.12 (2013) 996–1011
Available online at www.expresspolymlett.com
DOI: 10.3144/expresspolymlett.2013.98

Phase behavior of UCST blends: Effects of pristine nanoclay as an effective or ineffective compatibilizer

F. Hemmati[1], *H. Garmabi*[1*], *H. Modarress*[2]

[1]Department of Polymer Engineering and Color Technology, Amirkabir University of Technology, No. 424, Hafez Ave., Tehran, Iran
[2]Department of Chemical Engineering, Amirkabir University of Technology, No. 424, Hafez Ave., Tehran, Iran

Received 2 June 2013; accepted in revised form 18 August 2013

Abstract. The effects of unmodified nanoclay (natural montmorillonite) on the miscibility, phase behavior and phase separation kinetics of polyethylene (PE)/ethylene vinyl acetate copolymer (EVA) blends have been investigated. Depending on the blend composition, it was observed that the intercalated pristine nanoclay influences the biphasic morphology either as an effective compatibilizer or just as an ineffectual modifier. In spite of the presence of micrometer-sized agglomerated tactoids, natural nanoclay can play a thermodynamic role in reducing the interfacial tension of polymer components. The addition of clay nanoparticles was found to change the phase diagram slightly and diminishes the composition dependency of the binodal temperatures. Moreover, it was observed that a small amount of unmodified layered silicate slows down the phase separation process considerably and enhances the solubility of each polymer in the domains of its counterpart. The findings of this study verify that even poorly dispersed nanoclay with high surface tension can act as a conventional compatibilizer and change the immiscible PE/EVA blends to the partially miscible ones.

Keywords: *polymer blends and alloys, miscibility, nanocomposites, rheology, phase separation*

1. Introduction

Blending of polymers is a well-established route to create new materials, which have ultimate properties of the components to offer in a single product. However, most of polymer pairs result in immiscible blends having biphasic morphology that affects all final characteristics. One of the classical strategies to enhance the miscibility of two phases is the addition of a third component as compatibilizer. This strategy not only provides an opportunity to modify the microstructure, but also gives a chance to improve the final properties of the blends [1]. A newly developed concept, presented in this area, is the use of inorganic nanofiller in a binary blend to enhance the compatibility of polymeric components. It has been found that the addition of solid nanoparticles with at least one dimension in the nanometer scale can affect the compatibility of components and improve the physical, mechanical and thermal properties of the blends [2–5]. The improved miscibility of polymer mixtures in the presence of nanofillers has been reported by different groups with reduced dispersed phase domains, narrower droplet size distribution in matrix-dispersed morphology, enhanced ductility and mechanical properties, lower interfacial tension between two phases and more morphological stability in the subsequent melt blending processes [5–10]. As shown theoretically by Nesterov and Lipatov [11–12], the compatibilization effect of solid filler (F) on an immiscible polymer pair (A and B) can be described by the mixing free energy of system (ΔG_{mix}) which consists of the absorption free energy of each polymer on the solid surface of F (ΔG_{AF} and ΔG_{BF}) and the interaction

*Corresponding author, e-mail: garmabi@aut.ac.ir
BME-PT

energy between two polymeric components (ΔG_{AB}) as expressed by Equation (1):

$$\Delta G_{mix} = \Delta G_{AF} + \Delta G_{BF} + \Delta G_{AB} = RT(\chi_{AF}\varphi_A\varphi_F + \chi_{BF}\varphi_B\varphi_F + \chi_{AB}\varphi_A\varphi_B) \quad (1)$$

where φ_i is the volume fraction of i^{th} component and χ_{ij} is the Flory-Huggins interaction parameter between components i and j. As the authors stated, the binary blend containing solid filler would be more miscible in the case of the absorption of either both polymers or one of them preferentially on the surface of filler (either ΔG_{AF} and $\Delta G_{AF} < 0$ or one of them become less than zero). In addition to the mentioned enthalpic gain, the absorption of polymer chains on the filler surface is accompanied by another impact, that is the entropic reduction of the polymer chains, named 'entropic surface tension' of nanoparticles [13]. According to the simulation work of Balazs *et al*. [14], preferential wetting of nanofiller by one of the polymers results in slower kinetics of spinodal decomposition. Therefore, nanoparticle addition to binary mixtures and preferential absorption of polymer chains could slow down the domain growth and cause a pinning influence on the interface motions. In the similar manner, it was experimentally observed that the addition of nanoparticles could diminish the diffusion of absorbed polymeric chains and retard the phase separation phenomena [15, 16]. As it is found by Lipatov *et al*. [11, 12], this 'non-equilibrium' compatibilization mechanism of nanofillers is more profound at higher concentrations of the inorganic component wherein the distance of two adjacent solid particles in the system can be comparable to the gyration radius of unperturbed polymer coils. Contrary to the non-equilibrium compatibilization mechanism, the equilibrium mechanism is accompanied by a promoted thermodynamic stability of the hybrid system. Zhang *et al*. [17] studied the thermodynamic effect of nanoclay in an immiscible polymer blend as an equilibrium phenomenon whereupon the biphasic morphology was stabilized during the annealing time. The applied time scale of experiments was much longer than the time scale required for polymer diffusion. By incorporation of other inorganic nano-size particles including spherical fillers and nanotubes in the blend, this was observed that nanoclay with large aspect ratio is more efficient in compatibilizing and reducing the interfacial tension by providing large amounts of *in-situ* grafts between two components at the interface.

Although there have been several researches on different aspects of nanofiller induced miscibility in the binary blends, the phase diagram and the interaction parameter of polymeric pairs in the presence of inorganic nanoparticles have not been studied intensively. The effect of fumed silica on the phase diagram of a lower critical solution temperature (LCST) blend was investigated [11, 12] and it was found that the miscibility window of phase diagram directly impressed depending on the filler concentration. The thermodynamic implications were proposed to govern by simultaneous action of two mechanisms: selective absorption of one of polymers on the solid surface and redistribution of macromolecules with respect to their molecular weights between the bulk and the boundary layer (in the vicinity of filler surface) and the alteration of the interaction parameter between polymer constituents. Likewise, Yurekli *et al*. [18] studied the effects of layered silicate on the phase behavior of polystyrene (PS)/poly(vinyl methyl ether) (PVME) blends. They observed that the phase transition boundary was not considerably changed by adding 0.04 volume fraction of nanoclay. In contrast to their work, Huang *et al*. [19] found that the addition of nanosilica increased the phase separation temperature of a LCST blend and diminished the interaction parameter (χ_{AB}). Moreover, the solubility of each component in the other phase domains was enhanced. Following by them, Mabrouk *et al*. [20, 21] reported that nanoclay could alter the phase behavior both by thermodynamics and kinetics effects and the phase transition mechanism changes from spinodal decomposition to nucleation and growth by addition of nanoparticles. Using the same binary blends, Gharachorlou and Goharpey [22] by means of rheology examined the influence of hydrophilic nanosilica having the size comparable to the chain gyration radius and illustrated the phase boundary increased up to 10°C toward the heterogeneous region, despite the fact that nanoparticles migrated to one of the component domains. Interestingly, Gao *et al*. [23] stated that the compatibilizing effect of nano-size silica on the phase separation temperature of the studied LCST blends strongly depended on the blend composition. Also, they deduced that micron size silica could scarcely make

a noticeable impact on the phase separation of blend.

As explained, different aspects of nano-size particle compatibilization influence on varied binary blends have been addressed in the literature. Among them, the phase behavior alteration of LCST blends in the presence of inorganic nanofillers is worth mentioning. However, to the best of our knowledge, the implications of nanoparticles for phase behavior of the upper critical solution temperature (UCST) blends needs to be investigated. In this work, in order to study the influences of inorganic nanofiller on the miscibility window and phase separation kinetics of an UCST blend, polyethylene (PE)/ethylene-vinyl acetate copolymer (EVA) blends were chosen and compounded with natural montmorillonite (MMT) clay. The phase transitions of these blends including liquid-liquid and solid-liquid phase separation had been evaluated previously. It is noteworthy that PE/EVA/clay hybrid systems with enhanced thermal properties and flame retardancy are demanded for wire and cable insulating applications extensively [4]. The main objective of the present research is to examine the effects of unmodified nanoclay on the miscibility of PE/EVA blends during phase transition phenomenon. Attempts are particularly made to answer this question that whether or not the nanoparticles can act as an effective interfacial modifier while the enthalpic interactions of polymer-filler pairs are extremely weaker than the enthalpic interaction of two polymer components; i.e. χ_{AF} and $\chi_{BF} >> \chi_{AB}$. Because of this goal, pristine nanoclay without any surface modification was chosen as nanofiller. Moreover, another concern of the present study is to probe the nanoclay localization influences on the biphasic microstructure and composition-dependent interactions existed in the PE/EVA blends. By means of linear viscoelastic responses, effort is made to track the effects of chain confinement on the kinetics of phase separation phenomena. In addition to the rheological measurements, dynamic mechanical analysis (DMA), microscopic observations and interfacial tension measurements were carried out to support the findings of this work.

2. Experimental part

2.1. Materials and sample preparation

High density polyethylene (HDPE, BL3 grade) from Arak Petrochemical Company (Arak, Iran) and ethylene vinyl acetate copolymer (EVA, Seetec VA910) from Hyundai Company (Seoul, South Korea) and natural montmorillonite (MMT, Cloisite Na^+) from Southern Clay Products Inc. (Texas, USA) were used as received. The characteristics of the polymeric components are presented in Table 1. Irganox B225 (Ciba Specialty Chemicals Inc., Basel, Switzerland) was applied to thermally stabilize the prepared samples at 0.1 wt%. PE/EVA blends and PE/EVA/MMT compounds at various polymer concentrations, ranging from 30 to 70% of EVA by weight, were prepared by a laboratory batch internal mixer (BRABENDER PL2200, Duisburg, Germany) at a temperature of 155°C with a rotor speed of 60 rpm. Melt-compounding was continued for 10 min then the film and sheet samples were prepared by compression molding at temperature of 150°C under 15 MPa pressure. The concentration level of MMT was fixed at 3 wt%. In the remaining parts, the samples will be coded as PExEVAyMMTz wherein *x*, *y* and *z* stand for PE, EVA and MMT weight fractions, respectively. For samples in which one of the components is not included, the material's name will be omitted from the corresponding code.

2.2. Characterization

2.2.1. Rheological measurements

All the rheological measurements were performed using a parallel plate Paar-Physica rheometer (diameter of 25 mm, gap of 1 mm, Ashland, VA 23005, USA). To prevent moisture absorption and sample degradation, all examinations were carried out at nitrogen atmosphere. The performed small amplitude oscillatory shear measurements consisted of:

Table 1. Characteristics of the studied materials

Sample	Density [g/cm^3][a]	MFI [g/10 min][a]	VAc content [wt%][a]	M_w [g/mol][b]	PDI[b] (M_w/M_n)	OIT [min][c]
HDPE	0.954	1	–	330 000	6.2	>200
EVA	0.950	400	28	56 000	3.6	>90

[a]given by the supplier

[b]measured using PL-GPC 220 High Temperature GPC/SEC System (Agilent Technologies, California, USA)

[c]measured at 180°C in pure oxygen atmosphere using the stabilized samples

(a) Isochronal dynamic temperature ramps by reducing the temperature from the mixed region (180°C) to the phase-separated region, at a small strain in the linear viscoelastic regime (1%, as determined by preliminary isothermal dynamic strain sweeps) and the cooling rate of 1°C/min; (b) Isothermal dynamic time sweep for 3 hr at temperatures in the vicinity of phase separation boundary at a fixed frequency of 1 s^{-1} and a given strain of 1%, in order to evaluate the phase separation kinetics. Seeking this purpose, the samples were annealed at 180°C, and then quenched to the desired temperature to track the rate of phase separation. In addition, dynamic time sweeps at 180°C for 50 min were performed on the stabilized PE, EVA, PE100MMT3 and EVA100MMT3 samples to ensure that the measurements were carried out without the interference of thermal degradation. Apart from the mentioned rheological examinations, the oxidation induction time (OIT) measurements demonstrated that the oxidation reaction of the mentioned samples began at times longer than 90 min in pure oxygen atmosphere; (c) Isothermal dynamic frequency sweeps at a linear strain of 1% were also performed.

2.2.2. Morphological observations

Demixing temperature of the prepared samples were determined by optical microscopy (Leica DMRX, Buffalo Grove, IL 60089, USA) equipped with a heating block (Linkam LTS 350, Surrey, UK) using films having the thicknesses about 50 μm. The cooling rate inside the heating block was 1°C/min. To investigate the state of nanoclay dispersion and localization, the height and phase mode images of the atomic force microscopy (AFM) were prepared using a Dualscope, DME Atomic Force Microscope (Copenhagen, Denmark) equipped with a DS 95-50-E scanner and an AC probe. Biphasic morphology of samples was examined using a field emission scanning electron microscopy (Hitachi High-Technologies Co., Tokyo, Japan). The cryofractured samples were etched in xylene (Extra pure, Ph Helv vl, Merck KGaA, Darmstadt, Germany) for 6 hr at 50°C to extract the EVA-rich domains selectively. The droplet size for the samples with matrix-dispersed morphology was measured using image analysis software. The average diameter of dispersed domains (D_v) was calculated from the area of the domains in SEM micrographs. At least 250 dispersed-phase domains were analyzed for each sample. To determine the EVA continuity index and to study the biphasic morphology in 3 dimensions, the samples with the specified weights were stirred in xylene for 7 days at a constant temperature of 50°C for selectively removal of EVA domains. The weight fraction of the extracted EVA phase was determined as the co-continuity index of EVA-rich phase. For probing the nanoclay dispersion more precisely, TEM micrographs were prepared using a Philips CM-30 (Amsterdam, Netherlands) operating at accelerating voltage of 200 kV. Following the same approach, XRD patterns were recorded on a Philips XPERT diffractometer (Almelo, The Netherlands) using Cu tube. Data were obtained within the scattering angles of 1–10° at a step size of 0.02°.

2.2.3. Thermal analysis

To study the miscibility of the polymeric component in the amorphous region, the viscoelastic properties of the sheet samples were measured by DMA using TTDMA Dynamic Mechanical Analyzer (Triton Technology Ltd, Lincolnshire, UK). The experiments were performed in single bending mode from –160 to 100°C at a frequency of 1 Hz with a programmed heating rate of 5°C/min.

2.2.4. Interfacial tension measurement

Interfacial tension of PE/EVA in the pure state and in the presence of nanoclay was measured using sessile drop and imbedded fiber retraction methods at temperature of 155°C. For sessile drop measurements, the drops of EVA were formed on the sheets of PE and PE100MMT3. The samples were remained in nitrogen atmosphere until the mechanical equilibrium was reached (approximately 5 hrs). Then, the samples were suddenly cooled down to 0°C, fixed, cut with a surgical blade, and then observed using optical microscope. Afterwards, the contact angles were measured. The interfacial tensions were evaluated by the Neumann triangle rule using the surface tensions of PE, EVA and PE100MMT3 samples at 155°C. The surface tensions were determined using a pendant drop instrument at nitrogen atmosphere and the results are collected in Table 2. Another method used to measure the interfacial tension in this study was imbedded fiber retraction. The melt spun threads of PE and PE100MMT3 were chopped and annealed at temperature of

100°C for 24 hr in a vacuum oven, then, the short fibers were imbedded in a matrix of pure EVA. Moreover, the PE short fiber sandwiched between two EVA100MMT3 films was also prepared. The obtained sandwich type assemblies were placed in the heating block of optical microscopy and heated to 155°C. Then, the evolution of the fibers was recorded. Using Carriere and Cohen's theory [24, 25], the interfacial tension between fibers and matrices were measured. The zero shear viscosity of the samples required for the calculations were determined by the isothermal dynamic frequency sweeps using Carreau-Yasuda model [26] and the obtained data are presented in Table 2. The results of interfacial tension measurements given in the following sections are the arithmetic means of 3–5 replicates. To ensure that the examinations were carried out in stable conditions without the interference of thermal degradation, themogravimetry analysis (TGA) were performed using a Shimadzu TGA-50 Thermoanalyzer instrument (Kyoto, Japan) in nitrogen atmosphere. The obtained results indicated that the weight loss of PE, EVA, PE100MMT3 and EVA100MMT3 samples were negligible for 5 hr at temperature of 155°C.

The interfacial tension of EVA/MMT and PE/MMT were determined via contact angle measurement of the polymer melt drops on nanoclay disks. The MMT powder were pressed into hard disks under 15 MPa pressure. The average roughness of the prepared disks was examined by AFM topography scans and it was about 120 nm. The drops of pure polymers were formed on the MMT disks at melt-compounding process temperature. Then, the samples were left in nitrogen atmosphere to reach the mechanical equilibrium. The equilibrium advancing and receding contact angles were measured by video recordings of the drops.

Table 2. Surface tension and viscoelastic properties of the samples used in the interfacial tension measurements at 155°C

Sample	Surface tension [mN/m]	Zero shear viscosity [Pa·s]	G′ at ω = 0.1 rad/s [Pa]
PE	26.7±1.1	113 980	1900
EVA	28.8±0.9	60.4	0.185
PE100MMT3	31.8±0.2	216 540	1920
EVA100MMT3	32.8±0.9	192 770	0.508

3. Results and discussion

3.1. Microstructure

3.1.1. Biphasic morphology

By considering the SEM micrographs of the prepared blends and the related nanocomposites (Figure 1a–1f), it can be assessed that pristine MMT has a noticeable effect on the biphasic morphology of PE/EVA blends. Regardless of the sample composition, the SEM micrographs obviously indicated that the presence of natural nanoclay did not vary the type of blend morphology. Despite this fact, the addition of the nanoparticles resulted in the formation of narrower fibrils, finer biphasic morphologies and reduced dispersed-domain size for all of the prepared blends except for PE70EVA30. It is noteworthy that the mentioned compatibilization effect of MMT was also deduced from the SEM micrographs of PE40EVA60 and PE30EVA70 blends which are not shown in Figure 1. In contrast to the observed compatibilization effect of nanoclay, the EVA domain size increased for PE70EVA30 blend distinctly by taking a closer look at Figure 1a and 1b. Quantitative analysis of the dispersed domain size for the samples with matrix-dispersed morphology (PE70EVA30 and PE30EVA70 blends plus the related nanocomposites) showed that the corresponding diameter (D_v) of EVA domains was raised from 9.26 to 26.27 μm, whereas D_v of PE dispersed-domains exhibited an inverse trend by the presence of nanoparticles and was reduced from 16.43 to 7.67 μm for PE30EVA70 blend.

According to the results, the biphasic morphology transition from matrix-dispersed to co-continuous, by increasing the EVA content, caused an alteration in the influence of inorganic filler from demixing effect to a more conventional compatibilization effect. Further evidence on this phenomenon is the results of EVA co-continuity index measurements collected in Table 3. The mentioned examinations as a 3-dimensional analysis of biphasic morphology proved that the continuity of EVA-rich domains was enhanced or remained unchanged by adding the nanoparticles except for PE70EVA30 blend. The EVA co-continuity index was declined for the PE-rich blend contained nanofiller (PE70EVA30MMT3). The compatibilization impact of nanoparticles resulted in the domain size reduction and co-continuity index increment in the polymer mixtures have

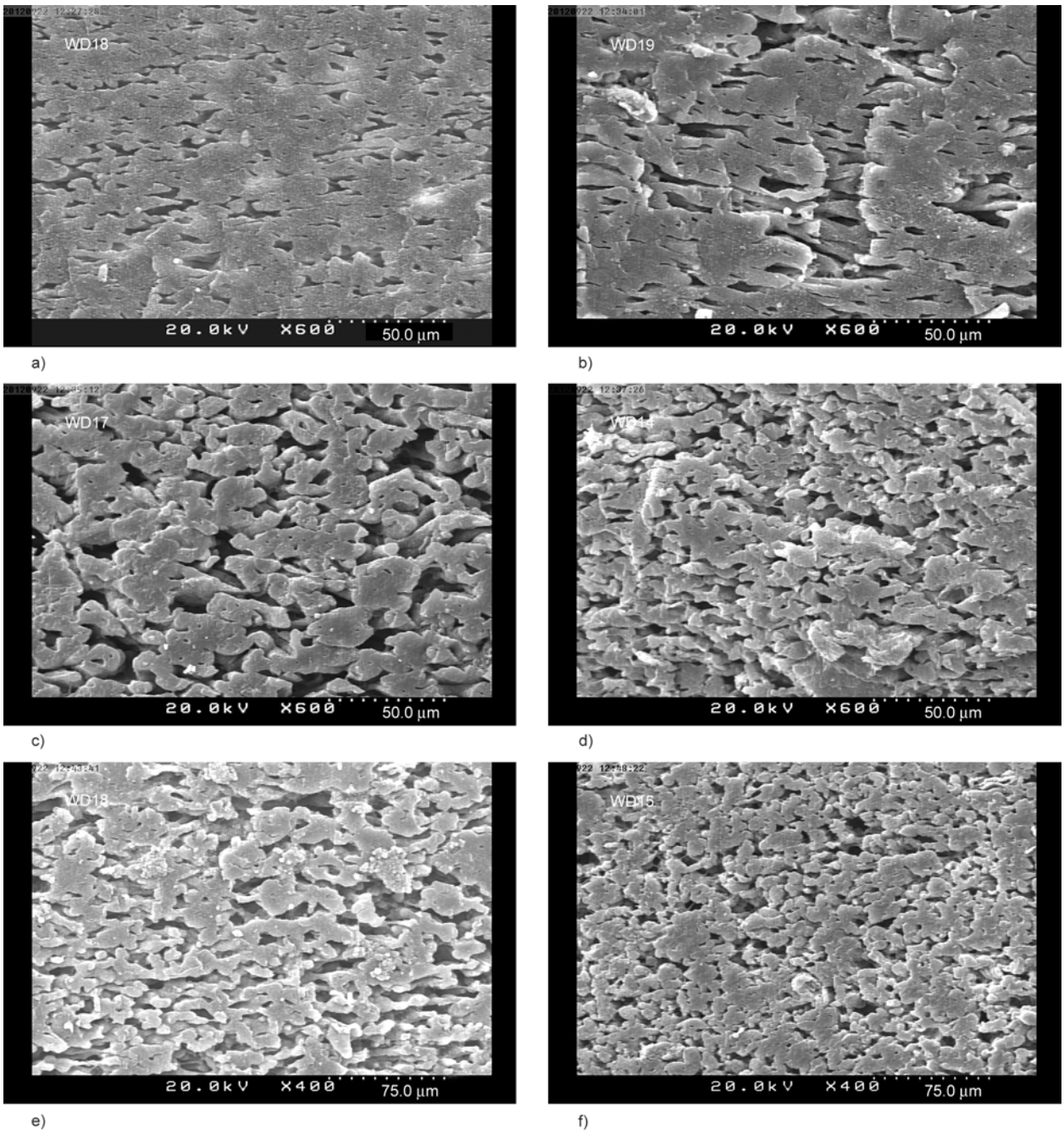

Figure 1. SEM micrographs of (a) PE70EVA30, (b) PE70EVA30MMT3, (c) PE60EVA40, (d) PE60EVA40MMT3, (e) PE50EVA50, and (f) PE50EVA50MMT3

Table 3. Co-continuity index [%] of EVA in the virgin blends and the related nanocomposites containing 3 wt% MMT

Sample	PE100	PE70EVA30	PE60EVA40	PE50EVA50	PE40EVA60	PE30EVA70	EVA100
Virgin blend	0	73.8	83.0	90.8	97.9	5.53	0
Nanocomposite	0	67.3	89.5	90.9	97.0	16.80	0

been also reported by other groups [5–7, 27]. However, the observed contradiction between two different effects of pristine MMT on the biphasic morphology can be clarified by investigating the state of nanoparticle localization as well as dispersion.

3.1.2. The states of MMT dispersion and localization

To investigate these states, the AFM images and TEM micrographs of PE70EVA30MMT3, PE60EVA40 MMT3 and PE50EVA50MMT3 samples were pre-

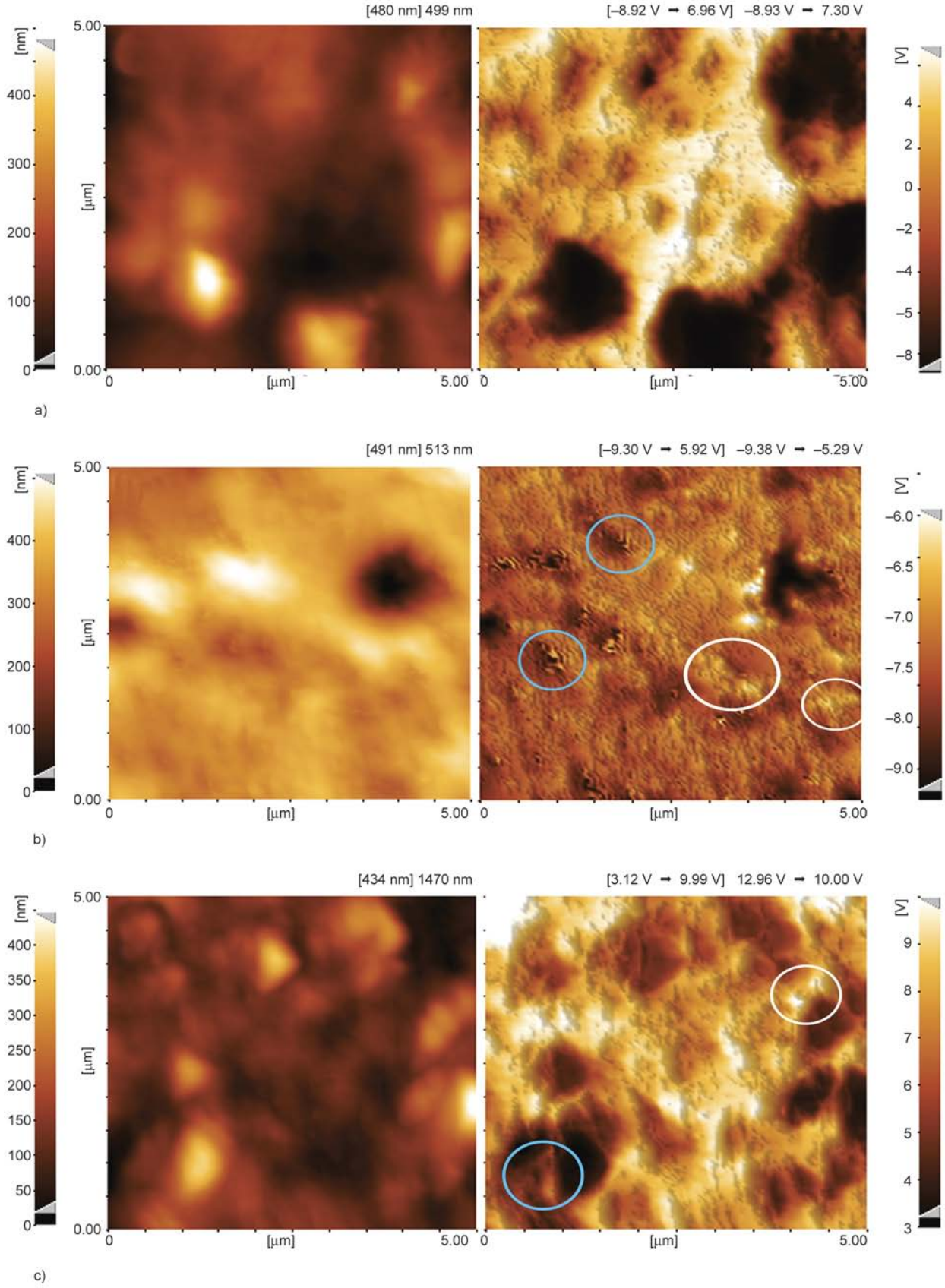

Figure 2. AFM images of (a) PE70EVA30MMT3, (b) PE60EVA40MMT3, (c) PE50EVA50MMT3. Left and right images show height and phase-mode micrographs, respectively. Z-axes are on the right and left sides of images. Blue and white ellipses mark nanoclay stacks partitioned into EVA and PE domains, respectively.

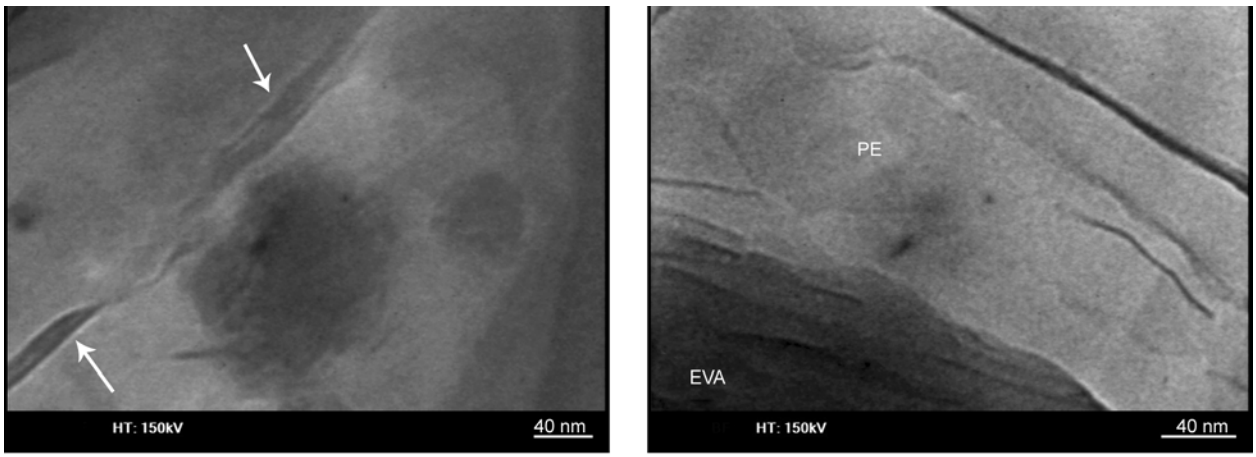

Figure 3. TEM micrographs of (a) PE70EVA30MMT3 and (b) PE60EVA40MMT3. Intercalated MMT stacks were marked by arrows. EVA dispersed-domains can be discerned as darker areas.

pared and illustrated in Figure 2 and 3. The phase contrast images of the scanning force microscopy have been deduced to be sensitive to the sample surface properties such as modulus, viscoelastic characteristics and chemical composition [28]. Thus, different components of PE/EVA/MMT films having highly different stiffness and viscoelasticity were contrasted with each other sharply, especially in the phase-mode image of PE70EVA30MMT3 sample. As can be found in the phase contrast image of PE70EVA30MMT3 sample (Figure 2a), EVA domains were observed as black holes and brown features. Whereas PE phase could be recognized as yellow areas in the images. Likewise the other work [29], inorganic nano-layered stacks can be identified as white features in PE phase and light brown ones in EVA domains. A comparison of the phase contrast images of these nanocomposites showed that the nanoparticles were mainly confined to PE phase and the interface of two phases in PE70EVA30 MMT3 sample (see Figure 2a). While for the other nanocomposites, silicate nanolayers were localized in EVA domains as well. Blue and white ellipses in Figure 2b and 2c mark the nanoclay stacks partitioned into EVA and PE domains, respectively. Due to the larger amounts of nanoparticles localized in EVA domains and enhancements of EVA stiffness and viscoelasticity, the phase contrast of two phases were reduced for the nanocomposites containing more than 30 wt% of EVA. In a similar manner, TEM micrographs of these nanocomposites verify the observed states of MMT partitioning. As shown in Figure 3a, intercalated nanoclay stacks were localized in PE for PE70EVA30MMT3 nanocomposite, which marked by white arrows and EVA darker domains were empty of MMT. Contrary to this nanocomposite, MMT stacks can also be found in EVA domains and at the interface of two phases in the other nanocomposite (see Figure 3b).

The nanoparticle preference for being thermodynamically localized in which domains was quantitatively evaluated by measuring the mechanical equilibrium contact angles and the interfacial tension between each polymer and nanoclay disks. The mentioned interfacial tensions were calculated using the Young equation with the assumption that the solid surface is perfectly smooth and rigid. The roughness measurements on the prepared clay disks showed that the solid surface was relatively flat (mean roughness ($R_a \simeq 120$ nm). The Young contact angles were determined using advancing and receding equilibrium angles following the work of Tadmor [30]. The results represented in Table 4 show that contrary to the EVA contact angle (θ_c <90°), the PE contact angle on pristine nanoclay is more than 90° indicating low wettability and solid-liquid weak interaction. Higher wettability of the EVA melt led to the lower amount of interfacial tension. Therefore, the EVA melt at processing temperature could wet the nanoparticle surfaces better. In spite of this fact, the measured interfacial tensions are not

Table 4. Equilibrium Young contact angle (θ_c) of polymer melts on nanoclay disks and corresponding interfacial tensions measured at 155°C

Polymer drop	θ_c [°]	Interfacial tension [mN/m]
PE	99.7±3	296.5±2.2
EVA	19.1±1	264.8±1.5

Table 5. XRD results of MMT and some of the prepared samples

Sample	MMT	PE100MMT3	PE70EVA30MMT3	PE50EVA50MMT3	PE30EVA70MMT3	EVA100MMT3
Peak, 2θ [°]	7.49	1.89;7.1	1.74;7.04	1.88;6.85	2.03;7.49	2;7.49
Related d-spacing [nm]	1.18	4.66;1.24	5.07;1.26	4.7;1.29	4.35;1.18	4.41;1.18

extremely different because of high surface energy of unmodified nanoclay.

Due to this high surface energy of natural nanoclay, silicate nanolayers fell through being dispersed during melt-compounding process and remained aggregated into micrometer-sized tactoids which can be observed even by the optical microscopy at higher magnifications (refer to part 3.3). Although the applied polymers and the inorganic unmodified nanofiller were expected to be thoroughly immiscible, intercalated morphology was achieved for the nanocomposites on the evidence of the following examinations. According to the modeling work of Ginzburg *et al*. [31], even in the immiscible part of the phase map for the clay-polymer system wherein the interaction between clay and polymer is too weak, the intercalated morphologies still could be obtained because of the equilibration of densities in polymer bulk and clay galleries. The Peak characteristics of XRD patterns for pristine MMT and the prepared nanocomposites are presented in Table 5. For the nanocomposites, two distinct peaks were discerned in XRD patterns which appeared at smaller angles, 2θ (~2 and ~7°), than the peak position of natural MMT (7.49° and corresponding d-spacing of 1.179 nm) indicating an increment in the d-spacing of clay platelets.

Shifting the peaks of PE70EVA30MMT3 and PE50EVA50MMT3 compounds toward lower angles in comparison with the peak position of PE100MMT3 sample is worthy to be considered. During sample preparation process, low melting EVA phase (melting temperature (T_m = 65.9°C) could coat the clay stacks and diffused into the clay interlayer spacing before melting of the PE phase (T_m = 132.8°C). Because of EVA chain diffusion, clay d-spacing increased and the hydrophilic nature of nanoparticle surfaces was modified. Thus, it could facilitate the nanoclay intercalation by hydrophobic PE macromolecules. The existence of both polymer chains in the same gallery was also reported by other groups [5, 6]. Obtaining the intercalated morphology in the nanocomposites can also be verified by microscopic observations. TEM micrographs shown in Figure 3 indicated the achievement of intercalated microstructure for the prepared hybrid systems.

3.1.3. Effective parameters for morphology development

Better understanding of the microstructure of nanocomposites could clarify the observed composition-dependent effect of nanoparticles on the biphasic morphology. In the melt blending process of two polymers (*A* and *B*), the deformation and breakup of domains relies on capillary number (*Ca*) and viscosity ratio (*P*) (Equations (2) and (3)):

$$Ca = \frac{\tau R}{\gamma_{AB}} \tag{2}$$

and

$$P = \frac{\eta_d}{\eta_m} \tag{3}$$

where τ, R and γ_{AB} are the applied stress of external flow, characteristic domain size and interfacial tension, respectively. In addition, η_m and η_d are the viscosity of the matrix and dispersed phases, respectively. When *Ca* exceeds a critical value (Ca_{crit}), the domain breakup occurs. Ca_{crit} depends on the viscosity ratio and reaches the minimum value at $P = 1$ [32]. The presence of natural MMT in the used polymers and the resultant chain confinement in the clay galleries alters the viscosity and elasticity ratio. As can be seen in Table 2, the nanoparticles have significant influence on the viscoelastic properties of the EVA phase and increase the zero shear viscosity up to 3 orders of magnitude. Comparing with the EVA polymer, this effect is not very noticeable for the PE phase. The addition of 3 wt% of natural MMT to the PE polymer enhanced the zero shear viscosity to almost twice its value. As a result, for the obtained hybrid systems containing more than 30 wt% of EVA, in which the amount of nanoparticle localized in EVA domains is substantial, the viscosity and elasticity ratio of phases change and become closer to 1. In other words, the localization of nanoclay in EVA phase reduces the viscoelastic asymmetry of phases in these systems, which is a direct result of more considerable effect

of MMT on the EVA viscoelastic properties. Therefore, Ca_{crit} diminishes and breakup can take place at lower shear rates. Besides, Wu's empirical method (Equation (4)) [33] verified that the characteristics domain size is brought down as viscosity ratio approaches to 1:

$$\frac{\tau \eta_m R}{\gamma_{AB}} = 4(P)^{\pm 0.84} \quad (4)$$

where the positive exponent is for $P > 1$ and the negative one for $P < 1$. Hence, as the viscosity ratio approaches to 1 for the mentioned nanocomposites, R reduces to lower values. In contrast to these nanocomposites, the EVA-dispersed compound wherein the majority of clay stacks were confined to the PE matrix has even a lower amount of viscosity ratio in comparison with the pure blend (PE70EVA30). As a result, Ca_{crit} and resultant droplet size are raised. This state of partitioning worsens the dynamic asymmetry of two components. However, the MMT localization in the PE phase for PE70EVA30MMT3 is not thermodynamically favorable and subsequent melt-blending process may shift it to the EVA dispersed domains.

Another influential factor in dictating the final morphology is the interfacial tension between the two polymers. The interfacial tension of the pure components and the pristine nanoclay modified constituents are gathered in Table 6. By adding 3 wt% of nanofiller to each phase, the interfacial tension between the polymers was diminished to the lower values, especially for the systems wherein the PE phase contained natural MMT. The observed decline in γ_{AB} can explain the interfacial activity of unmodified filler stacks at the interface of the PE and EVA phases, though this effect does not seem to be as significant as the interfacial activity of organically modified nanoclay evaluated in other blends [5–7]. However, the observed interfacial tension reduction can have an impact on the deformation and breakup of blend domains, which is not our priority to study it in this work. Nonetheless, the compatibilization influence of the pristine MMT causing a decrease in the value of γ_{AB} does not seem to dominate the development of biphasic morphology in comparison with the viscosity ratio factor for PE70EVA30 MMT3 nanocomposite.

Table 6. Interfacial tension (γ_{AB}) between PE and EVA in the presence of natural MMT measured at 155°C

Measurement method	Fiber/Drop	Matrix	γ_{AB} [mN/m]
Imbedded fiber retraction	PE	EVA	1.79±0.47
Imbedded fiber retraction	PE	EVA100MMT3	1.4±0.41
Imbedded fiber retraction	PE100MMT3	EVA	0.97±0.30
Sessile drop	EVA	PE	2.16±0.63
Sessile drop	EVA	PE100MMT3	1.07±0.25

3.2. Phase separation diagram

To investigate the phase separation of PE and EVA domains in the melt state before the crystallization temperature of PE, two methods were used to determine the phase transition boundary: phase separation phenomenon recorded by the optical microscopy and the isochronal dynamic temperature sweeps. Figure 4 illustrates the dynamic temperature experiment of PE60EVA40 and PE60EVA40MMT3 samples during cooling ramp from well-mixed to the phase separated region. As can be observed in this

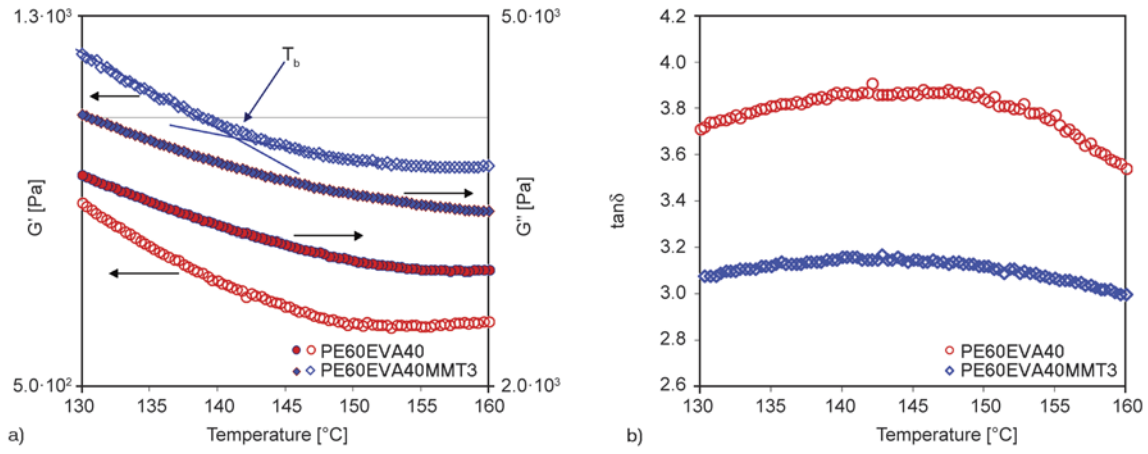

Figure 4. Isochronal dynamic temperature of (a) G' (hollow symbols) and loss modulus (G'') (filled symbols) and (b) tan δ for PE60EVA40 and PE60EVA40MMT3 samples

figure, a notable change in the slope of moduli is made as temperature approaches the phase transition boundary. Moreover, the addition of pristine nanoclay does not affect the viscoelastic behavior of the blend qualitatively. Only an increment in the magnitude of moduli and a reduction in the amount of loss tangent ($\tan\delta$) can be seen. For the blends with weakly dynamic asymmetry due to small differences in the glass transition temperature of components such as the ones studied here, the contributions of concentration fluctuation and interface to the storage modulus (G') are not substantial and just a deviation from the temperature dependence of G' in the mixed region can be observed [23]. Therefore, the temperature at which an increment in the slope of G' is detected and the corresponding peak position of tan δ is employed to determine the onset temperature of phase separation. The demixing temperature of the prepared samples was also measured by optical microscopy. By cooling down the homogeneous melt, the threshold temperature below which phase separated domains were clearly seen was identified as binodal temperature (T_b). The phase separation diagrams of the prepared blends and nanocomposites obtained by the optical microscopy and rheology are displayed in Figure 5. The results demonstrated that T_b of the blends slightly decreased to the lower temperatures by adding pristine nanoclay except for PE70EVA30MMT3 sample. It seems that the presence of unmodified nanoparticles could diminish the composition dependency of phase transition temperature. According to the results of an analytical theory proposed by Ginzburg [13] which was developed to describe the impact of nanoparticles on the thermodynamics of binary polymer blends, at larger size of nanofillers, the entropy reduction of polymer chains due to the absorption on the solid surface becomes critical and it causes the homogeneous system to be destabilized. It is suggested that for these hybrid systems, the phase separation occurs between polymer-rich and nanoparticle-rich regions like conventional behavior of colloid-polymer mixtures. For the prepared nanocomposites that contained micrometer-sized agglomerated tactoids, the polymer-nanoparticle segregation could happen and worsen the system miscibility induced by nanoclay stacks. (It will be explained in the following section.). However, the mentioned segregation could intensify when the majority of nanoparticles localized in the more unfavorable phase domains (PE domains in PE70EVA30MMT3 sample). It has been confirmed both theoretically and experimentally that in the case wherein nanofiller prefers the minority component like PE70EVA30MMT3, the presence of nanoparticles reduces the system miscibility and phase separation temperature shifts to the lower values for LCST blends [11, 13, 23].

As mentioned before, the interfacial tension between each polymer component and unmodified nanoclay is remarkably higher than the interfacial tension of the used polymers (about 2 orders of magnitude). In spite of weak interaction of the used polymers with pristine nanoclay in comparison with the interaction

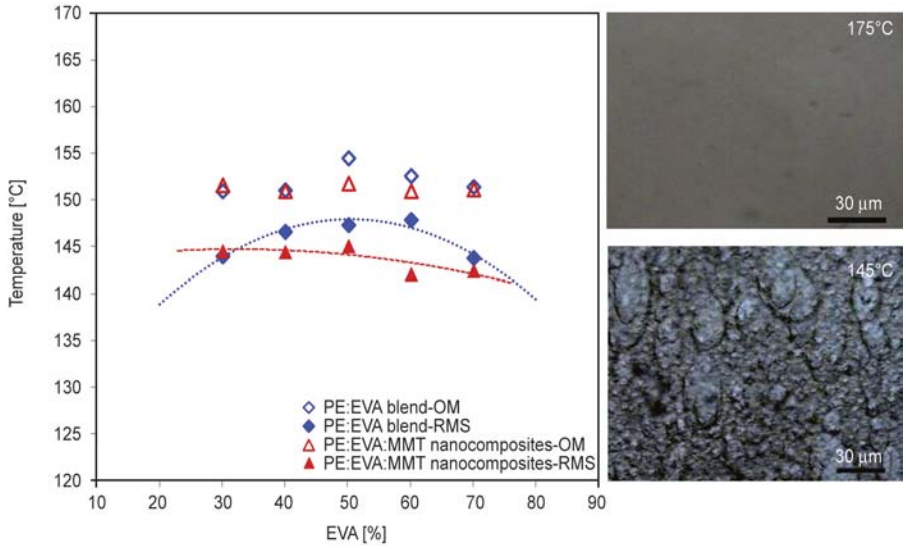

Figure 5. Phase diagram of PE:EVA blends and PE:EVA:MMT nanocomposites determined by means of rheology (RMS) and optical microscopy (OM). Lines are drawn to guide eye.

between two phases (γ_{AF} and $\gamma_{BF} >> \gamma_{AB}$), the addition of nanoparticles was observed to improve the compatibility of the virgin blends a little. According to the theoretical work of He *et al*. [34], the intermixing of polymers can be promoted in the presence of nanofiller, even nanoparticles with relatively larger interaction parameters with polymer components than the interaction parameter of two polymers.

3.3. Phase separation kinetics

Nanofillers can influence the domain growth and phase separation kinetics of a binary blend by the pinning effect, which is considered as non-equilibrium compatibilization mechanism. The interaction of polymeric constituents with the solid surface diminishes macromolecular mobility, chain entropy and resultant phase separation rate in the system [11, 12, 16]. Seeking the track of phase transition kinetics, the complex viscosity (η*) of the prepared samples were measured at different temperatures across the phase diagram and are illustrated in Figure 6a and 6b accompanied by the same results calculated via theoretical mixing rule. It can be clearly seen that η* of the virgin blends represents a definite positive deviation from theoretical results of mixing rule at higher temperatures wherein the melt is well-mixed. This result can be due to the cooperative motion or the collective relaxation of mixed polymer chains. Contrary to the positive deviation, η* of the obtained blends showed a negative deviation from the results of mixing rule as the temperature reduced and phase separation intensified apart from the PE-rich blend (PE70EVA30). The noticeable positive deviation of this blend at lower temperatures can be an outcome of the polymer chain interlocking at the interface. While the observed negative deviation of the others below the miscibility window is resulted from the formation of weak interface between two phases.

Although the pure mixtures showed a complicated positive-negative deviation for η* at temperatures far below the phase boundary, the complex viscosity of the obtained nanocomposites demonstrated a positive deviation for all compositions even at the lowest measured temperature, i.e. 130°C. This behavior can be explained by two different actions of nanoclay stacks: firstly, providing in-situ grafts at the interface of phase-separated domains and reducing the interfacial tension; secondly, retarding the phase separation phenomenon due to the entropy reduction and diminished mobility of the polymer chains interacted with the inorganic solid surfaces. The latter action of nanoparticles inhibits the phase-separated domains to be thoroughly purified from the chains of other phase in the time-scale of experiment. To evaluate this effect, i.e. the non-equilibrium compatibilization impact of nanofiller, isothermal time sweep experiments were performed at equal depth in phase-separated region on the samples with 50:50 compositions and PE-rich ones (PE70EVA30 and PE70EVA30MMT3) displayed in Figure 6c. Clearly, for both samples, PE50EVA50 and PE50EVA50MMT3, the storage modulus continuously decreased with time after showing a maximum. The rate of this reduction was substantially affected by the addition of pristine MMT. Even though the virgin blend reached approximately the saturated stage, the magnitude of G' for PE50EVA50 MMT3 sample was continuing its gradual decline with time, even after passing 10 000 s, indicating much slower phase separation process in the presence of nanofiller. In the vicinity of nanoclay stacks, the macromolecular mobility reduces due to the restriction imposed by the intercalated morphology. As a result, the diffusion process of polymer chains is retarded causing a sharp decline in the amplitude of concentration fluctuation growth rate during phase separation phenomenon.

By considering the time sweep results of PE-rich samples (Figure 6c), it seems that nanoparticles in this blend play the same role as the one in PE50EVA50 blend and apply constraints on the concentration fluctuation process. In the time-scale of the measurements, the storage modulus of PE70EVA30 sample illustrates its continuous reduction with time, whereas for the corresponding nanocomposite, seemingly, G' has passed just the early stages of phase separation process. The slower phase transition phenomenon of this blend in the presence of pristine MMT can be verified by the optical microscopy images shown in Figure 6d and 6e. The observations indicate that the phase-separated domains, which can be discerned by optical microscopy, form over a longer period in the presence of nanoparticles and develop slower. The obtained results can confirm that even when the majority of nanoclay stacks is localized in one of the component domains, i.e. PE, nanoparticles can slow down the phase separation process.

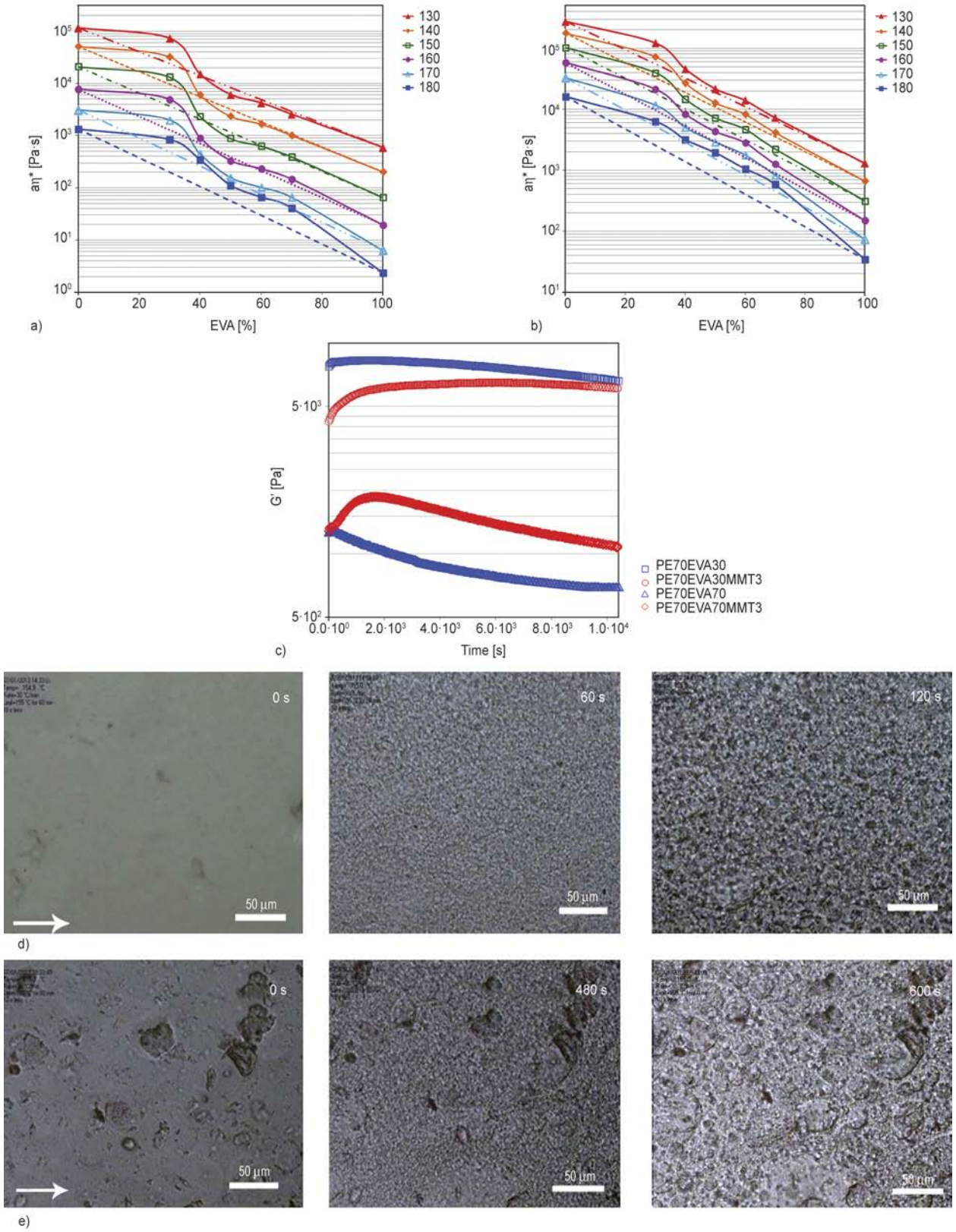

Figure 6. (a) and (b) complex viscosity (η*) of virgin blends and nanocomposites, respectively, versus EVA composition obtained via experiments (points) and calculations using mixing rule (straight lines) at different temperatures across phase boundary. Curves are shifted along the vertical-axis. (c) time evolution of G' at frequency of 1 rad/s and with 1% strain; the experiment was performed at T = 155°C and T = 152°CC for PE50EVA50 and PE50EVA50MMT3, respectively, whereas it was carried out at T = 150°C for both PE70EVA30 and PE70EVA30MMT3. (d) and (e) the optical microscopy images of: PE70EVA30 and PE70EVA30MMT3, respectively, recorded during phase separation at T = 150°C.

The restrictions on macromolecular relaxation and phase separation phenomena imposed by natural MMT improved the compatibility between the used polymers and changed the immiscible PE/EVA blends to the partially miscible ones. As a direct result of the imposed limitations, the phase-separated domains cannot thoroughly purify themselves from the molecules of the other phase during any applied cooling process. This fact can be verified by further evidence obtained using dynamic-mechanical analysis.

The observed transition temperatures of the PE and EVA phases for different samples were collected in Table 7. The β transition peak due to the relaxation of the chain branches can be hardly detected for the PE phase. Moreover, α transition peak correlated with some types of motion existed in the crystalline regions was also absent for the EVA phase. The addition of nanoparticles increased the transition temperatures to the higher values for pure polymers indicating the interaction of polymer chains with the solid surface of MMT and limited macromolecular mobility. To investigate the miscibility of these two polymers in the amorphous zones, the γ transition related to the glass transition temperature (T_g) for the obtained samples must be considered in more detail. For the virgin blends, the γ transition peak of PE and EVA phases insignificantly varied in comparison with the T_g of pure components demonstrating the immiscibility of two phases, while the presence of nanoclay altered the γ transition of polymeric constituents. Although the sample preparation method was the same, the glass transition temperatures of PE and EVA domains moved toward each other for PE70EVA30MMT3 and PE50EVA50MMT3 nanocomposites. Besides the observed miscibility enhancement, the addition of

Table 7. Different transition temperatures [°C] of PE and EVA phases in some of the obtained samples

Sample	PE phase		EVA phase	
	γ	α	γ	β
PE	–120.0	52.3	–	–
PE100MMT3	–117.9	63.8	–	–
EVA	–	–	–147.6	–20.0
EVA100MMT3	–	–	–144.6	–18.9
PE70EVA30	–120.3	51.2	–147.4	–21.0
PE70EVA30MMT3	–120.5	54.7	–143.0	–17.1
PE50EVA50	–120.7	50.2	–147.4	–21.1
PE50EVA50MMT3	–125.0	57.7	–145.9	–14.6
PE30EVA70	–120.0	–	–146.8	–21.2
PE30EVA70MMT3	–135.3	–	–135.3	–16.7

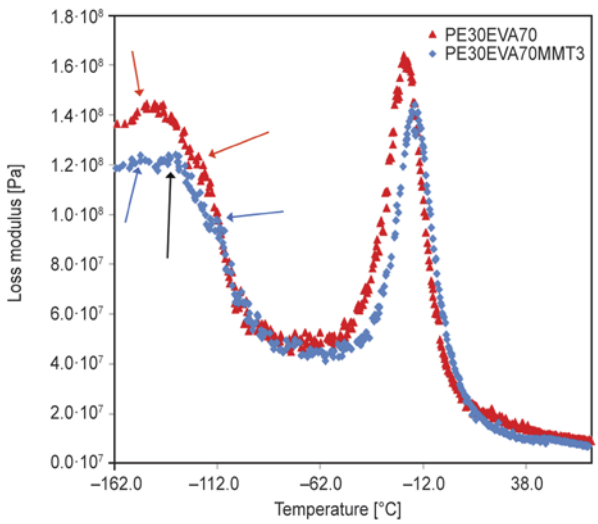

Figure 7. Loss modulus versus temperature for PE30EVA70 and PE30EVA70MMT3; the addition of MMT leads to appearance of an intermediate peak, which marks by a black arrow

nanoclay caused the appearance of a third peak, intermediate to that of the pure polymers for the EVA-rich nanocomposite (PE30EVA70MMT3). This intermediate peak marks by a black arrow in Figure 7, which show the DMA results of EVA-rich blend and the related nanocomposite. For the EVA domains in the nanocomposites, the presence of remained PE chains after phase separation and the intercalated nanoclay affect the T_g of EVA component in the same way, whereas for the PE domains, the remained EVA molecules counteract the effects of MMT and reduce the γ transition temperature of PE phase to lower values. However, the results can prove that the pristine MMT enhanced the miscibility of PE/EVA blends due to the pinning influence of nanoclay on the phase separation process.

4. Conclusions

The effects of pristine nanoclay, without any surface modification, on the biphasic morphology, phase transition diagram and phase separation kinetics of PE/EVA blends with UCST behavior were investigated.

– First of all, it was found that the compatibilization influence of natural MMT on the biphasic morphology of the virgin blends depends on the blend composition. While the addition of nanoparticles coarsens the matrix-dispersed morphology of the PE-rich blend, nanoclay plays the conventional role of compatibilizers as the morphology has become co-continuous. The observed

contradiction was explained by the state of clay localization as evaluated by microscopic observations. Different states of clay partitioning alter the dynamic asymmetry of phases; while the localization in EVA phase reduces the viscoelastic asymmetry of phases in the blends having more than 30 wt% EVA, its substantial localization in PE phase worsens the dynamic asymmetry of two components and consequently, increases the EVA domain size.

– Interfacial tension measurements indicates that the intercalated nanoclay stack can reduce the interfacial tension between the used polymers in spite of the fact that the interfacial tensions between each polymer and unmodified nanoclay are about two orders of magnitude higher than the interfacial tension of pure polymers.
– The presence of micrometer-sized agglomerated tactoids of nanoclay slightly diminishes the binodal temperatures to lower values. Although it is theoretically observed that nanofiller with γ_{AF} and $\gamma_{BF} >> \gamma_{AB}$ can enforce the macromolecules to intermix better, the segregation of nanoparticle-rich and polymer-rich regions can diminish the compatibilization effect of pristine nanoclay.
– Regardless of the blend composition, the addition of unmodified nanoclay slows down the phase separation phenomenon and enhances the miscibility of PE/EVA mixtures in the amorphous regions by comparison with the virgin blends prepared via the same melt process.

Acknowledgements

The authors would like to thank Ms. Jalilzade (Mahar Fan Abzar Co.) for the preparation of AFM images and Dr. Saeb for his helpful discussion and assistance. Also, we thank Mrs. Ghasemirad for critical reading of the manuscript.

References

[1] Manas-Zloczower I.: Mixing and compounding of polymers: Theory and practice. Hanser, Munich (2009).
[2] Zhang Q., Yang H., Fu Q.: Kinetics-controlled compatibilization of immiscible polypropylene/polystyrene blends using nano-SiO_2 particles. Polymer, **45**, 1913–1922 (2004).
DOI: 10.1016/j.polymer.2004.01.037
[3] Si M., Araki T., Ade H., Kilcoyne A. L. D., Fisher R., Sokolov J. C., Rafailovich M. H.: Compatibilizing bulk polymer blends by using organoclays. Macromolecules, **39**, 4793–4801 (2006).
DOI: 10.1021/ma060125+
[4] Behradfar A., Shojaei A., Sheikh N.: Rheological and mechanical characteristics of low density polyethylene/ethylene-vinyl acetate/organoclay nanocomposites. Polymer Engineering and Science, **50**, 1315–1325 (2010).
DOI: 10.1002/pen.21660
[5] Ray S. S., Pouliot S., Bousmina M., Utracki L. A.: Role of organically modified layered silicate as an active interfacial modifier in immiscible polystyrene/polypropylene blends. Polymer, **45**, 8403–8413 (2004).
DOI: 10.1016/j.polymer.2004.10.009
[6] Dharaiya D. P., Jana S. C.: Nanoclay-induced morphology development in chaotic mixing of immiscible polymers. Journal of Polymer Science Part B: Polymer Physics, **43**, 3638–3651 (2005).
DOI: 10.1002/polb.20657
[7] Hong J. S., Kim Y. K., Ahn K. H., Lee S. J., Kim C.: Interfacial tension reduction in PBT/PE/clay nanocomposite. Rheologica Acta, **46**, 469–478 (2007).
DOI: 10.1007/s00397-006-0123-1
[8] Elias L., Fenouillot F., Majesté J. C., Alcouffe P., Cassagnau P.: Immiscible polymer blends stabilized with nano-silica particles: Rheology and effective interfacial tension. Polymer, **49**, 4378–4385 (2008).
DOI: 10.1016/j.polymer.2008.07.018
[9] Pack S., Kashiwagi T., Cao C., Korach C. S., Lewin M., Rafailovich M. H.: Role of surface interactions in the synergizing polymer/clay flame retardant properties. Macromolecules, **43**, 5338–5351 (2010).
DOI: 10.1021/ma100669g
[10] Wu D., Lin D., Zhang J., Zhou W., Zhang M., Zhang Y., Wang D., Lin B.: Selective localization of nanofillers: Effect on morphology and crystallization of PLA/PCL blends. Macromolecular Chemistry and Physics, **212**, 613–626 (2011).
DOI: 10.1002/macp.201000579
[11] Nesterov A. E., Lipatov Y. S.: Compatibilizing effect of a filler in binary polymer mixtures. Polymer, **40**, 1347–1349 (1999).
DOI: 10.1016/S0032-3861(98)00277-8
[12] Lipatov Y. S., Nesterov A. E., Ignatova T. D., Nesterov D. A.: Effect of polymer–filler surface interactions on the phase separation in polymer blends. Polymer, **43**, 875–880 (2002).
DOI: 10.1016/S0032-3861(01)00632-2
[13] Ginzburg V. V.: Influence of nanoparticles on miscibility of polymer blends. A simple theory. Macromolecules, **38**, 2362–2367 (2005).
DOI: 10.1021/ma0482821
[14] Balazs A. C., Ginzburg V. V., Qiu F., Peng G., Jasnow D.: Multi-scale model for binary mixtures containing nanoscopic particles. Journal of Physical Chemistry B, **104**, 3411–3422 (2000).
DOI: 10.1021/jp993356+

[15] Nesterov A. E., Lipatov Y. S., Horichko V. V., Gritsenko O. T.: Filler effects on the compatibility and phase separation kinetics of poly(vinyl acetate)-poly (methyl methacrylate) mixtures. Polymer, **33**, 619–622 (1992). DOI: 10.1016/0032-3861(92)90740-N

[16] Yurekli K., Karim A., Amis E. J., Krishnamoorti R.: Influence of layered silicates on the phase-separated morphology of PS–PVME blends. Macromolecules, **36**, 7256–7267 (2003). DOI: 10.1021/ma0207551

[17] Zhang W., Lin M., Winesett A., Dhez O., Kilcoyne A. L., Ade H., Rubinstein M., Shafi K. V. P. M., Ulman A., Gersappe D., Tenne R., Rafailovich M., Sokolov J., Frisch H. L.: The use of functionalized nanoparticles as non-specific compatibilizers for polymer blends. Polymers for Advanced Technologies, **22**, 65–71 (2011). DOI: 10.1002/pat.1875

[18] Yurekli K., Karim A., Amis E. J., Krishnamoorti R.: Phase behavior of PS–PVME nanocomposites. Macromolecules, **37**, 507–515 (2004). DOI: 10.1021/ma0302098

[19] Huang Y., Jiang S., Li G., Chen D.: Effect of fillers on the phase stability of binary polymer blends: A dynamic shear rheology study. Acta Materialia, **53**, 5117–5124 (2005). DOI: 10.1016/j.actamat.2005.07.021

[20] El-Mabrouk K., Bousmina M.: Phase separation of polystyrene/poly(vinylmethylether)/organoclay nanocomposites. Journal of Nanoscience and Nanotechnology, **6**, 472–482 (2006). DOI: 10.1166/jnn.2006.093

[21] El-Mabrouk K., Vandreuil S., Zeghloul A., Bousmina M.: Effect of shear on phase-separation in polystyrene/poly(vinyl methyl ether)/organoclay nanocomposites. Journal of Nanoscience and Nanotechnology, **8**, 1895–1900 (2008). DOI: 10.1166/jnn.2008.0191895

[22] Gharachorlou A., Goharpey F.: Rheologically determined phase behavior of LCST blends in the presence of spherical nanoparticles. Macromolecules, **41**, 3276–3283 (2008). DOI: 10.1021/ma7020985

[23] Gao J., Huang C., Wang N., Yu W., Zhou C.: Phase separation of poly (methyl methacrylate)/poly (styrene-co-acrylonitrile) blends in the presence of silica nanoparticles. Polymer, **53**, 1772–1782 (2012). DOI: 10.1016/j.polymer.2012.02.027

[24] Carriere C. J., Cohen A., Arends C. B.: Estimation of interfacial tension using shape evolution of short fibers. Journal of Rheology, **33**, 681–689 (1989). DOI: 10.1122/1.550033

[25] Cohen A., Carriere C. J.: Analysis of a retraction mechanism for imbedded polymeric fibers. Rheologica Acta, **28**, 223–232 (1989). DOI: 10.1007/BF01332854

[26] Yasuda K.: Investigation of the analogies between viscometric and linear viscoelastic properties of polystyrene fluids. PhD Thesis, Massachusetts Institute of Technology (1979).

[27] Steinmann S., Gronski W., Friedrich C.: Influence of selective filling on rheological properties and phase inversion of two-phase polymer blends. Polymer, **43**, 4467–4477 (2002). DOI: 10.1016/S0032-3861(02)00271-9

[28] Raghavan D., Gu X., Nguyen T., VanLandingham M., Karim A.: Mapping polymer heterogeneity using atomic force microscopy phase imaging and nanoscale indentation. Macromolecules, **33**, 2573–2583 (2002). DOI: 10.1021/ma991206r

[29] Hemati F., Garmabi H.: Compatibilised LDPE/LLDPE/nanoclay nanocomposites: I. Structural, mechanical, and thermal properties. The Canadian Journal of Chemical Engineering, **89**, 187–196 (2011). DOI: 10.1002/cjce.20377

[30] Tadmor R.: Line energy and the relation between advancing, receding, and young contact angles. Langmuir, **20**, 7659–7664 (2004). DOI: 10.1021/la049410h

[31] Ginzburg V. V., Weinhold J. D., Jog P. K., Srivastava R.: Thermodynamics of polymer–clay nanocomposites revisited: Compressible self-consistent field theory modeling of melt-intercalated organoclays. Macromolecules, **42**, 9089–9095 (2009). DOI: 10.1021/ma9017263

[32] Puyvelde P. V., Velankar S., Moldenaers P.: Rheology and morphology of compatibilized polymer blends. Current Opinion in Colloid and Interface Science, **6**, 457–463 (2001). DOI: 10.1016/S1359-0294(01)00113-3

[33] Wu S.: Formation of dispersed phase in incompatible polymer blends: Interfacial and rheological effects. Polymer Engineering and Science, **27**, 335–343 (1987). DOI: 10.1002/pen.760270506

[34] He G., Ginzburg V. V., Balazs A. C.: Determining the phase behavior of nanoparticle-filled binary blends. Journal of Polymer Science Part B: Polymer Physics, **44**, 2389–2403 (2006). DOI: 10.1002/polb.20887

eXPRESS Polymer Letters Vol.7, No.12 (2013) 1012–1019
Available online at www.expresspolymlett.com
DOI: 10.3144/expresspolymlett.2013.99

Effect of an organoclay on the reaction-induced phase-separation in a dynamically asymmetric epoxy/PCL system

*J. Rotrekl, A. Sikora, L. Kaprálková, J. Dybal, I. Kelnar**

Institute of Macromolecular Chemistry, Academy of Sciences of the Czech Republic, Heyrovsky Sq. 2, 162 06 Prague, Czech Republic

Received 13 June 2013; accepted in revised form 23 August 2013

Abstract. The addition of layered silicates can significantly affect the phase behaviour of both immiscible thermoplastic blends and partially miscible thermoset systems that undergo reaction-induced phase separation (RIPS) during curing. This study focuses on the phase behaviour of polycaprolactone (PCL)/epoxy in the presence of organically modified montmorillonite (oMMT). Due to the high dynamic asymmetry caused by the differences in the molecular weights and viscosities of the PCL and the uncured epoxy, the critical point is localised at low PCL concentrations, as indicated by the pseudophase diagram. The addition of oMMT to the system led to the marked shift of the critical point towards higher concentrations of PCL, with an increase in the oMMT content occurring as a consequence of the preferential localisation of the clay in the epoxy phase, making this phase more dynamically slow. Significant changes in morphology, including phase inversion of the PCL/epoxy systems caused by the presence of oMMT, were recorded for PCL concentrations ranging from 10 to 30%.

Keywords: *nanocomposites, epoxy, microstructure, reaction induced phase separation*

1. Introduction

Epoxies are often used in combination with liquid rubbers or thermoplastic polymers [1–4] to reduce their brittleness. An effective two phase structure [5] can be obtained by the reaction-induced phase separation (RIPS) of the initially dissolved polymeric modifiers. Recently it was found that behaviour of multicomponent polymer systems can be significantly altered by using nanofillers. The presence of nanofillers in polymeric mixtures can affect the thermodynamics of its phase behaviour, the kinetics of phase separation, and also the morphology formed in the two-phase region [6–14]. Bousmina et al [15, 16] found in PS/PVME blend that organoclay changed the mechanism of phase separation from spinodal decomposition to nucleation and growth and affected the final morphology obtained after phase segregation. Organoclay represents an efficient active interfacial agent that enlarges the miscibility window and reduces the size of PS droplets. Theoretical study of Balazs *et al*. [17] showed that preferential wetting of nanofiller by one of the polymers may slow down the kinetics of spinodal decomposition. As a result, nanoparticle addition to binary mixtures could decrease the rate of domain growth and leads to a pinning effect on interface motions. The fact that the addition of nanoparticles could diminish the diffusion of polymeric chains and retard the phase separation was confirmed experimentally [10, 12]. The effect of the nanofiller on the phase behaviour can be controlled by altering the polymer clay affinity using various clay modifications, leading to the preferential wetting of one component of the blend [18].

*Corresponding author, e-mail: kelnar@imc.cas.cz

In the case of partially miscible thermoset systems, the clay influences the RIPS not only through a nucleating effect [19] combined with hindering the mass transport of the system but also by affecting the cure kinetics [20, 21]. The final phase separated morphology of the thermoplastic/epoxy mixture is also determined by its composition and cure temperature. The classic example of a thermoplastic-thermosetting mixture is an epoxy alloy, in which the toughness has been modified through blending with high performance thermoplastics, such as poly (ether imide) (PEI), poly(ether sulphone) (PES), poly (phenylene ether) (PPE), polysulphone, poly(ether ketone) (PEK) and others. It has been reported that significant increase in toughness is [22] achieved only when the thermoplastics form a continuous phase in the mixture. Due to the importance of RIPS in determining the structure type and dimensions, including the composition of the respective phases, efforts to control the phase behaviour and morphology have attracted considerable interest. Curing of the epoxy-monomer containing a dissolved polymeric modifier leads to phase separation. This occurs depending on the composition of the reaction mixtures, either by a spinodal (SD) or a nucleation and growth (NG) mechanism. The resulting morphology is determined by the thermodynamic conditions of the phase separation [23] and by the viscoelastic characteristics of the separating phases [24–27]. These factors are particularly important in thermoplastic/epoxy mixtures that exhibit significant dynamical asymmetry due to large differences in the molecular weights and glass transition temperatures (T_g) of the two components [27].

Studies of the mechanisms of phase separation have revealed that the majority of polymer blends do not meet the implicit assumptions contained in the model for the phase separation of low-molecular weight liquid mixtures [25], which states that the viscoelastic properties of the components are similar to each other (*i.e.*, symmetrical). As a general rule, the viscoelastic properties of the constituent polymer blends vary significantly due to differences in the size of the molecules and their flexibility. These systems are referred to as dynamically asymmetric, and their phase separation is considered viscoelastic phase-separation (VPS) [25]. It is important to note that the initiation of phase separation crucially depends on thermodynamic conditions. The viscoelastic properties of the components influence the phase separation mechanism once the system reaches thermodynamic instability. Tanaka's comprehensive model analysing the phase separation of binary polymeric mixtures [25] has defined the dynamic area under binodal in which the separation mechanism is controlled by bulk and shear stress. This regime is defined by the dynamic spinodal curve, in which the maximum temperature is lower than the upper critical solution temperature. In the concentration range in which the ratio of the components is close to 1, phase inversion occurs.

As a result, the epoxy-rich phase tends to interfere even at the very early stages of SD due to its low viscosity and/or poor fluid strength. The minority phase, namely the thermoplastic-rich phase, is continuous due to its strengthened viscoelasticity during phase separation.

In our recent work [28, 29] we showed that nanoclay can significantly affect the behaviour of epoxy/PCL systems containing 5–30% PCL. The radical morphological transformations consisting of phase inversion for 20% PCL content due to increasing clay content led to a substantial improvement of the mechanical behaviour. The main reason for this phenomenon was a shift in the dynamic asymmetry caused by the localization of clay inside the epoxy phase, supporting its continuity. The results indicate the potential of clay to tailor the structure and properties of RIPS systems with significant dynamic asymmetry.

The aim of this study was to evaluate the influence of nanofillers on the phase separation behaviour represented by pseudophase diagrams in the whole concentration range of epoxy/PCL system and coresponding final morphology of nanocomposites.

2. Experimental

2.1. Materials

Organically modified montmorillonite Cloisite C30B (C30) with methyl tallow bis(2-hydroxyethyl) quaternary ammonium chloride was obtained from Southern Clay Products, Inc. (Gonzales, Texas, USA). Polycaprolactone (PCL) m.w. 40 000 was obtained from Perstorp (Perstorp, Sweden). The diglycidyl ether of bisphenol A (DGEBA)-based epoxy resin, Epilox A19-02 (epoxy equivalent weight 185–200 g, m.w. 396 g/mol), was purchased from Leuna-Harze GmbH (Leuna, Germany), and the

amine hardener diaminodiphenyl sulphone (DDS) was purchased from Aldrich (St. Louis, Missouri, USA).

2.2. Preparation of blends and related nanocomposites

The mixtures of epoxy, curing agent, PCL and oMMT were prepared by dissolving the components in tetrahydrofuran for 12 hours. The concentration of solution prepared was approximately 10%. The solvent was removed under vacuum at room temperature for 48 hours. Thin layer samples for optical microscopy were prepared by insertion of small piece of material between two round glass plates (12 mm in diameter) and subsequent compression at 120°C to achieve thin layer (~50 μm).

2.3. Cloud point evaluation and morphological observations

The cloud point time was evaluated by the *in situ* optical microscopy observation of a thin layer (~50 μm) of sample sandwiched between two glass slides at 170°C. A Linkam hot stage was used to heat the samples. *In situ* optical microscopy was also used for morphological observations. Pseudophase diagrams were constructed using conversion at the time of cloud point evaluated by FTIR measurement of samples heated at 170°C and quenched after reaching of cloud point time. Due to extremely slow curing rate of DDS at ambient temperature, the error can be neglected.

2.4. Chemorheological measurements

Chemorheological experiments were conducted using an ARES apparatus (Rheometric Scientific, Piscataway, NJ). The evolution of the dynamic viscosity and tan δ during curing at 170°C were conducted in the parallel-plate geometry using an oscillatory shear deformation at a frequency of 6.28 rad/s (1 Hz) (estimated variation coefficient of viscosity at gel point is 5%). Gelation time evaluation was based on tan δ, since gelation occurs at approximately tan δ = 1, where loss modulus is equal to storage modulus [30].

3. Results and discussion

3.1. Effect of clay on the curing reaction

Chemorheological measurements were performed to evaluate the effect of clay on the viscosity and cure kinetics of the composites. Figure 1 illustrates

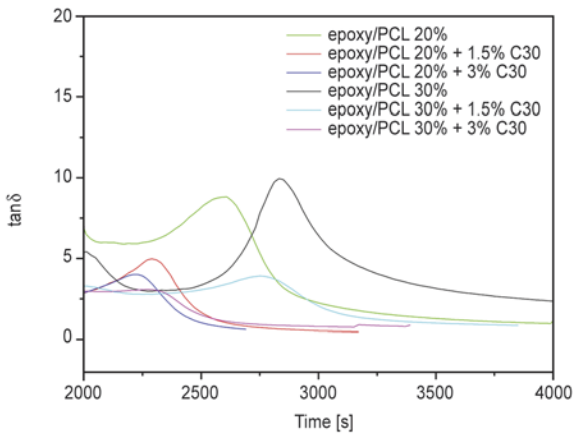

Figure 1. The evolution of tan δ with curing time, as evaluated by chemorheology

the significant shortening of the gelation time (tan δ = 1 [30]) and corresponding increase in reaction rate with increasing clay concentration, which has been observed previously elsewhere [20, 21, 31, 32]. The increased reaction rate can be attributed to the catalytic activity of the ternary ammonium salt contained in the organic clay modifier on the epoxy amine reaction [33]. This effect is more pronounced with increasing oMMT content [31, 32]. The quarternary ammonium salt also initiates the self-polymerisation of epoxy groups at elevated temperatures [34], which may contribute to the increase in the epoxy conversion rate. This hypothesis was confirmed by the 10% conversion observed by IR measurement of the blank sample, which contained the epoxy resin with added clay but no curing agent. However, there is no evidence that the PCL can participate in the reaction with epoxy, as demonstrated by the IR-based evaluation of the conversion of samples composed of epoxy and PCL only. Therefore, the PCL only affects the reaction rate through its contribution to the dilution of the reaction components, which results in prolonged reaction times. Figure 1 also reveals peaks in tan δ corresponding to the onset of phase separation [35]. These peaks are in general agreement with the cloud point determined by *in situ* optical microscopy.

Chemorheological measurements provided further evidence of the effect of clay on the viscosity (Figure 2). The slight increase of viscosity at 2000 s for sample without oMMT coresponds obviously with phase separation [36]. The absence of this fluctuation for the sample containing oMMT most probably indicates the affecting of phase separation process by relative high content (3%) of oMMT.

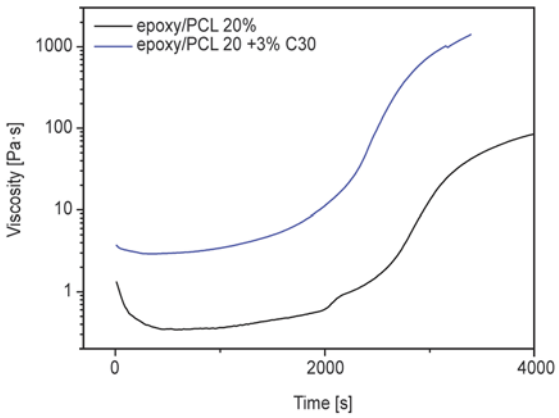

Figure 2. The evolution of viscosity with curing time, as evaluated by chemorheology

3.2. Effect of clay on pseudophase diagrams

The phase diagrams of the PCL/epoxy systems (Figures 3 and 4) reveal a minimum (critical point, CP) located at approximately 10% PCL content. This behaviour arises due to the dynamic asymmetry between the components due to their differences in molecular weight; in cases in which the two components exhibit similar molar masses, the critical point is CP = 0.5 and the phase diagram is symmetrical. The addition of oMMT led to a shift of the CP to higher concentrations of PCL. Due to the preferential concentration of the nanofillers with a high molar mass in the epoxy phase (documented by TEM in ref. [28], not shown), an increase in the apparent molar mass of the epoxy phase and a change in the effective (medium) interaction parameter occurred. As a result, the CP of the phase diagram shifted with increasing filler content to higher PCL content, in agreement with the Ginzburg model calculations [37].

From both the time- and conversion-based phase diagrams in Figures 3 and 4, it is evident that the time needed to achieve phase separation at a given curing temperature at high PCL concentrations decreased sharply with increasing filler content and that the conversion approached 100%. This behaviour was influenced by several factors, including curing temperature. By temperature jump from room temperature to the curing temperature the studied mixture, gets into different depths of phase unstable area based on its composition. At low concentrations of PCL in the vicinity of the CP, penetration to a completely unstable spinodal region takes place, leading to a rapid separation of the two phases throughout the sample volume. This behaviour suggests that at low PCL concentrations a fast decay phase and brief turbidity occur, which are only slightly dependent on the filler content. At concentrations above 50% PCL, the depth of penetration into the unstable area of the phase diagram is lower and the system is located in the region between the spinodal and binodal curves, where phase-separation via nucleation and growth (NG) takes place. Development of the separated phase occurs in sepa-

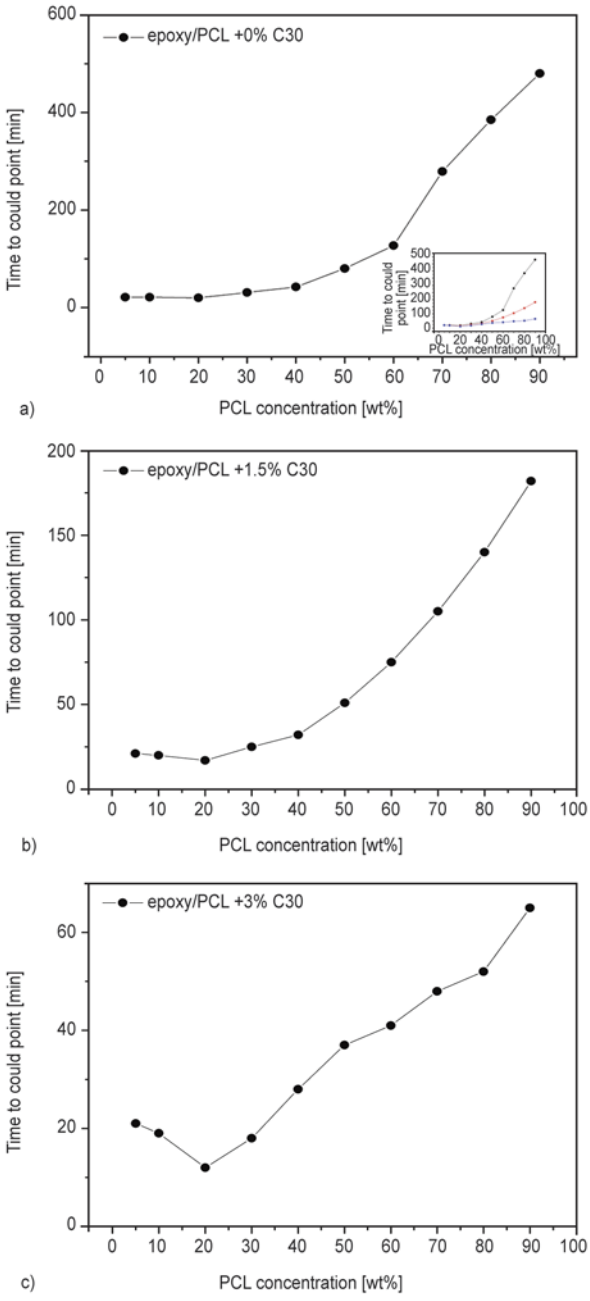

Figure 3. The effect of clay on the phase diagram of the time to cloud point vs weight fraction of PCL, (a) 0% C30, (b) 1.5% C30, (c) 3% C30. Note significant differences in time to cloud point as indicated in the inlet picture.

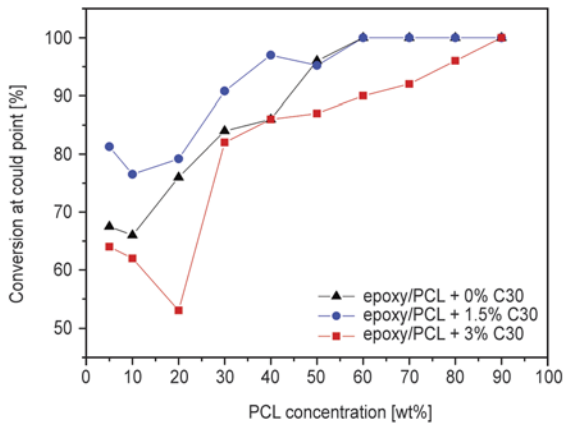

Figure 4. The effect of clay on the phase diagram of conversion at cloud point vs weight fraction of PCL

rate random domains relatively slowly. The time required for the emergence of an observable phase is extended, and as a result, the conversion detected during the initial phase separation is remarkably high. The decreasing time necessary to achieve phase separation with increasing filler content is in agreement with the observation that nanofillers accelerate epoxy curing. However, nano-sheets of MMT substantially restrict the diffusion of the system components, resulting in lower conversions at the threshold of phase separation, as depicted in the comparison of the phase diagrams in Figure 4.

This behaviour is in agreement with previously published data. When studying the phase behaviour of aqueous solutions of poly(vinylmethyl ether) (PVME), Tanaka observed unexpected morphological changes during phase separation at temperatures above the lower critical solution temperature (LCST) [24]. The resulting structure differed from the bicontinual phase structure with a subsequent phase separation(s) into domains, as described in the classical model of spinodal disintegration (SP) or the nucleation and growth mechanism (NG). Similar morphological changes have been observed in a wide variety of polymer blends, including inversion stages, which cannot be explained simply using the classical SD or NG mechanism [26, 38].

From Figure 5, it is apparent that the addition of 3% filler to the mixtures containing 15 and 20% PCL led to phase inversion; the continuous PCL structure separated to form a domain structure. This can be explained by the influence of the filler on the effective interaction parameter and reaction rate. Both of these parameters shift the critical temperature (*e.g.*, upper critical solution temperature to higher temperatures and higher concentrations of PCL; LCST to lower temperatures and higher concentrations of PCL). The dynamic spinodal curve shifted in the same direction as the areas of phase inversion. The addition of fillers caused the mixture to shift to this region of the phase diagram earlier than the binary mixture of PCL with epoxy. The addition of nanofillers also affected the viscoelastic behaviour of the epoxy phase, in which they preferentially concentrate. This altered the dynamic asymmetry of the mixture and extended the area of the inverted phases.

3.3. Morphology

The images captured using *in-situ* optical microscopy revealed a change in the morphology of the cured samples upon the addition of the nanoclay. At 15% and 20% PCL content, the addition of 3% clay transformed the original structure, consisting of rough bi-continuous domains, into a structure comprising an epoxy matrix and fine PCL inclusions. The localisation of PCL was confirmed by the observation of PCL spherulites under polarised light. At higher PCL concentrations (over 20%), the original spherical domains of the epoxy were converted to larger, irregular 'islands' as a consequence of the improved continuity of the epoxy and the change in asymmetry induced by the clay. The morphology may have also been affected by the change in reaction kinetics induced by the clay (Figures 1 and 2), which can lead to changes in the time interval (between cloud and gel point) available for phase separation [39]. The reduced time available for the development of the phase during curing was also confirmed by chemorheological measurements (Figure 1), which revealed a peak in tan δ corresponding to the initiation of phase separation [40] that was closer to the gelation at higher clay concentrations. Furthermore, the T_g values demonstrate that, contrary to the increase observed in the neat epoxy nanocomposite, the T_g decreased with increasing clay content in the epoxy/PCL [28]. This behaviour can be attributed to the incomplete phase separation caused by the accelerated curing and reduced diffusion (pinning effect) induced by the clay, which resulted in a higher concentration of 'dissolved' PCL in the epoxy rich phase. Thus, the phase separation freezes at an earlier stage in the presence of the clay.

The optical microscopy observations of thin layers of the material were in good agreement with the

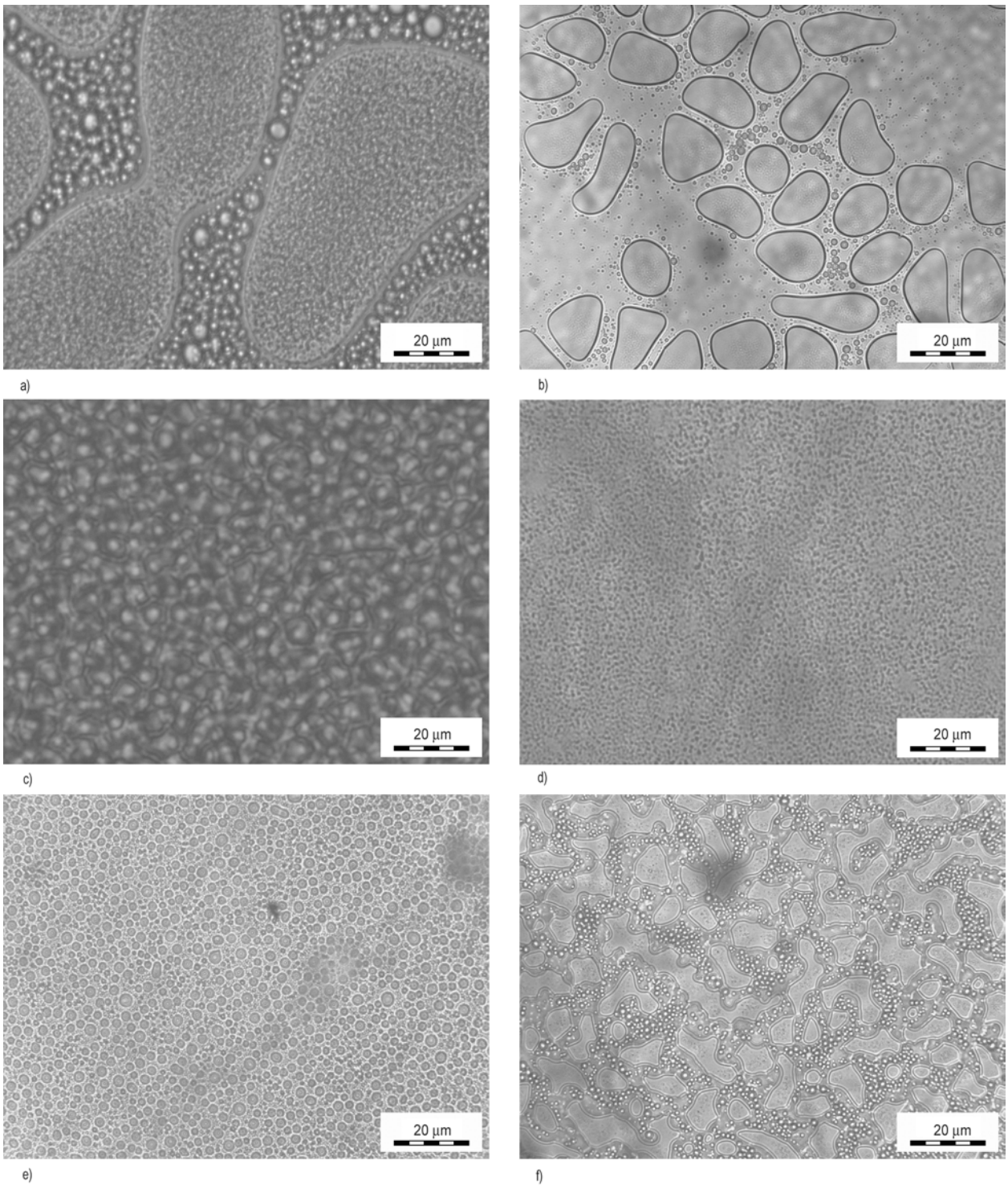

Figure 5. Morphology of thin layer samples observed by optical microscopy (a) 5% PCL, (b) 20% PCL, (c) 30% PCL (d) 15% PCL + C30B, (e) 20% PCL + C30B, (f) 30% PCL + C30B

SEM observations [28] of bulk samples, which displayed phase inversion from a continuous PCL-rich phase with large epoxy globules to an epoxy-rich matrix with fine PCL inclusions with increasing content of clay.

4. Conclusions

The pseudophase diagrams of dynamically asymmetric PCL/epoxy systems with various clay contents demonstrated the marked ability of oMMT nanoplatelets to influence LCST phase separation

behaviour. This is reflected most notably in the shift of the critical point towards higher PCL concentrations. Such behaviour can be attributed to the preferential localisation of the clay in the epoxy-rich phase, which slows its dynamics and results in a significant transformation in the morphology of cured blends at PCL concentrations near and above the critical concentration of the neat blend, including inversion from a PCL-rich matrix with globules of epoxy to an epoxy-rich matrix with fine PCL inclusions. The strong potential of nanofillers to alter the morphology of cured blends with a fixed content of polymeric modifier can be used to tailor the structures of multiphase thermosets.

Acknowledgements

This work was supported by the Grant Agency of the Academy of Sciences of the Czech Republic (project No IAA200500904)

References

[1] Francis B., Ramaswamy R., Rao V. L., Thomas S.: Toughening of diglycidyl ether of bisphenol-A epoxy resin using poly (ether ether ketone) with pendent ditert-butyl groups. International Journal of Polymeric Materials, **55**, 681–702 (2006).
DOI: 10.1080/00914030500323326

[2] Mimura K., Ito H., Fujioka H.: Improvement of thermal and mechanical properties by control of morphologies in PES-modified epoxy resins. Polymer, **41**, 4451–4459 (2000).
DOI: 10.1016/S0032-3861(99)00700-4

[3] Bucknall C. B., Gilbert A. H.: Toughening tetrafunctional epoxy resins using polyetherimide. Polymer, **30**, 213–217 (1989).
DOI: 10.1016/0032-3861(89)90107-9

[4] Hourston D. J., Lane J. M.: The toughening of epoxy resins with thermoplastics: 1. Trifunctional epoxy resin-polyetherimide blends. Polymer, **33**, 1379–1383 (1992).
DOI: 10.1016/0032-3861(92)90110-I

[5] Pascault J-P., Sautereau H., Williams R. J. J., Verdu J.: Thermosetting polymers. Marcel Dekker, New York (2002).
DOI: 10.1201/9780203908402

[6] Tanaka H., Lovinger A. J., Davis D. D.: Pattern evolution caused by dynamic coupling between wetting and phase separation in binary liquid mixture containing glass particles. Physical Review Letters, **72**, 2581–2584 (1994).
DOI: 10.1103/PhysRevLett.72.2581

[7] Ginzburg V. V., Qiu F., Paniconi M., Peng G., Jasnow D., Balazs A. C.: Simulation of hard particles in a phase-separating binary mixture. Physical Review Letters, **82**, 4026–4029 (1999).
DOI: 10.1103/PhysRevLett.82.4026

[8] Suppa D., Kuksenok O., Balazs A. C., Yeomans J. M.: Phase separation of a binary fluid in the presence of immobile particles: A lattice Boltzmann approach. Journal of Chemical Physics, **116**, 6305–6310 (2002).
DOI: 10.1063/1.1460863

[9] Nesterov A. E., Lipatov Y. S., Horichko V. S., Ignatova T. D.: Effect of filler on kinetics and energy of activation of phase separation in poly(methyl methacrylate)/poly(vinyl acetate) blend. Macromolecular Chemistry and Physics, **199**, 2609–2612 (1998).
DOI: 10.1002/(SICI)1521-3935(19981101)199:11<2609::AID-MACP2609>3.0.CO;2-Z

[10] Nesterov A. E., Lipatov Y. S., Horichko V. V., Gritsenko O. T.: Filler effects on the compatibility and phase separation kinetics of poly(vinyl acetate)-poly (methyl methacrylate) mixtures. Polymer, **33**, 619–622 (1992).
DOI: 10.1016/0032-3861(92)90740-N

[11] Lipatov Y. S., Nesterov A. E., Ignatova T. D., Nesterov D. A.: Effect of polymer–filler surface interactions on the phase separation in polymer blends. Polymer, **43**, 875-880 (2002).
DOI: 10.1016/S0032-3861(01)00632-2

[12] Yurekli K., Karim A., Amis E. J., Krishnamoorti R.: Influence of layered silicates on the phase-separated morphology of PS–PVME blends. Macromolecules, **36**, 7256–7267 (2003).
DOI: 10.1021/ma0207551

[13] Kelnar I., Rotrekl J., Kotek J., Kaprálková L.: Effect of montmorillonite modification on the behaviour of polyamide/polystyrene blends. Polymer International, **57**, 1281–1286 (2008).
DOI: 10.1002/pi.2475

[14] Kelnar I., Rotrekl J., Kotek J., Kaprálková L., Hromádková J.: Effect of montmorillonite on structure and properties of nanocomposite with PA6/PS/elastomer matrix. European Polymer Journal, **45**, 2760–2766 (2009).
DOI: 10.1016/j.eurpolymj.2009.06.024

[15] Mabrouk K. E., Bousmina M.: Phase separation of polystyrene/poly(vinylmethylether)/organoclay nanocomposites. Journal of Nanoscience and Nanotechnology, **6**, 472–482 (2006).
DOI: 10.1166/jnn.2006.093

[16] El-Mabrouk K., Vandreuil S., Zeghloul A., Bousmina M.: Effect of shear on phase-separation in polystyrene/poly(vinyl methyl ether)/organoclay nanocomposites. Journal of Nanoscience and Nanotechnology, **8**, 1895–1900 (2008).
DOI: 10.1166/jnn.2008.0191895

[17] Balazs A. C., Ginzburg V. V., Qiu F., Peng G., Jasnow D.: Multi-scale model for binary mixtures containing nanoscopic particles. Journal of Physical Chemistry B, **104**, 3411–3422 (2000).
DOI: 10.1021/jp993356+

[18] Araki T., Tanaka H.: Dynamic depletion attraction between colloids suspended in a phase-separating binary liquid mixture. Journal of Physics: Condensed Matter, **20**, 072101/1–072101/6 (2008).
DOI: 10.1088/0953-8984/20/7/072101

[19] Lee S-H., Kim M-J., Park H.: Characteristics of cotton fabrics treated with epichlorohydrin and chitosan. Journal of Applied Polymer Science, **117**, 623–628 (2010).
DOI: 10.1002/app.31351

[20] Bao S., Shen S., Liang G., Zhai H., Xu W., He P.: Curing behavior of epoxy resin/tung oil anhydride exfoliated nanocomposite by differential scanning calorimetry. Journal of Applied Polymer Science, **92**, 3822–3829 (2004).
DOI: 10.1002/app.20398

[21] Kelnar I., Rotrekl J., Kaprálková L., Hromádková J., Strachota A.: Effect of amine-terminated butadiene-acrylonitrile/clay combinations on the structure and properties of epoxy nanocomposites. Journal of Applied Polymer Science, **125**, 3477–3483 (2012).
DOI: 10.1002/app.36696

[22] Hodgkin J. H., Simon G. P., Varley R. J.: Thermoplastic toughening of epoxy resins: A critical review. Polymers for Advanced Technologies, **9**, 3–30 (1998).
DOI: 10.1002/(SICI)1099-1581(199801)9:1<3::AID-PAT727>3.0.CO;2-I

[23] Inoue T.: Reaction-induced phase decomposition in polymer blends. Progress in Polymer Science, **20**, 119–153 (1995).
DOI: 10.1016/0079-6700(94)00032-W

[24] Tanaka H.: Appearance of a moving droplet phase and unusual networklike or spongelike patterns in a phase-separating polymer solution with a double-well-shaped phase diagram. Macromolecules, **25**, 6377–6380 (1992).
DOI: 10.1021/ma00049a042

[25] Araki T., Tanaka H.: Three-dimensional numerical simulations of viscoelastic phase separation: Morphological characteristics. Macromolecules, **34**, 1953–1963 (2001).
DOI: 10.1021/ma001569n

[26] Ishii Y., Ryan A. J.: Processing of poly(2,6-dimethyl-1,4-phenylene ether) with epoxy resin. 1. Reaction-induced phase separation. Macromolecules, **33**, 158–166 (2000).
DOI: 10.1021/ma990837i

[27] Cicala G., Mamo A., Recca G., Restuccia C. L.: Study on epoxy/thermoplastic blends based on the addition of a novel aromatic block copolymer. Polymer Engineering and Science, **47**, 2027–2033 (2007).
DOI: 10.1002/pen.20915

[28] Rotrekl J., Matějka L., Kaprálkova L., Zhigunov A., Hromádková J., Kelnar I.: Epoxy/PCL nanocomposites: Effect of layered silicate on structure and behavior. Express Polymer Letters, **6**, 975–986 (2012).
DOI: 10.3144/expresspolymlett.2012.103

[29] Kratochvíl J., Rotrekl J., Kaprálková L., Hromádková J., Kelnar I.: Epoxy/poly(ε-caprolactone) nanocomposites: Effect of transformations of structure on crystallization. Journal of Applied Polymer Science, in press, (2013).
DOI: 10.1002/app.39536

[30] Chambon F., Winter H. H.: Linear viscoelasticity at the gel point of a crosslinking PDMS with imbalanced stoichiometry. Journal of Rheology, **31**, 683–697 (1987).
DOI: 10.1122/1.549955

[31] Lan T., Karivatna P. D., Pinnavaia T. J.: Mechanism of clay tactoid exfoliation in epoxy-clay nanocomposites. Chemistry of Materials, **7**, 2144–2150 (1995).
DOI: 10.1021/cm00059a023

[32] Le Pluart L., Duchet J., Sautereau H.: Epoxy/montmorillonite nanocomposites: Influence of organophilic treatment on reactivity, morphology and fracture properties. Polymer, **46**, 12267–12278 (2005).
DOI: 10.1016/j.polymer.2005.10.089

[33] Ton-That M-T., Ngo T-D., Ding P., Fang G., Cole K. C., Hoa S. V.: Epoxy nanocomposites: Analysis and kinetics of cure. Polymer Engineering and Science, **44**, 1132–1141 (2004).
DOI: 10.1002/pen.20106

[34] Lan T., Kaviratna P. D., Pinnavaia T. J.: Epoxy self-polymerization in smectite clays. Journal of Physics and Chemistry of Solids, **57**, 1005–1010 (1996).
DOI: 10.1016/0022-3697(95)00388-6

[35] Ishii Y., Ryan A. J.: Processing of poly(2,6-dimethyl-1,4-phenylene ether) with epoxy resin. 2. Gelation mechanism. Macromolecules, **33**, 167–176 (2000).
DOI: 10.1021/ma990838a

[36] Cicala G., La Spina R., Recca A., Sturiale S.: Influence of copolymer's end groups and molecular weights on the rheological and thermomechanical properties of blends of novel thermoplastic copolymers and epoxy resins. Journal of Applied Polymer Science, **101**, 250–257 (2006)
DOI: 10.1002/app.23275

[37] Ginzburg V. V.: Influence of nanoparticles on miscibility of polymer blends. A simple theory. Macromolecules, **38**, 2362–2367 (2005).
DOI: 10.1021/ma0482821

[38] Shi W., Yang J., Liu W., Zhang L., Han C. C.: Anomalous phase separation dynamics under asymmetric viscoelastic effect: Where fluidic and elastic properties meet. Macromolecules, **46**, 2516–2520 (2013).
DOI: 10.1021/ma400032w

[39] Kelnar I., Rotrekl J., Kapralková L., Hromádková J.: Effect of poly(oxyalkylene)amines on structure and properties of epoxide nanocomposites. Journal of Applied Polymer Science, **125**, 2755–2763 (2012).
DOI: 10.1002/app.36604

[40] Mezzenga R., Luciani A., Månson J-A. E.: Phase separation and gelation of epoxy resin/hyperbranched polymer blends. Polymer Engineering and Science, **42**, 249–257 (2002).
DOI: 10.1002/pen.10945

eXPRESS Polymer Letters Vol.7, No.12 (2013) 1020–1029
Available online at www.expresspolymlett.com
DOI: 10.3144/expresspolymlett.2013.100

Thermo-responsive, UV-active poly(phenyl acrylate)-*b*-poly(diethyl acrylamide) block copolymers

*Z. J. Wang, B. H. Lessard, M. Marić**

McGill University, Department of Chemical Engineering, McGill Institute of Advanced Materials (MIAM), Centre for Self-Assembled Chemical Structures (CSACS), 3610 University Street, H3A 2B2 Montréal, Québec, Canada

Received 7 June 2013; accepted in revised form 23 August 2013

Abstract. The homopolymerization of phenyl acrylate (PA) was investigated for the first time by nitroxide mediated polymerization (NMP) with the succinimidyl form of the SG1-based unimolecular initiator 2-[*N*-*tert*-butyl-2,2-(dimethylpropyl)-aminooxy]propionic acid (BlocBuilder MA). The control of PPA homopolymerization was improved by the use of 15 mol% additional free nitroxide SG1 ([tert-butyl[1-(diethoxyphosphoryl)-2,2-dimethylpropyl]amino]oxidanyl) and dispersities, M_w/M_n, of around 1.2 were achieved. A PPA homopolymer was then successfully chain-extended with diethyl acrylamide (DEAAm) to form a block copolymer of PPA-*b*-PDEAAm where the PDEAAm segment is thermo-responsive, while the PPA block is potentially UV-active. The thermo-responsive behavior of the block copolymer in 0.5 wt% aqueous solution was studied by UV-Vis spectrometry and dynamic light scattering (DLS), indicating cloud point temperatures of 26–30°C, close to that reported for PDEAAm homopolymers.

Keywords: *smart polymers, UV-active polymers, nitroxide mediated polymerization (NMP), phenyl acrylate*

1. Introduction

A great deal of interest has been focused on the inclusion of photosensitive chromophores into thermo-responsive polymers, which can change the behavior of the polymer when exposed to light [1–5]. Poly(phenyl acrylate) (PPA) homopolymers have been shown to undergo photo-Fries rearrangements which can significantly modify the polymer solubility, making it an ideal candidate for photosensitive applications such as for photolithography and for light-sensitive 'smart' block copolymers when coupled to a stimuli-responsive segment (Figure 1) [6, 7]. Photo-Fries rearrangements have been utilized in UV-induced micro- or nano-lithography and nano-scale patterning [8, 9]. Despite its potentially interesting properties, particularly if it was to be incorporated into block copolymers, phenyl acrylate (PA) has only been homo/copolymerized by conventional free-radical polymerization [9, 10] and ionic polymerization [11] and not in the open literature by any reversible-deactivation radical polymerization (RDRP) technique such as nitroxide mediated polymerization (NMP) [12–16], atom transfer radical polymerization (ATRP) [17–19] and reversible addition fragmentation transfer polymerization (RAFT) [20, 21]. There has been some mention of polymerizing PA in the patent literature however. Multi-walled carbon nanotubes were dispersed using block copolymers, preferentially using poly(acrylic acid)-block-poly(methyl methacrylate) using NMP [22] for which PA could be used in the hydrophobic block [23] but no kinetic details were presented. Glaser described an ATRP process for which PA could be used as a possible monomer but again no specific

*Corresponding author, e-mail: milan.maric@mcgill.ca

examples of PA kinetics were provided [24]. To control the functionality of the block copolymer, it is imperative to exert a high degree of control of the molecular weight and composition of the block copolymer; therefore making an RDRP technique highly attractive, particularly since it avoids the stringent requirements for typical, traditional living polymerizations.

The goal of this manuscript is thus to examine the NMP of PA using the so-called SG1-based nitroxide, BlocBuilder-MA, as the unimolecular initiator, which was modified to a succinimidyl form (to be termed NHS-BlocBuilder herein). The succinimidyl group could be used to couple with amines [25, 26], a reaction often used in peptide coupling [27]. Further, NHS-BlocBuilder dissociates 15 times faster compared to BlocBuilder MA, which essentially mimics the effect of adding more free nitroxide at the onset of the polymerization, which should help to control the polymerization better [28]. We then tried to attach a thermoresponsive segment by chain extension with diethyl acrylamide (DEAAm). Poly (DEAAm) (PDEAAm) exhibits a lower critical solution temperature ~33°C in aqueous media and was shown recently to be controllable by BlocBuilder initiators [28]. After showing that potentially UV-active, thermoresponsive block copolymers can be made, testing of the solution behavior of the block copolymers in aqueous media was performed. This study will then serve as the starting point for further studies to manipulate the solubility of the copolymer, specifically the PPA block, by employing UV irradiation to incur the photo-Fries rearrangement.

2. Experimental

2.1. Materials

Phenyl acrylate (PA, ≥98%) and diethyl acrylamide (DEAAm, 99%) were purchased from Polysciences Inc, US. while tetrahydrofuran (THF, ≥99%), lithium bromide (LiBr, ≥99%) and 1,4-dioxane (≥99.0%) were obtained from Fisher Scientific, Canada. Diethyl ether (≥99%), HPLC grade N,N-dimethylformamide (DMF, ≥99.8%), and toluene (99.0%) were obtained from Sigma Aldrich, Canada. The monomers (PA, DEAAm) were purified by passage through a column containing a mixture of basic alumina and calcium hydride (40:1 weight ratio) and stored in a freezer under a head of nitrogen until required. NHS-BlocBuilder was synthesized according to the literature [29] from the commercially available unimolecular initiator 2-[*N*-*tert*-butyl-2,2-(dimethylpropyl)-aminooxy]propionic acid, which was kindly supplied from Arkema (known as Bloc-

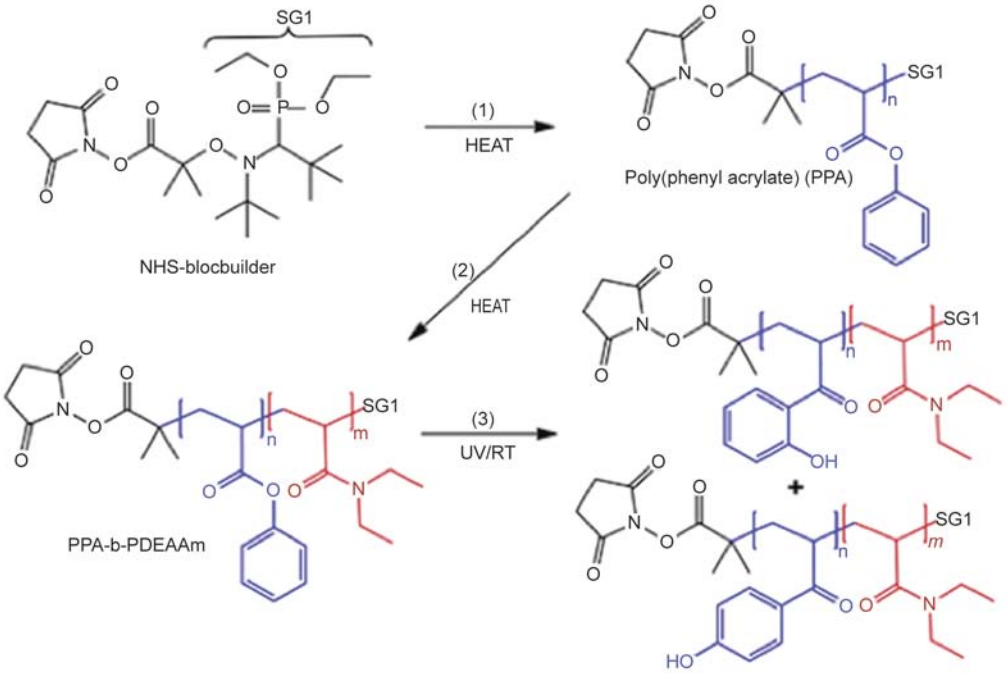

Figure 1. Synthetic route for UV-alterable/thermo-responsive block copolymers by NMP, where (1) is the homopolymerization of phenyl acrylate (PA) using NHS-BlocBuilder, followed by (2) the chain extension of the PPA homopolymers with diethyl acrylamide (DEAAm) and the potential molecular change resulting from (3) photo-Fries rearrangement of the phenyl acrylate units due to UV exposure

Builder MA) [29]. The additional [tert-butyl[1-(diethoxyphosphoryl)-2,2-dimethylpropyl]amino]oxidanyl (SG1, >85%) was graciously donated by Noah Macy of Arkema and used as received.

2.2. Phenyl acrylate (PA) homopolymerization

The PA homopolymerizations were done in a 10 mL three-neck round bottom flask with a magnetic teflon stir bar connected to a condenser that was chilled with cooling water (5°C). A thermocouple, inserted into a thermo-well joined to the reactor, was connected to a temperature controller that used a heating mantle to heat the reactor. As an example, the synthesis of PPA-3 is shown (see Table 1). First, PA (1.56 g, 10.50 mmol), NHS-BlocBuilder (0.051 g, 0.11 mmol), SG1 free nitroxide (0.0048 g, 0.016 mmol) and 1,4-dioxane (1.65 g) were added to the reactor prior to being sealed with a rubber septum. Nitrogen was then used to bubble the mixture for 25 minutes, removing any dissolved oxygen in the reactor. Once sufficiently bubbled, the nitrogen flow was reduced while the needle was raised above the liquid level to allow the system to be purged throughout the reaction. The temperature controller was set to 90°C and heating at a rate of 10°C·min^{-1} was commenced. After reaching the set temperature, samples were taken periodically and added to excess methanol to precipitate the polymer. After 625 min, the polymerization was stopped and the reactor contents were precipitated in methanol and dried in a vacuum oven at 60°C to evaporate any unreacted monomer or solvent that was still present. The final polymer was characterized by gel permeation chromatography (GPC) and ^{1}H NMR spectroscopy (yield = 0.50 g, final conversion = 0.31, number average molecular weight $\bar{M}_n$ = 3.8 kg·mol^{-1}, and dispersity $\bar{M}_w/\bar{M}_n$ = 1.17, relative to poly(styrene) standards in THF at 40°C). The kinetic plots and the evolution of the molecular weight distribution during the polymerization are shown in Figure 2. The summary of the molecular characteristics for the PPA homopolymers is shown in Table 1 below.

^{1}H NMR for PPA ($CDCl_3$, 25°C) (δ, ppm): 1.5–2.5 (backbone, –CH_2–CH–); 7.0–7.4 (aromatic, –COO–$C_6\underline{H}_5$).

^{13}C NMR for PPA ($CDCl_3$, 25°C) (δ, ppm): 36 (–CH_2–$\underline{C}$H–); 42 (–$\underline{C}H_2$–CH–); 120, 123, 128, 140 (aromatic –C_6H_5–); 173 (–COO–).

2.3. Chain extension with poly(phenyl pcrylate) (PPA) as macroinitiator

The chain extension of the PPA macroinitiator was performed with the same experimental set-up as the PA homopolymerizations. PPA-5 ($\bar{M}_n$ = 10.1 kg·mol^{-1}, $\bar{M}_w/\bar{M}_n$ = 1.55, 0.56 g, 3.15 mmol), DEAAm (2.04 g, 16.1 mmol) and toluene (2.60 g, 28.2 mmol) were added to the reactor, which was then sealed and bubbled with nitrogen for 25 minutes. The temperature controller was then set to 110°C and the nitrogen flow rate reduced. The reaction was allowed to continue for 11.5 h and then the mixture was cooled, precipitated in diethyl ether and dried in a vacuum oven at 60°C overnight. The final recovered yield for the copolymer was 1.2 g ($\bar{M}_n$ = 22.6 kg·mol^{-1}, $\bar{M}_w/\bar{M}_n$ = 1.91 relative to PMMA standards in DMF with 1 g·L^{-1} LiBr at 50°C; F_{PA} = 0.21 by ^{1}H NMR).

^{1}H NMR for PPA-*b*-PDEAAm ($CDCl_3$, 25°C) (δ, ppm): 1.0 (–CON–CH_2–$C\underline{H}_3$–); (1.5–2.0 (back-bone, –CH_2–CH–); 2.8–3.8 (–CON–$C\underline{H}_2$–CH_3–); 7.0–7.4 (aromatic, –COO–$C_6\underline{H}_5$).

^{13}C NMR for PPA-*b*-PDEAAm ($CDCl_3$, 25°C) (δ, ppm): 13–15 (–N–CH_2–$\underline{C}H_3$–); 35–37 (–CH_2–$\underline{C}$H–); 35–37 (–$\underline{C}H_2$–CH–); 40 (–N$\underline{C}$–H_2–CH_3–); 120, 123, 128, 140 (aromatic –C_6H_5–); 173 (–COO– overlapping from both monomers).

2.4. Characterization

Molecular weight characterization of the PPA homopolymers was determined using gel permeation chromatography (GPC) performed on a Water Breeze GPC. HPLC grade THF (>99.9%) was used as the eluent with a flow rate of 0.3 mL·min^{-1}, heated to 40°C while passing through three Waters Styragel® HR columns connected in series (HR1 with molecular weight measurement range of 10^2–$5\cdot10^3$ g·mol^{-1}, HR2 with molecular weight measurement range of $5\cdot10^2$–$2\cdot10^4$ g·mol^{-1}, and HR4 with molecular weight measurement range $5\cdot10^3$–$6\cdot10^5$ g·mol^{-1}). A guard column was also used. The GPC was equipped with ultraviolet (UV 2487) and differential refractive index (RI 2410) detectors and was calibrated using linear, nearly monodisperse poly(styrene) standards with THF as eluent at 40°C. The molecular weight characterization of the PPA-*b*-P(DEAAm) block copolymers was also determined using the same GPC but was equipped with 2 ResiPore (3 μm, MULTI pore type, 250×4.6 mm) columns with a ResiPore guard column (3 μm,

50×4.6 mm) (Polymer Laboratories) using HPLC grade DMF with 1 g·L^{-1} LiBr as the eluent and poly(methyl methacrylate) as standards. A mobile phase flow rate of 0.3 mL·min^{-1} was applied while the columns were heated to 50°C during the analysis. The molar composition of the final samples was determined using ^{1}H NMR spectroscopy, which was per-formed with a 400 MHz Varian Mercury instrument. For the conversion of phenyl acrylate (X), the disappearance of the vinyl peaks at 6.0–6.4 ppm relative to the aromatic peaks at 7.0–7.3 ppm, which appear in both unreacted monomer and resulting polymer, were used to determine X by ^{1}H NMR as shown in Equation (1):

$$X = 1 - \frac{A_{6.0}}{\frac{A_{7.0-7.3}}{5}} \tag{1}$$

where $A_{6.0}$ is the integrated area of the peak corresponding to one of the vinylic protons and $A_{7.0–7.3}$ is the integrated area of the peak corresponding to the 5 aromatic protons in the monomer and polymer.

For the copolymer, characteristic peaks for each monomer unit in the copolymer were identified: phenyl acrylate (5H, C_6H_5, 7.05–7.30 ppm); DEAAm (4H, –N–CH_2–, 2.85–3.8 ppm and 6H, –CH_3, 0.60–2.80 ppm). To determine the molar composition of the block copolymer with respect to PA, F_{PA}, the area of the peak corresponding to the protons from the aromatic group of the PA units were compared to the area of the peaks corresponding to the methylene protons attached to the nitrogen of the DEAAm units using the formula shown in Equation (2):

$$F_{PA} = \frac{\frac{A_{7.0-7.3}}{5}}{\frac{A_{7.0-7.3}}{5} + \frac{A_{1.0}}{6}} \tag{2}$$

where $A_{7.0–7.3}$ is the integrated area of the peak corresponding to the 5 protons in each of the PA units and $A_{1.0}$ is the integrated area of the peak corresponding to the 6 protons from the –CH_3 groups in each of the DEAAm units. The ^{13}C NMR was also done, confirming the structure of the homopolymer and the block copolymer.

For the aqueous solution properties, the block copolymer was dissolved in de-ionized water at 0.5 wt% concentration. Light transmittance of the solution at various temperatures was measured using a Cary 5000 UV-Vis-NIR Spectrophotometer at 600 nm. The solution was equilibrated for 30 min with stirring at 5°C and then heated at a rate of 0.5°C·min^{-1}. The transmittance was re-corded in increments at every 0.5°C. DLS (dynamic light scattering) measurements were per-formed with a Malvern Zetasizer (Nano-ZS). The instrument was equipped with a He-Ne laser operating at 633 nm and an avalanche photodiode detector. The samples were heated in 1°C increments, allowed to equilibrate for 1 min followed by 3 measurements, which were then averaged together to give one value at the temperature of interest.

3. Results and discussion

3.1. Synthesis of PPA homopolymers

In this study, we first demonstrate the homopolymerization of PA using a succinimidyl functional unimolecular alkoxyamine initiator (NHS-BlocBuilder [30, 31], Figure 1) followed by the synthesis of a PPA-*b*-P(DEAAm) block copolymer and the characterization of its thermo-responsive behavior. A series of PPA homopolymers were synthesized at either 90 or 110°C, using NHS-BlocBuilder with 0 or 15 mol% additional SG1 relative to NHS-BlocBuilder. In Figure 2a, for the polymerizations done at 90°C, the apparent rate constant (the slope of the semi-logarithmic plot of $\ln[(1–X)^{-1}]$ versus polymerization time t indicated that the effect of additional SG1 slowed the polymerization as expected. This is due to the added SG1 pushing the equilibrium between dormant and active chains towards the dormant chains, resulting in slower polymerizations [32, 33]. A similar effect of additional free SG1 nitroxide was observed for the polymerizations done at 110°C. Note that the polymerizations done at the higher temperature of 110°C were 2–3 times faster compared to the polymerizations done at 90°C, under otherwise identical conditions. The PPA homopolymerizations performed using NHS-BlocBuilder with no additional SG1 (experiments PPA-1 and PPA-2) exhibited a linear increase in number average molecular weight $\bar{M}_n$ versus conversion X (X<0.30) and relatively narrow molecular weight distributions ($\bar{M}_w/\bar{M}_n \approx 1.5$, Table 1). The PPA homopolymerizations synthesized using 15 mol% additional [tert-butyl[1-(diethoxyphosphoryl)-2,2-dimethylpropyl]amino]oxidanyl (SG1) relative to NHS-BlocBuilder (experiments PPA-3 and PPA-4) had similar increases in $\bar{M}_n$ versus X to that of PPA-1 and PPA-2 but the corresponding

molecular weight distribution was narrower ($\bar{M}_w/\bar{M}_n < 1.20$, Table 1). Similar reductions in $\bar{M}_w/\bar{M}_n$ have been observed when homopolymerizing other acrylates with additional SG1 [32, 34–37]. The

Table 1. Summary of phenyl acrylate (PA) homopolymerizations in dioxane solution using NHS-BlocBuilder (NHS-BB) as initiator

Sample ID	$[NHS\text{-}BB]_0$ [M]	$[PA]_0$ [M]	[dioxane] [M]	$T_{polym.}$ [°C]	r^a	$\bar{M}_n{}^b$ [kg·mol^{-1}]	$\bar{M}_w/\bar{M}_n$	$\bar{M}_{n,theoretical}{}^b$ [kg·mol^{-1}]	X^c
PPA-1	0.034	3.6	5.8	90	0	4.0	1.52	15.5	0.36
PPA-2	0.036	3.5	5.9	110	0	7.5	1.53	14.5	0.41
PPA-3	0.034	3.4	6.0	90	0.15	3.8	1.17	14.8	0.31
PPA-4	0.036	3.5	5.8	110	0.16	11.5	1.18	14.6	0.49
PPA-5	0.033	3.5	5.9	110	0	10.1	1.55	15.8	0.50

a: r = molar ratio of free SG1 nitroxide initially added relative to NHS-BlocBuilder unimolecular initiator.

b: $\bar{M}_n$ is the number average molecular weight and $\bar{M}_w/\bar{M}_n$ is the dispersity as measured by gel permeation chromatography (GPC) relative to linear poly(styrene) standards in tetrahydrofuran (PPA-1 to 4) at 40°C or poly(methyl methacrylate) standards in DMF with 1 g·L^{-1} LiBr (PPA-5) at 50°C. $\bar{M}_{n,\,theoretical}$ is the theoretical molecular weight at full conversion (mass of monomer added initially relative to moles of BlocBuilder-MA initiator added initially).

c: X is the final conversion of PPA monomer.

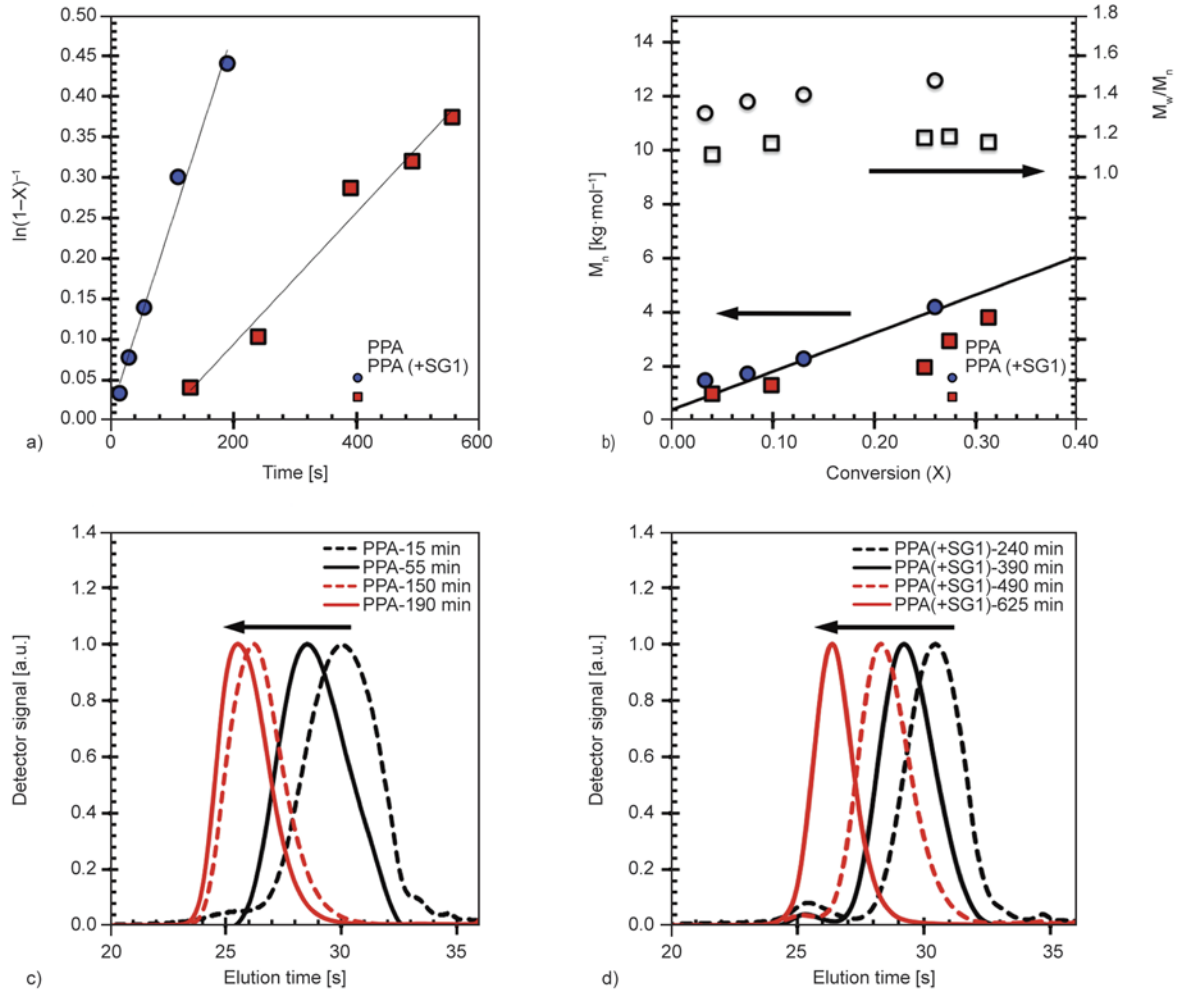

Figure 2. Homopolymerization of phenyl acrylate (PA) at 90°C using NHS-BlocBuilder with and without additional SG1 (15 mol% relative to NHS-BlocBuilder) where a) is the scaled conversion ($\ln[(1–X)^{-1}$ where X = conversion) versus polymerization time, b) is the number average molecular weight (M_n, filled symbols, circles = sample PPA-1, polymerization at 90°C, squares = sample PPA-3, polymerization at 90°C) and dispersity (M_w/M_n, empty symbols) versus X. The GPC chromatograms and the GPC chromatograms of samples taken during the PA homopolymerization at 110°C using c) no free SG1 added (sample PPA-2) and d) 15 mol% SG1 relative to NHS-BlocBuilder (sample PPA-4).

monomodal gel permeation chromatograms (GPC) confirmed this narrowing of the molecular weight distribution with the addition of SG1 (Figure 2c–2d). While the homopolymerization of PA by NMP has not been previously documented, the results are similar to those obtained for the homopolymerization of other acrylates by NMP [35]. Note that *X* of the PPA homopolymers was intentionally kept low to maximize the homopolymer's ability to cleanly re-initiate the second batch of monomer for the thermoresponsive block.

3.2. Chain extension of poly(PA) with DEAAm

A characteristic PPA homopolymer (PPA-5, $\bar{M}_n$ = 10.1 kg·mol^{-1}, $\bar{M}_w/\bar{M}_n$ = 1.55) was used as a macroini-

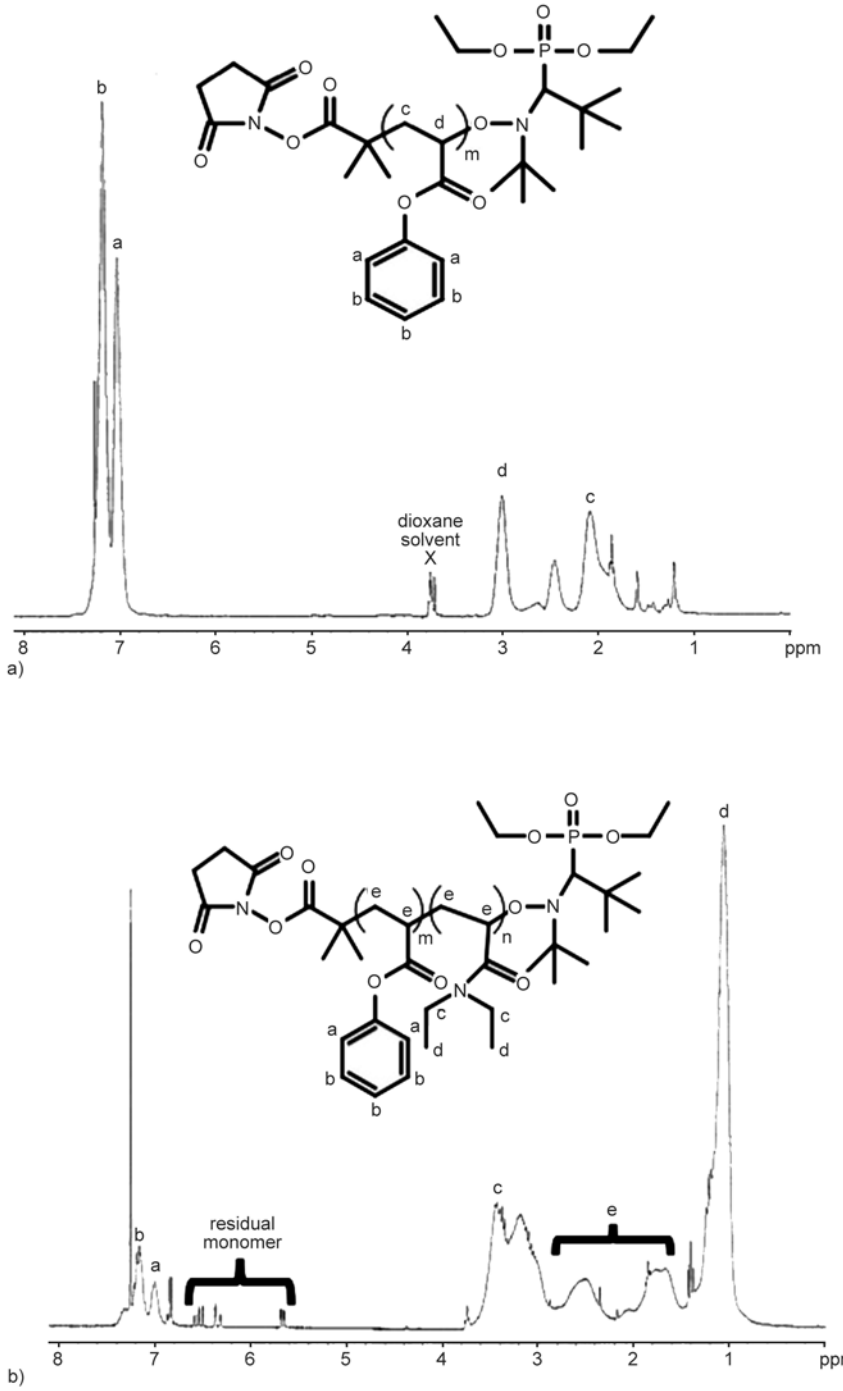

Figure 3. ^{1}H NMR ($CDCl_3$) of a) poly(phenyl acrylate) homopolymer (PPA-5) and b) poly(phenyl acrylate)-block-poly(diethyl acrylamide) (PPA-*b*-PDEAAm)

Table 2. Molecular characterizations for poly(PA) macroinitiator and chain extended PPA-*b*-PDEAAm

Sample ID	PPA macroinitiator		Chain-extended polymer		
	$\bar{M}_n$ [kg·mol^{-1}]	$\bar{M}_w/\bar{M}_n$	$\bar{M}_n$ [kg·mol^{-1}]	$\bar{M}_w/\bar{M}_n$	F_{PA}[a]
PPA-*b*-PDEAAm	10.1	1.55	22.6	1.91	0.21

a: F_{PA} is the molar fraction of PA in the final block copolymer PPA-*b*-PDEAAm and was determined by ^{1}H NMR. The PPA macroinitiator was PPA-5 (see Table 1) and its molecular weight was measured against poly(styrene) standards in THF at 40°C. The PPA-*b*-PDEAAm molecular weight was measured relative to poly(methyl methacrylate) standards in DMF with 1 g·L^{-1} LiBr at 50°C

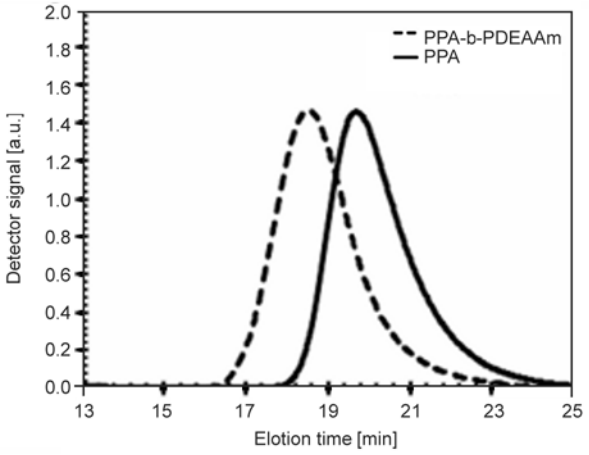

Figure 4. GPC chromatograms of the PPA macroinitiator (PPA-5, solid line) and the chain extended species (PPA-b-PDEAAm, dotted line) in the chain extension experiments

tiator for the polymerization of DEAAm. We chose to test a PPA homopolymer with a broader molecular weight distribution initially to see if it was still capable of reinitiating cleanly a second batch monomer despite its relatively high dispersity. The chain extension of the PPA macroinitiator was monitored by GPC and the composition was estimated from ^{1}H NMR (Figure 3a shows the ^{1}H NMR spectrum of the PPA macroinitiator and Figure 3b is the spectrum for the PPA-*b*-PDEAAm block copolymer). The final block copolymer had a broader molecular weight distribution compared to the macroinitiator ($\bar{M}_n$ = 22.6 kg·mol^{-1}, $\bar{M}_w/\bar{M}_n$ =1.91, relative to poly(methyl methacrylate) standards in DMF with 1 g·L^{-1} LiBr as eluent) but still retained a monomodal molecular weight distribution (see Figure 4). It should be noted that the molar composition of the final block copolymer measured by ^{1}H NMR does not match well based on the molecular weights estimated for the macroinitiator and the block copolymer by GPC. This is likely not surprising based on using poly(methyl methacrylate) standards in DMF for the GPC analysis as the PDEAAm segment is quite chemically different compared to that of the standards.

3.3. Thermo-responsive behavior illustrated by UV-visible spectrometry and dynamic light scattering

The thermo-responsive behavior of a 0.5 wt% solution of PPA-*b*-PDEAAm block copolymer ($\bar{M}_n$ = 22.6 kg·mol^{-1}, $\bar{M}_w/\bar{M}_n$ =1.91) in water was examined by UV-vis spectroscopy (Figure 5a) and dynamic light scattering (DLS) (Figure 5b). Due to the relatively hydrophobic PPA segment (F_{PA} = 0.21), the block copolymers were not completely soluble in pure H_2O and the solution was slightly opaque at room temperature. This was reduced upon slight heating below the cloud point temperature. The light transmittance profile showed typical behavior of LCST-type phase separation, where the solution was nearly 100% transparent at low temperature and became cloudy (~10% transmittance) quickly above the critical solution temperature, reflecting the sudden solubility decrease of polymer in water. The cloud point temperature T_{cp} determined here is below the 33°C reported by Idziak *et al*. [37] for the homopolymer PDEAAm. This can be ascribed to the presence of the hydrophobic PPA segment, which tends to suppress the LCST of the copolymer [38–40]. Also, the block copolymer exhibited a slight hysteresis in cloud point temperature between the heating and the cooling cycles (T_{cp} = 30°C for heating and T_{cp} = 26°C for cooling), which has also been observed for thermo-responsive polymers bearing tertiary amines [40–42]. It is generally attributed to the inter-polymer hydrogen bonding of the tertiary amine groups [42, 43]. In DLS measurements, the hydrodynamic diameter D_h was below 100 nm at low temperature for all cases and sharply increased to above 130 nm when the critical temperature was reached, illustrating the transformation from small micelles to large aggregated particles upon heating. The critical transition temperature observed in DLS corresponds well to that observed by UV-Vis, being about 30°C. The relatively large particle sizes at low temperature (5–20°C) may be attributable to the rel-

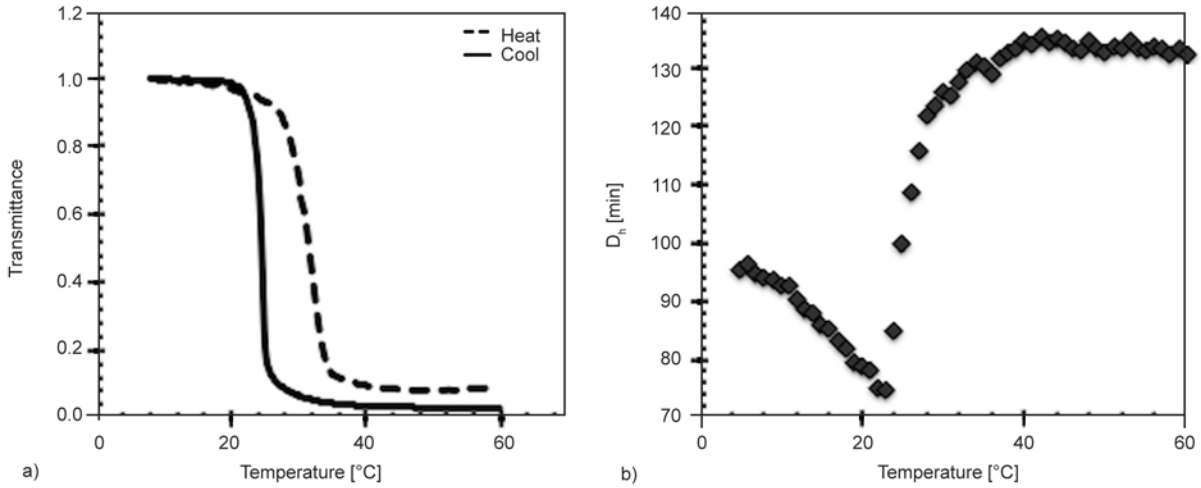

Figure 5. (a) Light transmittance as a function of temperature of PPA-*b*-PDEAAm block copolymer at 0.5 wt% in de-ionized water measured by UV-vis spectrometry; (b) hydrodynamic diameter of block copolymer (D_h) as a function of temperature for PPA-*b*-PDEAAm block copolymer in a 0.5 wt% solution in de-ionized water measured by dynamic light scattering

atively high molar fraction of the water insoluble PPA segment in the block copolymer but it was still dispersible in water. As the temperature however increased, the particle size slowly decreased to approximately 70 nm as the temperature increased from 5 to 20°C, as the PDEAAm corona was getting more insoluble and compressing, resulting in a smaller D_h. We observed similar behaviour in poly (oligo(ethylene glycol))-based block copolymers [39]. As the T_{CP} was approached, the particle size sharply increased, indicating aggregation to larger particles plateauing at about 140 nm. Larger particles may have precipitated out after T_{cp} was attained. The relatively low hysterisis shown in Figure 5 suggested the copolymer could re-dissolve rather easily upon cooling.

4. Conclusions

In summary, we showed that that the UV-active monomer PA could be easily homopolymerized by NMP in the temperature range between 90–110°C and the narrowest molecular weight distributions ($\bar{M}_w/\bar{M}_n$<1.20) were attained by adding a small fraction of additional free nitroxide (about 15 mol% relative to that of BlocBuilder MA). A PPA homopolymer was used as a macroinitiator for the incorporation of a thermoresponsive DEAAm block. The resulting PPA-*b*-PDEAAm block copolymer exhibited cloud points in the range 26–30°C, close to that of pure PDEAAm (cloud points of 33°C). The block copolymers will be examined next for irreversible changes in the PA solubility caused by the Photo-Fries rearangement of the PA segments, which would have a permanent effect on the thermoresponsive behavior of the block copolymers.

Acknowledgements

This work has been funded in part by the Canada Foundation for Innovation (CFI) New Opportunities Fund and the NSERC Discovery Grant. BL thanks the government of Canada for the Banting Postdoctoral Fellowship. We thank Scott Schmidt and Noah Macy of Arkema, Inc. for their help in obtaining the BlocBuilder™ and SG1 nitroxide mediators used in this work.

References

[1] Feng Z., Lin L., Yan Z., Yu Y.: Dual responsive block copolymer micelles functionalized by NIPAM and azobenzene. Macromolecular Rapid Communications, **31**, 640–644 (2010).
DOI: 10.1002/marc.200900777

[2] Roy D., Cambre J. N., Sumerlin B. S.: Future perspectives and recent advances in stimuli-responsive materials. Progress in Polymer Science, **35**, 278–301 (2010).
DOI: 10.1016/j.progpolymsci.2009.10.008

[3] Yu Y-Y., Tian F., Wei C., Wang C-C.: Facile synthesis of triple-stimuli (photo/pH/thermo) responsive copolymers of 2-diazo-1,2-naphthoquinone-mediated poly(*N*-isopropylacrylamide-*co*-*N*-hydroxymethylacrylamide). Journal of Polymer Science Part A: Polymer Chemistry, **47**, 2763–2773 (2009).
DOI: 10.1002/pola.23357

[4] Jiang J. Q., Tong X., Morris D., Zhao Y.: Toward photocontrolled release using light-dissociable block copolymer micelles. Macromolecules, **39**, 4633–4640 (2006).
DOI: 10.1021/ma060142z

[5] Lim S-J., Carling C-J., Warford C. C., Hsiao D., Gates B. D., Branda N. R.: Multifunctional photo- and thermo-responsive copolymer nanoparticles. Dyes and Pigments, **89**, 230–235 (2011).
DOI: 10.1016/j.dyepig.2010.03.013

[6] Kawatsuki N., Neko T., Kurita M., Nishiyama A., Kondo M.: Axis-selective photo-Fries rearrangement and photoinduced molecular reorientation in liquid crystalline polymer films. Macromolecules, **44**, 5736–5742 (2011).
DOI: 10.1021/ma200557k

[7] Griesser T., Adams J., Wappel J., Kern W., Leggett G. J., Trimmel G.: Micrometer and nanometer scale patterning using the photo-Fries rearrangement: Toward selective execution of molecular transformations with nanoscale spatial resolution. Langmuir, **24**, 12420–12425 (2008).
DOI: 10.1021/La802382p

[8] Kato J., Maekawa Y., Yoshida M.: Electron beam-induced Fries rearrangement of sulfonamide and sulfonate crystals. Chemistry Letters, **34**, 266–267 (2005).
DOI: 10.1246/cl.2005.266

[9] Li S-K. L., Guillet J. E.: Studies of the photo-Fries reaction in solid poly(phenyl acrylate). Macromolecules, **10**, 840–844 (1977).
DOI: 10.1021/ma60058a023

[10] Jenkins A. D., Jones R. G., Moad G.: Terminology for reversible-deactivation radical polymerization previously called 'controlled' radical or 'living' radical polymerization (IUPAC Recommendations 2010). Pure and Applied Chemistry, **82**, 483–491 (2010).
DOI: 10.1351/pac-rep-08-04-03

[11] Gueniffey H., Pinazzi C. P.: Polymerization of phenyl acrylate and para cresyl acrylate – Structures of polymers (in French). Makromolekulare Chemie, **148**, 93–105 (1971).
DOI: 10.1002/macp.1971.021480109

[12] Nicolas J., Guillaneuf Y., Lefay C., Bertin D., Gigmes D., Charleux B.: Nitroxide-mediated polymerization. Progress in Polymer Science, **38**, 63–235 (2013).
DOI: 10.1016/j.progpolymsci.2012.06.002

[13] Grubbs R. B.: Nitroxide-mediated radical polymerization: Limitations and versatility. Polymer Reviews, **51**, 104–137 (2011).
DOI: 10.1080/15583724.2011.566405

[14] Solomon D. H.: Genesis of the CSIRO polymer group and the discovery and significance of nitroxide-mediated living radical polymerization. Journal of Polymer Science Part A: Polymer Chemistry, **43**, 5748–5764 (2005).
DOI: 10.1002/pola.21067

[15] Hawker C. J., Bosman A. W., Harth E.: New polymer synthesis by nitroxide mediated living radical polymerizations. Chemical Reviews, **101**, 3661–3688 (2001).
DOI: 10.1021/cr990119u

[16] Georges M. K., Veregin R. P. N., Kazmaier P. M., Hamer G. K.: Narrow molecular weight resins by a free-radical polymerization process. Macromolecules, **26**, 2987–2988 (1993).
DOI: 10.1021/Ma00063a054

[17] Braunecker W. A., Matyjaszewski K.: Controlled/living radical polymerization: Features, developments, and perspectives. Progress in Polymer Science, **32**, 93–146 (2007).
DOI: 10.1016/j.progpolymsci.2006.11.002

[18] Kato M., Kamigaito M., Sawamoto M., Higashimura T.: Polymerization of methyl methacrylate with the carbon tetrachloride/dichlorotris-(triphenylphosphine) ruthenium(II)/methylaluminum bis(2,6-di-tert-butylphenoxide) initiating system: Possibility of living radical polymerization. Macromolecules, **28**, 1721–1723 (1995).
DOI: 10.1021/ma00109a056

[19] Wang J-S., Matyjaszewski K.: Controlled/'living' radical polymerization. Atom transfer radical polymerization in the presence of transition-metal complexes. Journal of the American Chemical Society, **117**, 5614–5615 (1995).
DOI: 10.1021/ja00125a035

[20] Moad G., Rizzardo E., Thang S. H.: Living radical polymerization by the RAFT process. Australian Journal of Chemistry, **58**, 379–410 (2005).
DOI: 10.1071/ch05072

[21] Chiefari J., Chong Y. K., Ercole F., Krstina J., Jeffery J., Le T. P. T., Mayadunne R. T. A., Meijs G. F., Moad C. L., Moad G., Rizzardo E., Thang S. H.: Living free-radical polymerization by reversible addition–fragmentation chain transfer: The RAFT process. Macromolecules, **31**, 5559–5562 (1998).
DOI: 10.1021/ma9804951

[22] Courbaron Gilbert A-C., Derail C., El Bounia N., Billon L.: Unexpected behaviour of multi-walled carbon nanotubes during '*in situ*' polymerization process: When carbon nanotubes act as initiators and control agents for radical polymerization. Polymer Chemistry, **3**, 415–420 (2012).
DOI: 10.1039/C1PY00357G

[23] El Bounia N. E., Courbaron Gilbert A-C., Billon L., Derail C.: Polymerization process in solution or in dispersed medium, of at least one monomer comprising at least one vinyl instauration, where the initiator and control agent of the polymerization are constituted of carbon nanotubes (in French). French Demande FR2962127 A1 20120106, France (2012).

[24] Glaser D. M., Coffey R., Jacobine A. F., Woods J. G.: Apparatus and methods for controlled radical polymerization. International Patent WO2009155303A2 (2009).

[25] Lecolley F., Tao L., Mantovani G., Durkin I., Lautru S., Haddleton D. M.: A new approach to bioconjugates for proteins and peptides ('pegylation') utilising living radical polymerisation. Chemical Communications, **2004**, 2026–2027 (2004).
DOI: 10.1039/B407712a

[26] Bathfield M., D'Agosto F., Spitz R., Charreyre M-T., Delair T.: Versatile precursors of functional RAFT agents. Application to the synthesis of bio-related end-functionalized polymers. Journal of the American Chemical Society, **128**, 2546–2547 (2006).
DOI: 10.1021/ja057481c

[27] Chenal M., Boursier C., Guillaneuf Y., Taverna M., Couvreur P., Nicolas J.: First peptide/protein PEGylation with functional polymers designed by nitroxide-mediated polymerization. Polymer Chemistry, **2**, 1523–1530 (2011).
DOI: 10.1039/C1py00028d

[28] Delaittre G., Rieger J., Charleux B.: Nitroxide-mediated living/controlled radical polymerization of *N,N*-diethylacrylamide. Macromolecules, **44**, 462–470 (2011).
DOI: 10.1021/ma102569e

[29] Vinas J., Chagneux N., Gigmes D., Trimaille T., Favier A., Bertin D.: SG1-based alkoxyamine bearing a *N*-succinimidyl ester: A versatile tool for advanced polymer synthesis. Polymer, **49**, 3639–3647 (2008).
DOI: 10.1016/j.polymer.2008.06.017

[30] Parvole J., Ahrens L., Blas H., Vinas J., Boissiere C., Sanchez C., Save M., Charleux B.: Grafting polymer chains bearing an *N*-succinimidyl activated ester end-group onto primary amine-coated silica particles and application of a simple, *one-step* approach via nitroxide-mediated controlled/living free-radical polymerization. Journal of Polymer Science Part A: Polymer Chemistry, **48**, 173–185 (2010).
DOI: 10.1002/Pola.23775

[31] Moayeri A., Lessard B., Maric M.: Nitroxide mediated controlled synthesis of glycidyl methacrylate-rich copolymers enabled by SG1-based alkoxyamines bearing succinimidyl ester groups. Polymer Chemistry, **2**, 2084–2092 (2011).
DOI: 10.1039/C1py00190f

[32] Bian K., Cunningham M. F.: Nitroxide-mediated living radical polymerization of 2-hydroxyethyl acrylate and the synthesis of amphiphilic block copolymers. Macromolecules, **38**, 695–701 (2005).
DOI: 10.1021/Ma0485383

[33] Nicolas J., Dire C., Mueller L., Belleney J., Charleux B., Marque S. R. A., Bertin D., Magnet S., Couvreur L.: Living character of polymer chains prepared via nitroxide-mediated controlled free-radical polymerization of methyl methacrylate in the presence of a small amount of styrene at low temperature. Macromolecules, **39**, 8274–8282 (2006).
DOI: 10.1021/ma061380x

[34] Hoogenboom R., Popescu D., Steinhauer W., Keul H., Möller M.: Nitroxide-mediated copolymerization of 2-hydroxyethyl acrylate and 2-hydroxypropyl acrylate: copolymerization kinetics and thermoresponsive properties. Macromolecular Rapid Communications, **30**, 2042–2048 (2009).
DOI: 10.1002/marc.200900507

[35] Lessard B., Tervo C., Marić M.: High-molecular-weight poly(*tert*-butyl acrylate) by nitroxide-mediated polymerization: Effect of chain transfer to solvent. Macromolecular Reaction Engineering, **3**, 245–256 (2009).
DOI: 10.1002/Mren.200900014

[36] Lessard B., Marić M.: Effect of acrylic acid neutralization on 'livingness' of poly[styrene-*ran*-(acrylic acid)] macro-initiators for nitroxide-mediated polymerization of styrene. Polymer International, **57**, 1141–1151 (2008).
DOI: 10.1002/Pi.2456

[37] Idziak I., Avoce D., Lessard D., Gravel D., Zhu X. X.: Thermosensitivity of aqueous solutions of poly(*N,N*-diethylacrylamide). Macromolecules, **32**, 1260–1263 (1999).
DOI: 10.1021/Ma981171f

[38] Lessard B. H., Savelyeva X., Marić M.: Smart morpholine-functional statistical copolymers synthesized by nitroxide mediated polymerization. Polymer, **53**, 5649–5656 (2012).
DOI: 10.1016/j.polymer.2012.10.020

[39] Lessard B. H., Ling E. J. Y., Marić M.: Fluorescent, thermoresponsive oligo(ethylene glycol) methacrylate/9-(4-vinylbenzyl)-9*H*-carbazole copolymers designed with multiple LCSTs via nitroxide mediated controlled radical polymerization. Macromolecules, **45**, 1879–1891 (2012).
DOI: 10.1021/ma202648k

[40] Lessard B., Marić M.: 'Smart' poly(2-(dimethylamino) ethyl methacrylate-*ran*-9-(4-vinylbenzyl)-9H-carbazole) copolymers synthesized by nitroxide mediated radical polymerization. Journal of Polymer Science Part A: Polymer Chemistry, **49**, 5270–5283 (2011).
DOI: 10.1002/pola.25004

[41] Becer C. R., Kokado K., Weber C., Can A., Chujo Y., Schubert U. S.: Metal-free synthesis of responsive polymers: Cloud point tuning by controlled 'click' reaction. Journal of Polymer Science Part A: Polymer Chemistry, **48**, 1278–1286 (2010).
DOI: 10.1002/pola.23872

[42] Yuk S. H., Cho S. H., Lee S. H.: pH/temperature-responsive polymer composed of poly((*N,N*-dimethylamino)ethyl methacrylate-*co*-ethylacrylamide). Macromolecules, **30**, 6856–6859 (1997).
DOI: 10.1021/ma970725w

[43] Wang X., Qiu X., Wu C.: Comparison of the coil-to-globule and the globule-to-coil transitions of a single poly(*N*-isopropylacrylamide) homopolymer chain in water. Macromolecules, **31**, 2972–2976 (1998).
DOI: 10.1021/ma971873p